

Aqueous synthesis and characterization of CdTe/CdS/ZnS quantum dots, their cytotoxicity, and cellular interactions

Von der Naturwissenschaftlichen Fakultät der
Gottfried Wilhelm Leibniz Universität Hannover

zur Erlangung des Grades
Doktorin der Naturwissenschaften (Dr. rer. nat.)

genehmigte Dissertation

von

Mehriban Ulusoy geb. Akin, M.Sc. (Türkei)

geboren am 19.07.1986 in Kardzhali, Bulgarien

2016

Referent: Prof. Dr. Thomas Scheper

Korreferent: Prof. Dr. Mark Green

Tag der Promotion: 29.01.2016

“Learn from yesterday, live for today, hope for tomorrow.

The important thing is not to stop questioning.”

Albert Einstein

Dedication

It is with my deepest gratitude and my warmest affection that I dedicate this dissertation to my lovely husband Mehmet, my parents Sabri and Neriman, my sisters Sabriye and Sibel, my nephew Mustafa, my grandmother Fatma, my best friends Emilia, Zeynep and Bin, and my life coach Hermann.

Your love, your support, as well as your trust have provided me a constant source of motivation and inspiration. My success wouldn't have been possible without you.

Mehriban Ulusoy

Hanover, 2016

Preface

This cumulative dissertation is submitted for the degree of Dr.rer.nat at the Gottfried Leibniz University of Hanover. The research described herein was conducted under the supervision of Prof. Dr. Thomas Scheper in the Institute of Technical Chemistry, between October 2012 and October 2015.

This work is to the best of my knowledge original, except where acknowledgements and references are made to the previous studies. The results of the work were published in peer-reviewed journals and presented in the international congresses. The structure of the thesis is adapted in the form of a ‘cumulative dissertation’ where experimental investigations, figure lists, as well as references were organized according to their appearance in their respective publications.

Mehriban Ulusoy

Hanover, 2016

Acknowledgements

My research life in the TCI has been nothing short of amazing. This thesis is the result of many experiences I have encountered at the TCI from dozens of remarkable individuals who I wish to acknowledge.

First and foremost, I would like to express my sincere gratitude to Prof. Dr. Thomas Scheper for giving me the opportunity to conduct my study in his group. Without his precious support it would not be possible to conduct this research.

Besides my advisor, my deepest thanks go to Dr. Frank Stahl for encouraging my research, helping me come up with the thesis topic and guiding me over almost three-years of development.

I also would like to express my special appreciation to Prof. Dr. Mark Green for his willingness to be co-supervisor of this work, for many insightful discussions and ideas during my research, as well as for his co-authorships in my publications.

Dr. Johanna Walter also deserves a special thank and appreciation for her continuous support and patience. Her accuracy and analytical thinking have thought me how to develop a keen eye for details. It was her critics that helped me to improve my scientific judgment skills. I also wish to thank Dr. Antonina Lavrentieva for her contributions and for providing me different aspects about my research. It was very enjoyable to work with her in the cell culture lab. Other deepest thanks go to Dr. Rebecca Jonczyk who thought me very valuable things since my master study. I feel lucky to be able to adapt her working discipline and multi-tasking ability.

I also would like acknowledge Imme Kretschmer, Lydia Sandiford, Alix Le Marois, Hamza Belhadj, Lutz Dreyer and Sergej Springer who contributed to my research to a great extent by conducting various experiments with quantum dots. I appreciate a lot their help and time. The same goes for Dr. Patrick Linder who gave me valuable suggestions and insights about statistical analysis for my data, Ivo Havlik and Michael Dors who provided me IT support, Martin Paehler and Martina Weiss who made everything easily accessible in the institute. I should also mention Ulrike Dreschel who was very kind to me when each time I brought her documents filled out with different surnames. I owe all of them a debt of gratitude.

I would like to extend my grateful thanks to the all members of the TCI. I spent such an amazing time at every activity with them. I got really lucky to be in this group. They

also have been a great help to foster my integration to German culture. I also thank Didem and Muharrem for the stimulating discussions as well as for fulfilling my longing for traditional Turkish food. I am also grateful to my office colleagues, Emi, Franzi, Martin and Michi. They gave me efficient critics in every aspects of my research and provided me a very productive atmosphere in the office.

I also would like to express my sincere appreciation to my life coach Hermann. His guidance helped me in all the time of research and taught me how to be critical and objective. He has played an integral role in my career, and has broadened my knowledge.

My hearty and deepest thanks go to Emi and Bin, my '*Yavrums*'. Their friendship has been the main source of my motivation and happiness throughout my research. What they have brought me in is priceless. They made me feel loved. Their impulsion for 'get up and go' saved me from the dreaded lab work.

Last but not the least, I would like to thank my husband and my family for their endless support throughout my life. In particular, I wish to thank my husband for attending my first oral talk at the congress and giving me the biggest motivation that anyone can give. Most importantly, he has always been very patience for enduring the long-distance relationship. It is their love and encouragements that always make me push my boundaries forward.

Thank you! Danke schön! Tesekkür ederim!

Abstract

Quantum dots (Qdots) are semiconductor nanocrystals with size-dependent optical properties that make them very attractive nanomaterials in biological studies. They have been widely utilized as fluorescent probes in targeted imaging, scaffolds in nano-sensors, and drug delivery vehicles. Since application of Qdots in biological contexts ultimately depends on their physicochemical and optical characteristics, to engineer Qdots with desired properties is one of the main topics in nanoparticle research.

The main objectives of this work are; (i) the aqueous synthesis and characterization of red-emitting Qdots, (ii) investigation of their *in vitro* cytotoxicity, (iii) development of their surface-related characteristics, and (iv) evaluation of their cellular interactions. Initially, an aqueous route to generate carboxyl-functionalized CdTe/CdS/ZnS Qdots with a core_(small)/shell_(thick)/shell_(thin) structure was developed. Synthesis of the outer ZnS shell around CdTe/CdS enhanced the quantum yield from 57% to 64%, increased photostability, and minimized toxicity. The applicability of Qdots as imaging agents was tested by coupling them with aptamers; as a result, the aptamer-Qdot conjugates were successfully internalized by the target cells. Later, toxic effects of Qdots were studied in detail by using three-dimensional (3D) spheroid cultures. 3D spheroids with *in vivo*-like structural morphology were found to be more resistant to Qdot toxicity than 2D cultures. Thereafter, an *in situ* approach for attachment of methoxy polyethylene glycol (mPEG) ligands to the surface of Qdot was developed to enhance surface-related characteristics. The effects of mPEG ligands on the growth of the ZnS shell, surface charge, colloidal stability, cytotoxicity, and non-specific cell binding were investigated. Overall, mPEG molecules improved colloidal stability to a great extent, diminished toxicity by 86%, and reduced non-specific binding. Confocal images also showed that Qdots penetrated into spheroids, and enabled their visualization.

In conclusion, the as-prepared Qdots presented an improvement over the previously reported Qdots in terms of enhanced fluorescence efficiency, increased stability, and reduced cytotoxicity. Their applicability in 3D spheroid imaging will promote their utilization in 3D imaging studies.

Keywords: *quantum dots, cytotoxicity, PEGylation, 3D spheroid culture, cell imaging*

Kurzfassung

Quantum Dots (Qdots) sind Halbleiter-Nanokristalle mit größenabhängigen optischen Eigenschaften, welche sie besonders attraktiv für biologische Anwendungen machen. Ihre Nutzung reicht dabei von bildgebenden Verfahren über die Sensorik bis zur gezielten Medikamentenfreisetzung. Diese biologischen Anwendungen beruhen auf den maßgeschneiderten physikochemischen und optischen Eigenschaften von Qdots, so dass die kontrollierte Herstellung und das Design von Qdots mit gewünschten Eigenschaften ein wichtiges Forschungsfeld im Bereich der Nanopartikel darstellt.

Die Ziele der vorliegenden Arbeit sind (i) die wässrige Synthese und die Charakterisierung von Qdots, die im Nahinfrarot emittieren, (ii) Untersuchungen zur Zytotoxizität dieser Qdots, (iii) die Generierung gewünschter Oberflächeneigenschaften, und (iv) die Evaluation ihrer zellulären Wechselwirkungen. Zunächst wurde die wässrige Synthese von Carboxyl-funktionalisierten Qdots anhand einer CdTe/CdS/ZnS core_(small)/shell_(thick)/shell_(thin) Struktur etabliert. Die Synthese einer äußeren ZnS Hülle um den CdTe/CdS Kern steigerte die Fluoreszenzausbeute von 57% auf 64%, erhöhte die Photostabilität und verringerte die Toxizität. Um die so synthetisierten Qdots in bildgebenden Verfahren einzusetzen, wurden Aptamere an ihre Oberfläche gekoppelt, die die spezifische Aufnahme in die Zelle über Oberflächenrezeptoren ermöglichen. Anschließend wurde die Toxizität in dreidimensionalen Spheroïdkulturen analysiert. Hier zeigte sich, dass dreidimensionale Spheroïdkulturen mit *in-vivo*-ähnlicher Morphologie widerstandsfähiger sind, als klassische zweidimensionale Zellkulturen. Anschließend wurden Methoxy-Polyethylenglykol Gruppen (mPEGs) an die Qdots gekoppelt. Für diese PEGylierten Qdots wurden die Oberflächenladung, die kolloidale Stabilität, die Zytotoxizität sowie die unspezifische Zellbindung analysiert. Die mPEG Gruppen erhöhen die kolloidale Stabilität bei gleichzeitiger Reduktion der Toxizität und unspezifischen Wechselwirkung mit Zellen. Mittels Konfokalmikroskopie konnte gezeigt werden, dass Qdots in dreidimensionale Zellstrukturen einwandern und so ihre Darstellung ermöglichen.

Die im Rahmen der vorliegenden Arbeit synthetisierten Qdots weisen im Vergleich zu den in der Literatur beschriebenen Qdots eine bessere Fluoreszenzausbeute, Stabilität und Toxizität auf. Insbesondere ihre Anwendbarkeit in der Visualisierung von Spheroïden wird ihre Nutzung in dreidimensionalen bildgebenden Verfahren fördern.

Stichwörter: *Quantum Dots, Zytotoxizität, PEGylierung, 3D Zellkultur, Visualisierung*

Table of Contents

1. Introduction	1
2. Aim and Scope	3
3. Theoretical Background	5
3.1. Introduction to quantum dots	5
3.2. Size-dependent photoluminescence properties of Qdots	7
3.3. Structural compositions of Qdots	9
3.3.1. Core/shell Qdot heterostructures	10
3.3.2. Core/shell/shell Qdot heterostructures	11
3.4. Synthesis of colloidal quantum dots	14
3.4.1. Organometallic synthesis of Qdots	15
3.4.2. Aqueous phase synthesis of Qdots	17
3.5. Cytotoxicity of Qdots	20
3.6. Features of Qdots as bio-imaging and therapeutic agents	24
3.7. Future aspects in Qdot development	29
4. Experimental Investigations	31
4.1. Aqueous synthesis of Qdots and their application in targeted imaging	32
4.1.1. Summary	32
4.1.2. Abstract	34
4.1.3. Introduction	35
4.1.4. Results and discussion	37
4.1.5. Experimental	47
4.1.6. Conclusions	52
4.1.7. Acknowledgements	52
4.1.8. Notes and references	52
4.1.9. Supplementary Information	54

4.2. Application of Qdots to 3D spheroid cultures	57
4.2.1. Summary	57
4.2.2. Abstract	59
4.2.3. Introduction	59
4.2.4. Experimental procedures.....	62
4.2.5. Results and discussion.....	66
4.2.6. Conclusions	75
4.2.7. Acknowledgements	76
4.2.8. References	76
4.2.9. Supplementary Information	78
4.3. Surface modification of Qdots with mPEG ligands	80
4.3.1. Summary	80
4.3.2. Abstract	82
4.3.3. Introduction	83
4.3.4. Results and Discussion.....	85
4.3.5. Conclusion.....	100
4.3.6. Materials and Method	100
4.3.7. Acknowledgements	105
4.3.8. References	105
4.3.9. Supplemantary Information	110
5. Conclusions and Outlook	111
List of Abbreviations	117
List of Figures	119
List of Tables	125
References	126
List of Publications	131
Curriculum Vitae	132

1. Introduction

Nanocrystals of semiconductors, so-called quantum dots (Qdots), represent one of the most diverse nanoparticle (NP) classes owing to a wide range of optical and structural properties. They exhibit various advantages due to their size-tunable optical features, narrow emission and broad absorption and excitation bands, and long fluorescence life times. These features allow Qdots to be utilized in numerous applications ranging from medicine to optoelectronic devices. Today's research has been focused on engineering such Qdot structural compositions with desired sizes and shapes, narrow size distributions, tailorable surface chemistries, and high optical yields. Synthesis of Qdots in aqueous solution facilitates water-solubilization of Qdots and increases their biocompatibility, as well as enables functionalization of their surfaces for biological studies. For that reason, aqueous synthesis routes to create bright and stable Qdots at mild temperatures with environmentally-friendly precursors have become preferred method over organic solvent-based organometallic synthesis approaches. The generation of near-infrared (NIR) emitting Qdots is of particular interest for biomedical applications, since they allow deep tissue imaging. They also have large surface areas that can interact with both diagnostic and therapeutic agents, resulting in multi-functional Qdots.

Qdots generally consist of an inorganic core and a shell of another inorganic material—forming core/shell systems. A $\text{core}_{(\text{small})}/\text{shell}_{(\text{thick})}$ system composed of a very small core (CdTe, CdSe) and a thick compressive shell (ZnS, ZnSe, CdS) having lattice strain-induced optical properties have emerged as a new class of Qdots. They exhibit greater photostability and giant spectral shifts in comparison to the traditional $\text{core}_{(\text{thick})}/\text{shell}_{(\text{thin})}$ Qdots. An external deposition of an inert shell material with a wide bandgap (e.g. ZnS) over the $\text{core}_{(\text{small})}/\text{shell}_{(\text{thick})}$ Qdot forming a $\text{core}_{(\text{small})}/\text{shell}_{(\text{thick})}/\text{shell}$ structure provides efficient passivation of the surface defect states, and enhances fluorescence efficiency. Moreover, the core/shell/shell Qdots exhibit a reduced toxicity due to their increased structural stability and minimized material decomposition to their environment. This effect is fundamental for the use of Qdots in biological labeling studies, which rely on their optical and structural properties.

Qdots with inherent size, shape, and surface chemistry can be readily internalized into cells. After the discovery of their cellular uptake capability, they have been immensely

used in targeted *in vitro* and *in vivo* fluorescence imaging studies. However, their application in uptake studies has raised some concerns. Their fate and possible toxicity in the organism comprise one of the major points of issue. Therefore, it is obligatory to investigate adverse effects of Qdots on cellular level prior to their bioapplication. The major factors that determine the interactions of Qdots with cells are their composition, size, shape, surface chemistry, and colloidal stability. Among them, surface ligands play a significant role since they direct interaction of Qdots with proteins, membranes and cells, and establish various nano-bio interfaces. Researchers, for that reason, spend a lot of effort to engineer Qdot surfaces with versatile ligands, e.g. peptides, oligonucleotides, polymers such as polyethylene glycol (PEG), to develop Qdots with desired surface functionalities.

To study nanoparticle and drug interactions as well as their side effects, three-dimensional (3D) cell cultures has become recently an important research area. 3D cell culture models resemble closely *in vivo* tissue micro-environment in terms of cellular communication, extracellular matrix development, and diffusion/transport mechanisms. They provide more accurate *in vitro* model in comparison to traditional monolayer cell cultures. Therefore, utilization of 3D cultures to explore Qdots toxicity holds great potential to produce physiologically relevant data, and provides the first essential step to give a detailed insight into interactions of Qdot with cells.

2. Aim and Scope

The objectives of this study are divided into three parts. In the first part, aqueous synthesis of CdTe/CdS/ZnS quantum dots (Qdots) emitting in the near-infrared (NIR) region will be studied. Fabrication of Qdots directly in aqueous media facilitates water dispersion of Qdots, and involves utilization of environmentally-friendly precursors for the nanocrystal growth. Moreover, it eliminates post-synthesis surface modification processes to render Qdots water soluble. Therefore, an aqueous approach will be developed to synthesis first CdTe/CdS Qdots having a very small CdTe core and a thick CdS shell structure. 3-mercaptopropionic acid (MPA) molecules will be utilized as surface coordinating ligand, since carboxyl groups that originate from MPA ligands are expected to provide colloidal stability of Qdots through electrostatic interactions, and enable further surface modification. Further, epitaxial growth of a ZnS shell will be achieved in order to improve the fluorescence yield and photostability of Qdots. ZnS has been mostly used as the material of choice due to its inert nature and wide-band gap energy. It passivates surface defects efficiently, and ensures confinement of electron-hole pair in the core/shell region. Moreover, the capability of the ZnS shell to mitigate Qdot-induced toxicity should be tested by applying appropriate *in vitro* cell viability assays. Later, targeted labelling efficiency of Qdots should be studied by coupling Qdots with DNA aptamers. DNA aptamers with a specific binding affinity to the target cells is expected to promote cellular internalization of Qdots.

In the second part, adverse effects of Qdots will be investigated by using three-dimensional (3D) spheroid cultures. Spheroid cultures have been introduced as a simple 3D model for high-throughput cell-based screening assays. Through utilization of 3D spheroids, more physiologically relevant data about Qdot-induced cellular toxicity is aimed to be obtained in order to understand Qdot interaction mechanisms with micro-sized tissue-like structures. Moreover, applicability of Qdots for labelling and monitoring spheroid structures should be investigated to give more insight into Qdot binding characteristics with 3D cellular systems.

In the third part, surface-related structural properties of Qdots will be improved by developing an *in situ* approach to modify Qdot surfaces with thiol-terminated methoxy polyethylene glycol (mPEG) molecules. PEG molecules are found to have meritorious effects on structural function of nanoparticles (NPs). For instance, they improve

structural stability, reduce cytotoxicity, diminish undesired NP–cell interactions, and prolong NP circulation time in the body. On this basis, influence of mPEG surface ligands to e.g. Qdot surface charge, colloidal stability, cellular toxicity, and non-specific cell binding should be investigated in detail. Effect of mPEG amount should also be studied in order to comprehend the relationship between the surface mPEG density and the mPEG functional properties.

In summary, this work aims to provide methods for the development and characterization, as well as biological application of Qdots with enhanced optical and structural properties.

3. Theoretical Background

Quantum dots (Qdots) are colloidal nanocrystals (NCs) that consist of ~1–10 nm diameter semiconductor materials. They carry organic capping ligands that coordinate to the surface atoms, enabling passivation of surface defects as well as solubilization of Qdots in various solvents. Qdots possess size-dependent optical and electronic properties that make them very attractive nanomaterials in fluorescence bio-imaging applications and in nanoscale electronic and optoelectronic devices. In this section, structural and functional properties of Qdots with regard to their synthesis and biological applications will be addressed.

3.1. Introduction to quantum dots

Nanoscale particles that exhibit quantum confinement effect are often referred to as ‘*quantum dots*’. A quantum dot (Qdot) is a semiconductor nanocrystal with a size on the nanometer length scale of which lie in the regime where quantum confinement effect arises [1]. Qdots often exhibit strong variations in their optical and electrical properties with size effects although they have the same interior bonding geometry as the corresponding bulk material. These changes arise through systematic transformations in the density of electronic energy levels as a function of the size of the interior, known as quantum size effects [2]. Semiconductor structures can be made with a wide variety of shapes according to the spatial confinement of excitons (electron–hole pairs) (**Fig. 1**). Bulk crystals having three dimensions above 100 nm are classified as three-dimensional (3D) semiconductors as their excitons are not confined to the nanoscale in any dimension. For two-dimensional (2D) nanostructures, two dimensions are not confined to the nanoscale, thus they have only one dimension under 100 nm. 2D nanocrystals can exhibit plate-like shapes, such as nanofilms, nanolayers, and nanocoatings. One-dimensional (1D) nanostructures have only one dimension out of nanoscale range; thereby they exhibit needle-like shaped nanomaterials, e.g. nanotubes, nanorods, nanowires. In zero-dimensional (0D) nanostructures, exciton confinement occurs in all three spatial dimensions. Thus, all three dimensions are in nanoscale length. The most common representation of 0D nanostructures is Qdot (**Fig. 1**).

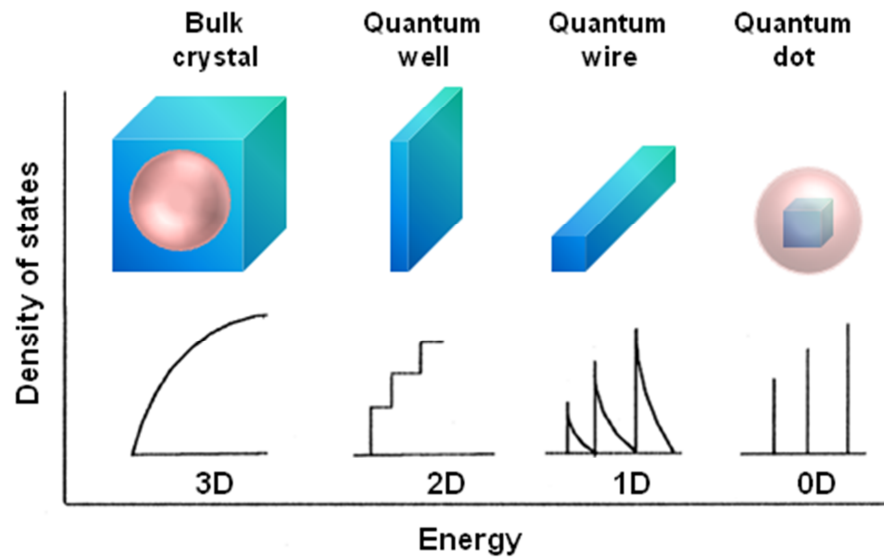


Fig. 1 Schematic illustration of the energy levels of a semiconductor crystal structure as a function of dimension. 3D, 2D, 1D and 0D indicate three, two, one, and zero-dimension, respectively. The energy levels of the bulk semiconductor in 3D are continuous, while in the case of 0D energy levels are discrete [2]. The exciton-Bohr diameter is represented by the sphere. Modified from reference [3].

The width of the energy gap that separates the conduction from the valence energy band is an important parameter for a semiconductor material. In bulk semiconductor crystals of macroscopic sizes, the width of this band is determined by the material identity; therefore it is a fixed parameter. However, in the case of semiconductor nanocrystals with sizes less than 10 nm, bandgap energies change with respect to their sizes since 1–10 nm size range corresponds to the regime of quantum confinement. Exciton-Bohr radius describes the spatial extension of excitons (electron–hole pairs) in solids, which ranges from 2 to 50 nm depending on the material. As the size of a Qdot approaches the exciton-Bohr radius, confinement begins to affect the exciton wave function and induces changes in the density of electronic states and in the energy level separation [4]. As a result, the bandgap energy increases with a decrease in the Qdot size, and continuous energy bands of the bulk material split into discrete atomic energy levels due to the quantum confinement. These well-separated energy states can be labelled using atomic-like notations (1S, 1P, 1D) as illustrated in **Fig. 2** [5]. As the size of the Qdot becomes smaller, the separation between the energy levels becomes wider, leading to a spectrum of discrete energies. As a result, Qdots respond to changes in the particle size by adjusting their energy spectra, leading to quantum size effect. When the Qdot size is small enough (< 10 nm) to allow quantum confinement effect to be in the strong regime, electronic and optical properties of the Qdots become highly tunable.

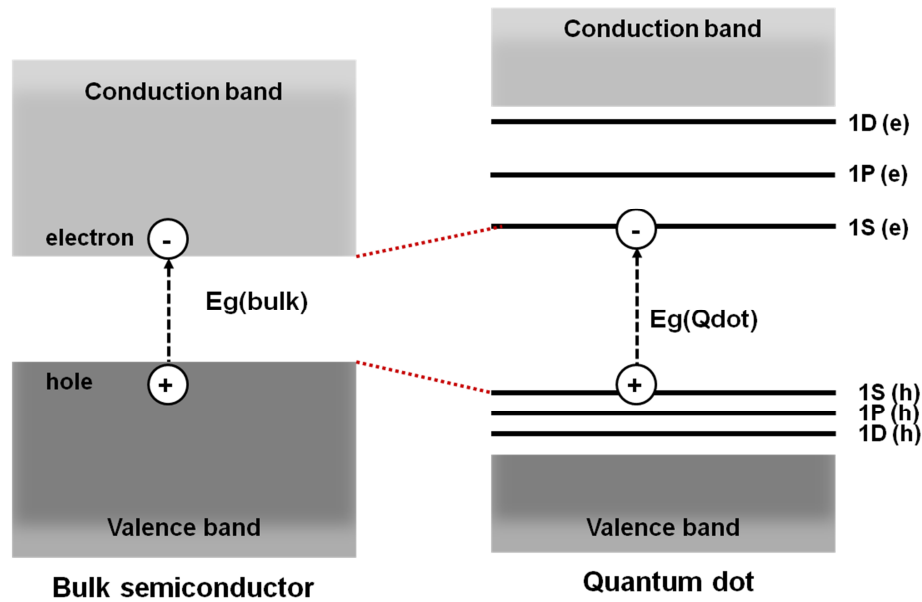


Fig. 2 Schematization of the electronic band structure of a bulk semiconductor (left) and the quantum confinement effect on a quantum dot (right). E_g indicates the bandgap energy between the highest occupied molecular orbital and the lowest unoccupied molecular orbital for the bulk and the Qdot. Charge carriers are demonstrated with (+) and (-) signs, indicating hole and electron, respectively. Modified from reference [6].

3.2. Size-dependent photoluminescence properties of Qdots

Material composition of a Qdot determines the electronic band structure which in turn defines the photoluminescence characteristics of the Qdot. When a photon is absorbed, an electron gains energy and transit from valence band to an unoccupied orbital in conduction band. In the meantime, the excited electron leaves behind an electron hole in the valence band. After a finite duration, conduction band electron loses its energy and re-occupies the energy state of the electron hole in the valence band. This process is called ‘radiative recombination of charge carriers (electrons and holes). Equivalent to this process, photons are emitted at a wavelength corresponding to the bandgap energy of the Qdot. The photoluminescence properties of Qdots that are derived from the exciton recombination events are strongly related to the Qdot sizes. For a spherical Qdot with a radius R , the bandgap energy is inversely proportional to R^2 . Therefore, an increase in the size of the Qdot corresponds to a decrease in its energy gap (**Fig. 3a**). Larger Qdots having more closely-located energy levels absorb photons at low energies. This leads to a red shift in the emission spectrum as the Qdot size increases. On the contrary, a decrease in the Qdot size in turn increases the bandgap energy, and

results in a blue shift of the emission (**Fig. 3b**). As a result, the optoelectronic properties of Qdots become strongly size-dependent, making it possible to tune the photoluminescence properties of Qdots through a wide spectral window by arranging the composition and size of the Qdots [4].

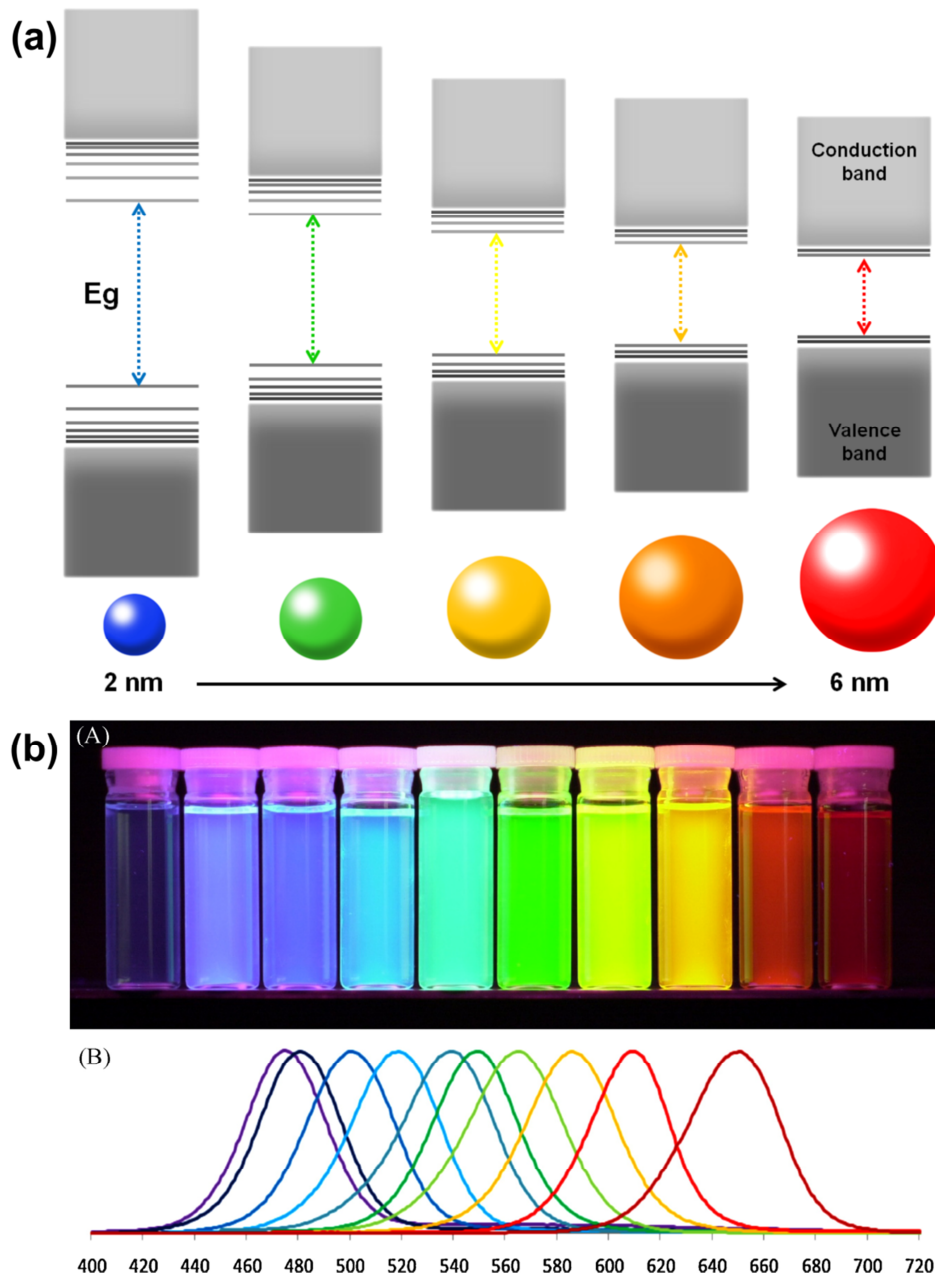


Fig. 3 (a) Schematic representation of the quantum confinement effects: the bandgap of the Qdot increases with a decrease in its size, and discrete energy levels arise at the band-edges. Also, the energy difference between the band-edge levels increases with a decrease in size. Modified from reference [4]; (b) upper image shows the emission colours of Qdots from left-to right with increasing nanoparticle sizes, and the lower image shows their corresponding emission spectra covering a wide spectrum. Reprinted from reference [7].

3.3. Structural compositions of Qdots

Qdots are hybrid nanomaterials that consist of an inorganic semiconductor nanocrystal and a surface coating layer. The inorganic component can be composed of atoms from various groups in the periodic table, such as II–VI (CdTe, ZnS, CdSe, CdS, ZnTe, or HgTe), III–V (InP, InAs, or GaP), I–VI (Ag_2S , Ag_2Se , and Ag_2Te), IV–VI (PbS, PbSe and PbTe), or I–III–VI (CuInS_2 , CuInSe_2 , AgInSe_2) and in many different alloyed compositions (e.g. CdSeTe, CdZnS, CdInS) [8]. The inorganic component can be composed of either a single core (e.g. CdTe, ZnSe) or a core/shell (e.g. CdTe/CdS, $\text{Cu}_2\text{S}/\text{ZnS}$) or a core/multi-shell (CdTe/CdSe/ZnS) heterostructure. The surface coating layer consist of organic ligand molecules that facilitate passivation of surface defect sites at the inorganic/organic interface, and solubilization or/and functionalization of Qdots for further applications. The schematic illustration of structural compositions of Qdots is shown in **Fig. 4 (i–iii)**.

The structure of the organic ligand can be either hydrophilic or hydrophobic depending on the reaction solution in which Qdots are grown. The hybrid nature of the Qdots gives them remarkable and unique properties that can be controlled by adjusting the composition, size and shape of each component in the Qdot structure [10–12].

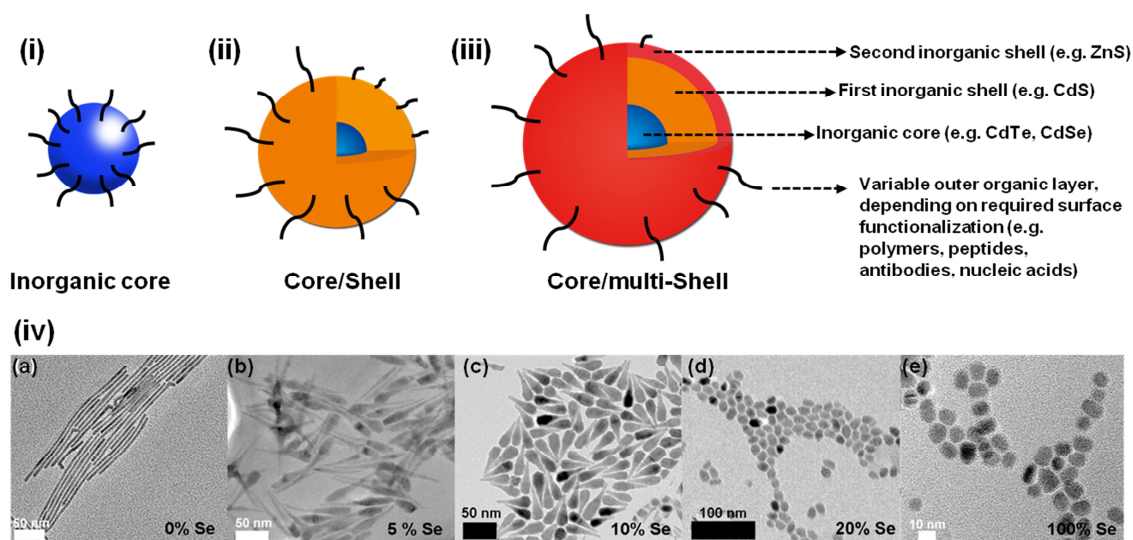


Fig. 4 Heterostructures of Qdots: (i) inorganic core passivated with organic surface ligands; (ii) inorganic core/shell heterostructure passivated with organic surface ligands; (iii) inorganic core/shell/shell heterostructure coated with organic surface ligands; (iv) TEM images of $\text{CdS}_{1-x}\text{Se}_x$ Qdots showing their morphology as a function of Se loading: (a) 0% Se loading (CdS), (b) 5% Se loading ($\text{CdS}_{0.68}\text{Se}_{0.32}$), (c) 10% Se loading ($\text{CdS}_{0.42}\text{Se}_{0.58}$), (d) 20% Se loading ($\text{CdS}_{0.33}\text{Se}_{0.67}$), (e) 100% Se loading (CdSe). Scale bars: 50 nm (a, b, c), 100 nm (d), and 10 nm (e). Reprinted from reference [9].

For instance, Ruberu *et al.* reported adjustable morphology changes in $\text{CdS}_{1-x}\text{Se}_x$ Qdots with relative sulfur and selenium loading [9] (**Fig. 4iv**). The interaction between the inorganic nanocrystal and the surface ligand molecules gives rise to size- and shape-dependent optical properties that can be controlled during the synthesis of Qdots [11, 13, 14]. As an example, Bao *et al.* obtained a series of aqueous cysteine-capped CdTe Qdots with interesting 1D nanowires and 3D hexagonal structures by manipulating the local amount of surface coordinating ligand [15]. Moreover, the organic ligand layer can be easily manipulated with various surface chemistry approaches, making it possible to render Qdots a number of surface properties (hydrophilicity, charge density, colloidal stability, flexibility to conjugation) for biological applications [16].

3.3.1. Core/shell Qdot heterostructures

Qdots with a single inorganic core structure that are passivated with organic ligands, as shown **Fig. 4i**, generally have low fluorescence quantum yields due to the surface related defect sites. Surface defects increase the probability of nonradiative recombination of excitons; therefore reduce the fluorescence yields (**Fig. 5**). Surface organic ligands that are coordinated with surface atoms are insufficient to passivate cationic and anionic surface traps simultaneously. Thus, they lead to formation of an incomplete surface coverage, making nanocrystals susceptible against environmental changes. Synthesis of a shell of a distinct semiconductor material around core, namely formation of a ‘core/shell’ structure (**Fig. 4ii**), can address this problem by providing a sufficient passivation of surface trap states.

The outer shell can enable passivation of both cationic and anionic surface traps, and give rise to enhanced fluorescence quantum yields [8, 17]. As a result, it provides a physical barrier between the optically active core and the surrounding medium, thus making the Qdots less sensitive to environmental changes, reduce photo-oxidative degradation, and increase chemical stability. Moreover, by controlling the composition and the thickness of the shell, its size and shape, tunability of fluorescence emission wavelengths can be achieved over a wide range of spectrum from visible to far-infrared region [19].

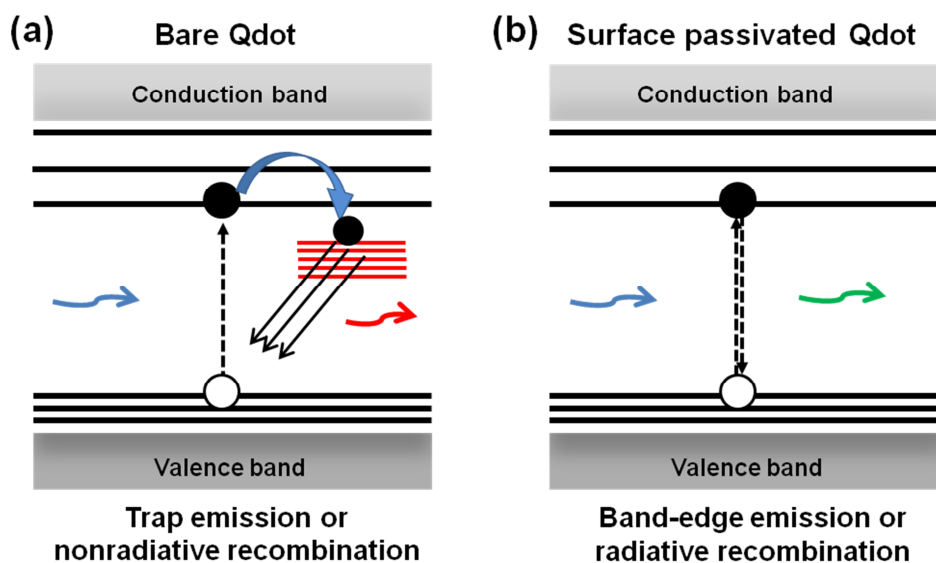


Fig. 5 Effect of surface states on the recombination process: (a) when the surface states are not passivated, the electrons at the conduction band can be trapped at the surface defect states, resulting in a weak surface state emission; (b) when the surface states are passivated well by inorganic shell layers, trap emission is eliminated and band-edge emission occurs. Adapted from reference [18].

3.3.2. Core/shell/shell Qdot heterostructures

Binary core/shell systems might not respond simultaneously to the requirements for appropriate electronic and structural properties. Particularly, if there is a significant lattice mismatch between the core and the shell material, overgrowth of the shell can cause significant deteriorations in the crystal structure. An example showing the lattice mismatches between the bulk materials is shown in **Fig. 6**. The mismatched lattice parameter not only prevents epitaxial growth of a thick shell, but also causes formation of nanocrystal defects, thus reduce the photoluminescence properties. In this case, deposition of an intermediate shell of a distinct semiconductor material between the core and the outer shell, forming a ‘core/shell/shell’ structure (**Fig. 4iii**), can reduce the strain between the core and the outer shell. This core/shell/shell heterostructure has been first proposed by Reiss *et al.* where they synthesized CdSe/ZnSe/ZnS Qdots [20]. The intermediate shell layer serves as a lattice adapter between the lattice-mismatched core and the outer shell, whereas the outer shell ensures efficient passivation of surface traps and confinement of charge carriers inside the core/shell structure. Consequently, the core/shell/shell system offers higher photo-chemical stability and higher fluorescence quantum yields than the core/shell system [22].

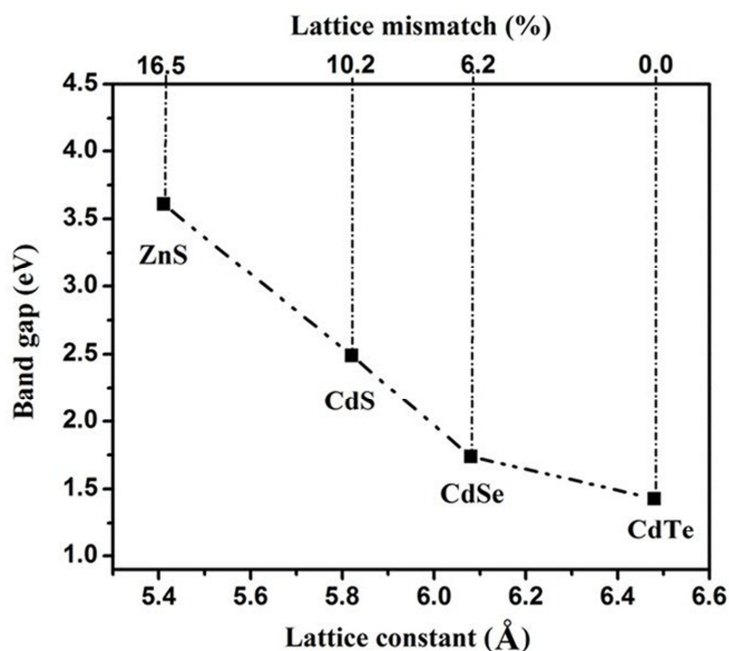


Fig. 6 The interrelationship between the bandgap energies, lattice constants, and lattice mismatches of CdTe, CdSe, CdS, and ZnS bulk semiconductors. The lattice parameters of bulk CdTe was utilized as a reference to calculate mismatch values. Reprinted from reference [21].

ZnS is the common material of choice as the outer shell. Its wide bandgap energy (3.8 eV for the bulk material) provides a sufficient confinement of electron and holes inside the nanocrystal structure. Moreover, it is nontoxic and chemically stable. For that reason, it has been extensively employed as the outer shell material to passivate inorganic cores [23-26]. However, the large mismatched lattice parameters between CdSe (ca. 10.3%), and CdTe (ca. 16.5%) cores and the ZnS shell induce a strain at the core/shell interface [27, 28]. This interfacial strain leads to formation of dislocations in the nanocrystal structure. Therefore, the defects in the ZnS shell negatively affect both the photoluminescence efficiency and the stability of Qdots, particularly at large ZnS shell thicknesses [8, 29]. It is worth mentioning that upon growing the ZnS shell, nanoparticle size distribution broadens substantially, indicating that Qdots lose their monodispersity. For that reason, the formation of an intermediate shell material, e.g. CdS, CdSe, CdZnS, can be a solution to generate Qdots with effective optical features [21, 30-32].

Another approach to generate a core/shell/shell system is to synthesize an outer shell layer consisting of a large bandgap semiconductor material around core/shell structure. This strategy is mostly applied to Qdots that have type-II electronic band structure. In a type-II band alignment, electron and holes are partially or completely confined in the

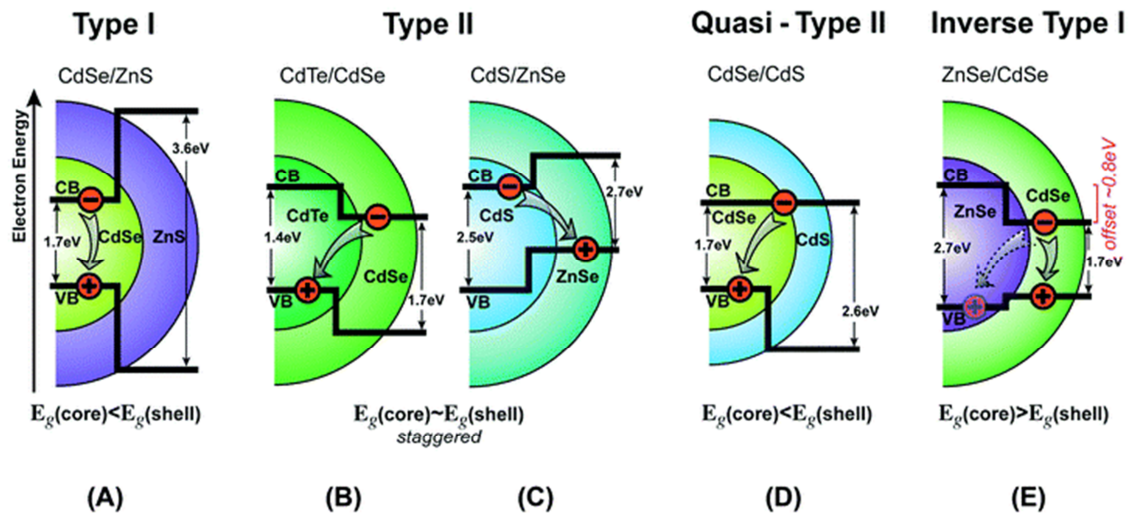


Fig. 7 Types of electronic band structures in Qdots that can be engineered by the selection of core and shell material: (a) Type-I band alignment– bandgap of the core is smaller than that of the shell, therefore electron and holes are confined in the core. A change in the shell thickness can induce slight red-shift in emission wavelengths. (b) type-II band alignment– valence and conduction band edges of the core are either lower or higher than those of the shell. Therefore, either electrons or holes are confined in the shell. An increase in the shell thickness can induce a great red-shift in emission wavelengths. (c) Inverse type-II band alignment, (d) quasi type-II band alignment– electrons are confined both in the core and shell, (e) inverse type-I alignment– both charge carriers are localized in the shell. Arrows show the lowest exciton energy separation between the occupied energy states at the core/shell interface (E_g) [18]. Reprinted from reference [33].

shell since bandgap of the shell material is smaller than that of the core. In contrast to that, in a type-I band alignment, the bandgap of the shell material is larger than that of the core, therefore both electrons and holes are confined in the core [19]. A schematic illustration that shows band alignments in type-I and II systems is given in **Fig. 7**. The advantages of type-II system over type-I are that they exhibit prolonged fluorescence lifetimes and a great tunability of emission wavelengths to the near-infrared region. However, extended fluorescence lifetimes can increase the probability of nonradiative recombination events; one of the separated charge carriers which are located in the shell can be trapped in the surface defect sites [34]. In the type-II system, surface passivation is achieved by organic surface ligands. Surface coordinating ligands can fail to provide a complete surface passivation which can further cause an inevitable decrease in fluorescence efficiency. Therefore, the addition of a large-bandgap outer shell layer, resulting in a core/shell/shell system can be a key factor to overcome those problems [35, 36].

3.4. Synthesis of colloidal quantum dots

A significant progress has been made in the synthesis of high-quality Qdots in the last decades. Organometallic route *via* which Qdots have been synthesized by thermal decomposition of organometallic precursors in a hot reaction medium, so-called hot injection method, has been applied widely by several groups in order to engineer Qdots with desired properties. Alternative to that, aqueous synthesis methods, i.e. conventional refluxing, hydrothermal, and microwave-assisted synthesis, have also been developed to generate water-soluble Qdots that are of great interest for biological studies. In common synthetic methods, anionic precursors are rapidly injected into solution containing cationic precursors at temperatures that are dependent on the boiling point of the reaction solution under required atmospheric conditions. In general, formation mechanism of Qdots can be divided to three stages: (i) pre-nucleation, (ii) nucleation, and (iii) growth. The schematic illustration of Qdot growth is depicted in **Fig. 8**. Accordingly, in the pre-nucleation stage, when the precursors are added, monomers are formed with a number of surface coordinating ligand. As the concentration of monomers increases, small and unstable clusters (i.e. subcritical nuclei, crystal nuclei or seeds) start to form [6]. Later on, at the nucleation stage, these clusters act as templates for crystal growth, and they reach a sufficient size to be capable of growing further rather than redissolving into monomers [37]. Formation of nuclei with a radius equal to or larger than the critical radius (i.e. the crystal nucleus radius at which the probabilities of growth and dissolution become equal) occurs either by the addition of monomer units to the largest possible subcritical nuclei, or by the coalescence of two or more smaller subcritical nuclei into a nucleus. At the growth stage, the growth of Qdots occurs *via* the diffusion of monomers to the crystal nuclei surfaces, which is followed by incorporation of monomers into the crystal nuclei [38]. The sequential addition of monomer units to the growing Qdots and/or coalescence of smaller Qdots proceed allowing the growth of the critical and supercritical crystal nuclei. The continuous consumption of monomers during the nucleation leads to a decrease in free monomer concentration below critical nucleation concentration, and nucleation discontinues. As monomers are depleted throughout the reaction, Ostwald ripening process takes place, a process whereby small particles dissolve in order to support the growth of larger particles [6, 39].

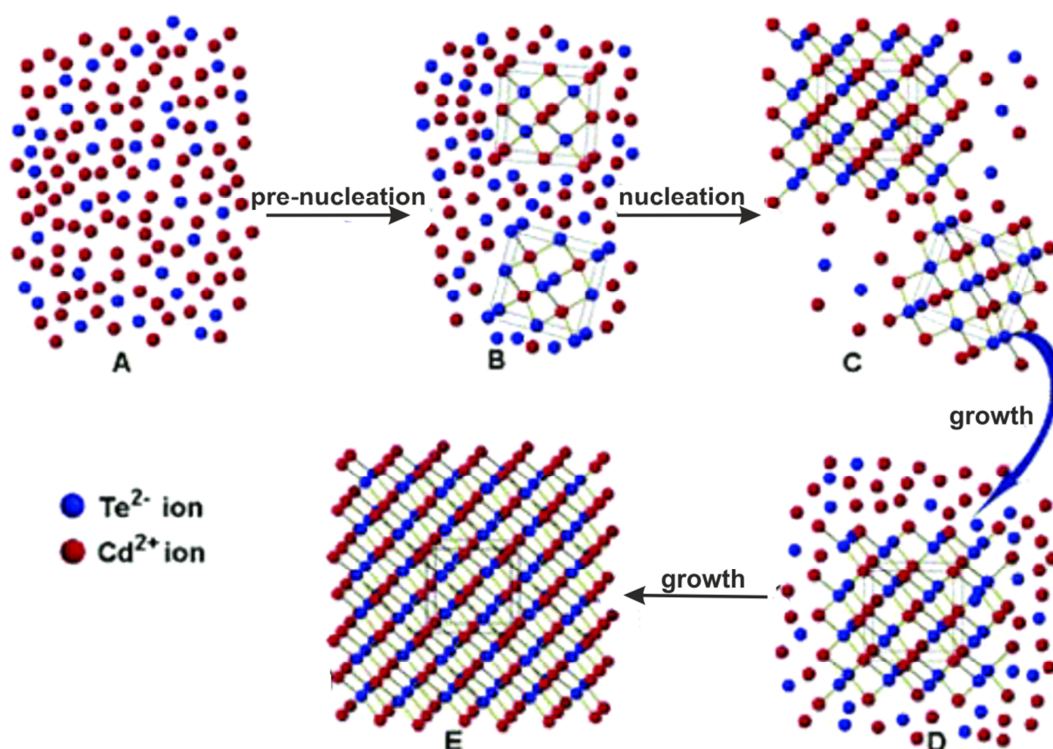


Fig. 8 Schematic presentation of the nanocrystal formation mechanism. Initially, precursors react to form monomers which later nucleate to form small nuclei (A-B). As the reaction temperature rises, small nuclei grow into stable nanocrystals (C-D-E). Modified from reference [40].

3.4.1. Organometallic synthesis of Qdots

In a typical organometallic approach, the metal precursor solution (for Cd, Zn, In etc.) is dissolved in apolar coordinating solvent with a high boiling point (e.g. tri-*n*-octylphosphine oxide (TOPO), hexadecylamine (HDA), oleic acid (OA), *n*-octadecylamine (ODA), *n*-octadecylphosphonic acid (ODPA), hexanethiol (HT), or stearic acid) under an inert atmosphere. After heating the reaction solution to ~ 230 - 280 °C, the chalcogen precursor (for Se, Te, S etc.) dissolved in another coordinating solvent, e.g. tri-*n*-octylphosphine (TOP), tributylphosphine (TBP), is swiftly injected into the flask under continuous stirring. This initiates rapid nucleation of seed colloidal NCs. To terminate the particle growth, the temperature of the reaction solution is cooled when the desired Qdot size is obtained. During the Qdot growth, surface ligands with amphiphilic characteristics coordinate with their polar head groups (S, N, O, P) to the metal ions on the Qdot surface. In the mean time, non-polar hydrocarbon tail groups determine the interactions of surface layer with the surrounding medium [4]. Following the synthesis of inorganic core, a passivating shell layer can be grown epitaxially by the injection of shell precursors, e.g. zinc and sulphur. Upon cooling the solution to room

temperature, core/shell Qdot heterostructures are obtained *via* precipitation [41]. A schematic illustration for the synthesis of Qdots is depicted in **Fig. 9**. The core/shell Qdots obtained from this organometallic procedure are highly fluorescent, stable against photo-oxidation, and monodisperse with narrow size-distributions. However, they are not soluble in aqueous solution, and they don't possess appropriate surface moieties for their conjugation to biomolecules. Therefore, they require post-synthesis surface modification processes to enable their application as fluorescence labels in biological studies. In order to make the Qdots water-soluble and biocompatible, the surface coordinating ligands (e.g. TOPO, ODA, or HDA) must be replaced or modified with other surface molecules which will allow Qdots to be dissolved in aqueous media and be linked to biomolecules. The utilization of Qdots grown by organometallic approach in biomedical applications has been achieved by several groups using various chemical surface modification approaches that can essentially be categorized in two main groups: (i) removal of the native capping ligands and replacing them with bifunctional hydrophilic ligands (ligand-exchange); and (ii) encapsulation of the native hydrophobic ligands with amphiphilic polymers or phospholipids, forming Qdots micelle structures [42]. For ligand-exchange reactions, single thiols such as mercaptoacetic acid (MAA), mercaptopropionic acid (MPA), mercaptoundecanoic acid (MUA), thiol- β -D-lactose, monothiol-PEG derivatives, cysteine, dendrons; or multiple thiols, amines and histidines, e.g. dihydrolipoic acid (DHLA) and its PEG, Tween, albumin and sulphobetaine derivatives, aminated polymers, cysteine-functionalized polyaspartic acid, bithiol-g-polyethylene glycol, multi-branched dendrimers, and peptides, have been utilized [24, 26, 42-46]. For the encapsulation processes, di- or triblock and random copolymers, phospholipids, β -cyclodextrine, silica, and polymer microspheres have been applied [42, 45, 47]. Additional detailed information about the conjugation strategies can be found in the review of Zhang *et al.* [48].

Surface modification reactions have been reported to cause dramatic loss of fluorescence [25, 44, 47, 49] and make Qdots prone to degradation due to the lack of original capping layer [43, 50], thus hindering imaging efficiency of Qdots to a great extent. Also, the current modification strategies still suffer from inefficiency, and strong dependence on the conditions and materials used. Hence, the colloidal stability of non-aqueous Qdots in aqueous buffers and in biological media needs to be improved by developing new surface coating strategies that will provide Qdots which are stable

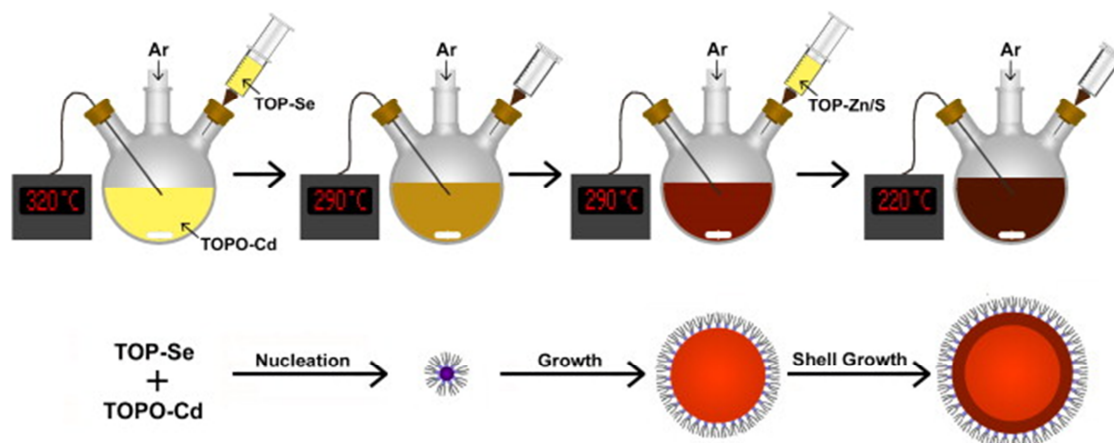


Fig. 9 Organometallic synthesis of colloidal CdSe core and CdSe/ZnS core/shell Qdots in high-temperature coordination solvent. In summary, anionic TOP-Se precursor are rapidly injected into solution containing the cationic TOPO-Cd precursor at elevated temperature under an inert atmosphere (nitrogen or argon). Reprinted from reference [41].

over a wide range of biologically-relevant conditions such as acidic and basic pHs and in the presence of excess counterions [45]. Moreover, the chemicals used in organic medium are very toxic, expensive, unstable in the air, and they require very harsh reaction conditions, e.g. very high temperature (>200 °C) and pressure, and an inert atmosphere. These issues, therefore, lead to the search for alternative synthesis routes.

3.4.2. Aqueous phase synthesis of Qdots

Synthesis of Qdots directly in aqueous solution is a facile method to obtain water-soluble and biocompatible Qdots for biological applications. For aqueous synthesis, atmospheric conditions and low reaction temperatures (<100 °C) are sufficient to obtain Qdots, making the process more environment-friendly, time and cost-effective, and feasible for industrial scale production. A typical synthesis involves the reaction of metal precursors (for Cd, Zn, Cu, In, and Pb etc.) with chalcogen precursors (for Te, Se, and S etc.). Metal precursors are acetates, nitrates or chlorides which are easily dissolved in water, whereas the chalcogen precursors can be either a commercial solid powder (e.g. Na_2TeO_3) [15] or freshly prepared before using in the reaction, e.g. H_2Te or NaHTe . H_2Te is prepared by adding sulphuric acid dropwise to the aluminium telluride (Al_2Te_3) [51], while NaHTe is prepared by the reaction of sodium borohydride (NaBH_4) with tellurium (Te) powder in the case of CdTe Qdots [14]. However, NaHTe and H_2Te are unstable compounds under ambient conditions; therefore, the synthesis of CdTe Qdots generally performed in an inert atmosphere. For that reason, air-stable

Na_2TeO_3 has been utilized as alternative to perform the synthesis in air, avoiding the need for an inert atmosphere. Thus, the synthetic procedure is free of complicated vacuum manipulations and more environment-friendly [39, 52].

Besides precursor solutions, surface coating ligands (also called as surfactants) play an important role for controlling the growth rate, size and shape of the Qdots. Several thiol molecules, including mercapto acids, mercapto alcohols, and mercapto amines, with a strong binding affinity to metal surfaces have been adapted as surface coordinating ligands in aqueous phase synthesis. The most commonly applied thiol ligands are thioglycolic acid (TGA) [53, 54], 3-mercaptopropionic acid (MPA) [55], mercaptosuccinic acid (MSA), glutathione (GSH) [56], L-cysteine (Cys) [57], mercaptoundecanoic acid (MUA) [32], dihydrolipoic acid (DHLA) [58], N-acetyl-L-cysteine (NAC) [59], and 2-mercaptoethylamine (MA) [60]. The sulfhydryl groups can coordinate to the Qdot surfaces, whereas the terminal functional groups, i.e. carboxyl, amine, and hydroxyl, can contribute to the electrostatic stabilization of the colloidal Qdots as well as to their surface modification for various applications. The molecular structure of some thiol ligands as well as exemplary surface structure of a thiol-stabilized CdTe Qdot is shown in **Fig. 10**.

Surface ligands play a key role for the growth of the Qdots. Metal precursors form micelle-like metal clusters in the presence of ligands in the reaction solution. These metal clusters serve as templates that limit the nucleation and the growth of the particles. Therefore, the binding strength of the ligand to the particle surface dominates the growth behaviour of the metal clusters. For instance, a stronger coordination between ligand and the metal surface will generally result in formation of smaller particles [62]. It is also well-established that concentration of the ligands as well as the temperature and pH of the reaction solution is responsible for the reactivity of metal precursors, as well as for tuning the size and the shape of the Qdots. They arrange the balance between the nucleation and the growth, and allow generation of high-quality Qdots [16]. The achievement of desired particle sizes with narrow size distribution, good crystallinity, high photostability, desired surface structure, and high quantum yields are the parameters that are considered to be characteristics of a “high-quality” of the chemically prepared Qdots [63]. 3-Mercaptopropionic acid (MPA) has been the most applied surface stabilizing ligand for the synthesis of Cd-based Qdots with improved optical properties [39]. When compared to other thiol-ligands, MPA enables tunability of fluorescence emissions to longer wavelengths up to 800 nm while

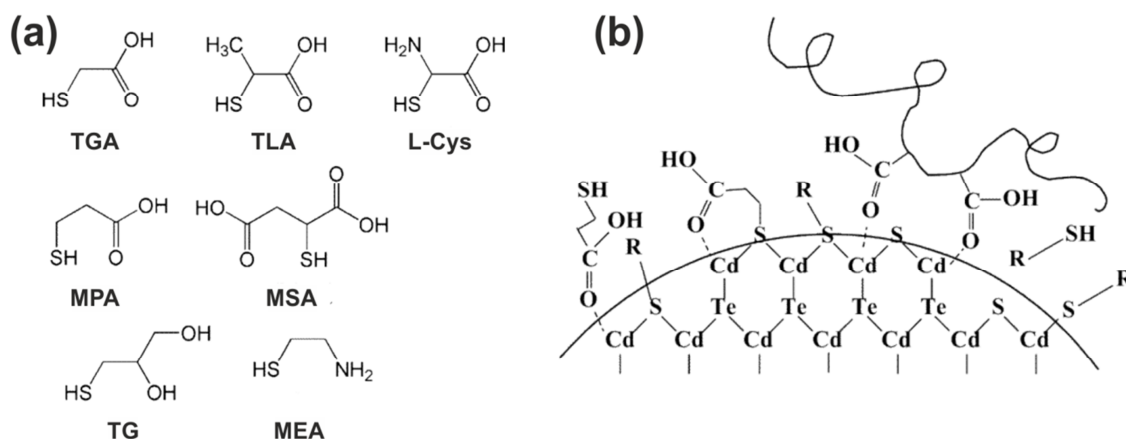


Fig. 10 (a) Molecular structures of some thiol-ligands (modified from reference [14]); (b) schematic illustration of the surface structure of the CdTe Qdots modified with MPA and poly(acrylic acid) (PAA). R represents carboxylic acid groups and the coil represents alkyl chain of PAA. Dotted lines show the coordination between carbonyl oxygen and cadmium on the Qdot surface. Unbounded sulphur atom on the surface indicates the decomposition of R group from the thiol-ligand. Reprinted from reference [61].

maintaining the particle monodispersity, and accelerating the growth rate of Qdots [64]. Moreover, Zhang and co-workers have demonstrated that carboxyl groups of MPA coordinating with cadmium ions effectively improved both fluorescence efficiency and the stability of the CdTe Qdots [61].

In the aqueous phase synthesis, growing Qdots at low temperatures (<100 °C) can cause high amount of surface defects. Surface defects may act as nonradiative recombination sites for electron-hole pairs, thereby reducing the fluorescence yield of the Qdots. Moreover, aqueous synthesis of Qdots can generate wide particle size distributions with wide emission peaks. These factors can compromise the optical and structural quality of Qdots and limit their potential applications. However, Qdot performances can be optimized by varying the synthesis parameters that affect reaction kinetics, such as precursor concentrations, molar composition of precursor solutions, pH, temperature, and structure and concentration of surface ligand molecules. After the establishment of the first aqueous synthesis of thiol-stabilized CdTe Qdots in 1996 by Rogach and co-workers [65], sufficient progress has been made in the aqueous preparation and the design, as well as in the characterization of Qdots which exhibit tunable emission wavelengths in the range of 400-1200 nm, enhanced fluorescence yields (40-84%), increased stability against degradation, and tailorable surface chemistries [21, 39, 66-69]. It should be also noted that the applications of semiconductor Qdots synthesized in water mostly relate to CdTe since this material has been best investigated. Nevertheless, the majority of the assembly and application

approaches developed for CdTe Qdots are also transferrable to other types of thiol-capped Qdots.

3.5. Cytotoxicity of Qdots

Understanding of nanoparticle (NP) interaction mechanisms with biological environments is pivotal for their safe translation from basic science to applied nanomedicine [70]. In the past decade, there has been a dramatic increase in the use of Qdots in biological research and in industrial production, which in turn has raised questions about the potential toxicity of such nanomaterials [71]. It is well known that Qdots can be internalized into the cells through various endocytic pathways, e.g. receptor-mediated endocytosis, clathrin/caveolae-mediated pinocytosis, macropinocytosis, and phagocytosis [72]. The internalization of Qdots has promoted their application for visualization of cells. However, their vast utilization has necessitated a profound research to investigate the interactions of Qdots with cells, and their effects on cellular processes. A huge body of work has been conducted with cultured cells in order to understand the underlying mechanisms for Qdot-induced cytotoxicity, and in turn to develop new routes to characterize and optimize their cellular interactions [70]. *In vitro* assessment of dose-dependent cytotoxicity of Qdots is widely accepted as proof-of-principle studies for the prediction of *in vivo* cytotoxicity [73, 74]. The assessment of Qdot cytotoxicity, however, has been complicated due to the great structural variety in the design of Qdots [75]. Internalization level of Qdots also alters in different neighbouring cells, due to variances in cell size, cell cycle phase and accumulation of Qdots to cell sites [70]. Physicochemical properties of Qdots (diameter, surface charge, and surface area), their surface coating, material composition, as well as applied Qdot concentrations, incubation conditions, type of cells and assay being used display synergetic effect for the inherent toxicity of Qdots [73, 76]. Physicochemical properties of Qdots that determine the inevitable fate of Qdots in biological systems are illustrated in **Fig. 11**. Furthermore, recent studies have demonstrated a close relationship between side effects of Qdots and their intracellular localization, degradation, and local concentration [77]. Nanoparticles (NPs) with sizes as small as natural proteins (2-10 nm) can reach cellular compartments, such as nucleus, where larger particles cannot reach. Furthermore, their

entrapment in endosomal vesicles after their uptake can increase their local concentration which cannot be achieved by free ions [77]. Due to their intrinsic small sizes (<10 nm), they have a high surface area to volume ratio, thus, a high reactive surface to interact with cellular components.

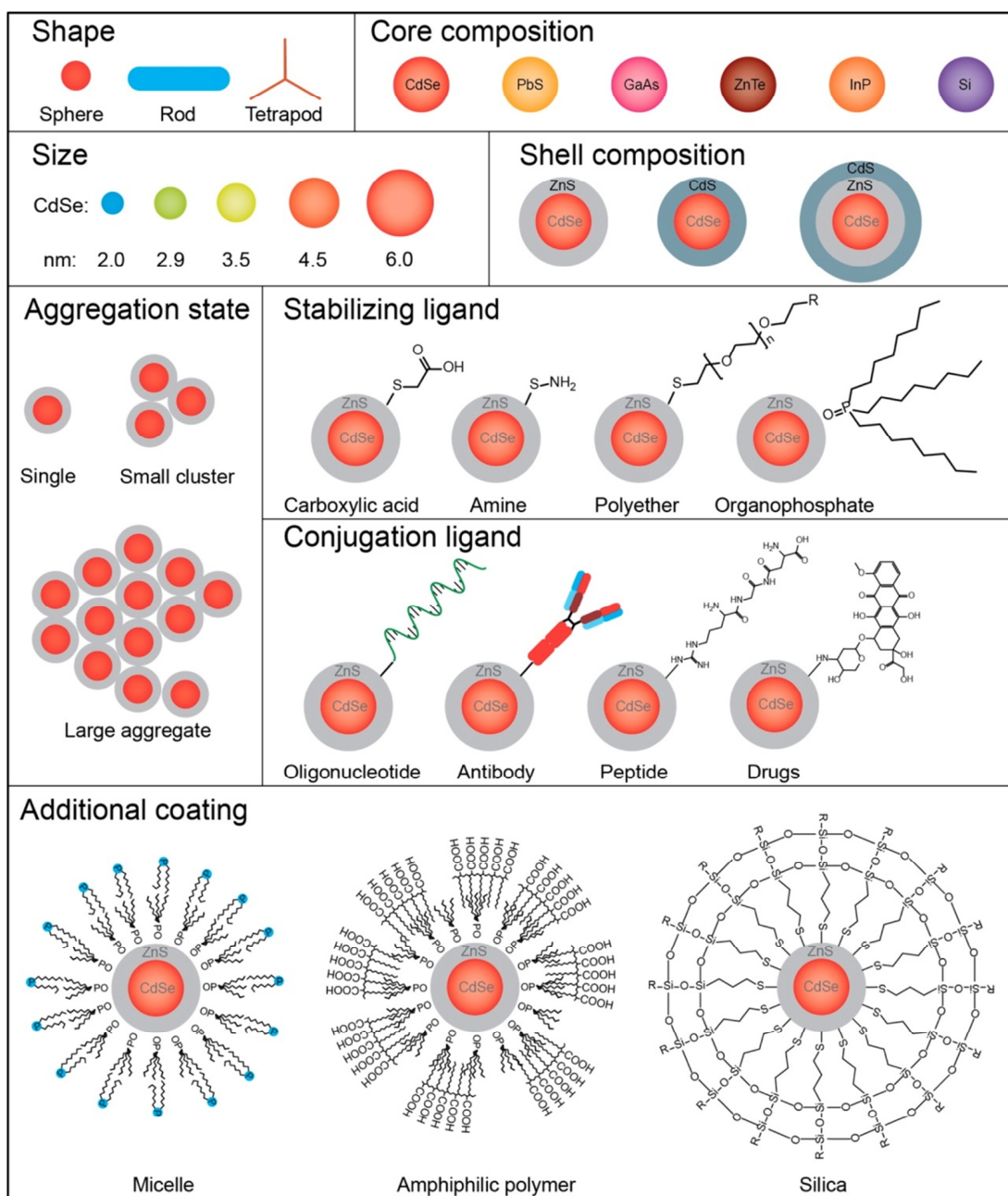


Fig. 11 Physicochemical properties of Qdots that determine their biological fate and inherent toxicity: shape, core and shell composition, size, and surface ligands can be manipulated during synthesis. Additional surface coating strategies, and surface modification steps with target-specific biomolecules can be assessed after their synthesis in order to increase the stability of Qdots against photo-oxidation and degradation to improve their biocompatibility, and manipulate their uptake efficiency. Reprinted from reference [74].

Surface structure of Qdots also dictates their cellular interactions, their uptake mechanism, as well as uptake efficiency [78]. Due to these common features of Qdots, several mechanisms have been predicted by which Qdots can induce adverse effect to the cells. A common phenomenon is generation of reactive oxygen species (ROS) by cells that are exposed to Qdots. The generated ROS can be either radical (nitric oxide or hydroxyl radicals) or non-radical (hydrogen peroxide). Levels of ROS that are higher than the cells can tolerate may result in cell damage by peroxidizing lipids and disrupting structural proteins, enzymes, and nucleic acids [79]. The possible mechanisms for NP-induced generation of ROS are illustrated in **Fig. 12**.

Release of heavy metal ions (Cd^{2+} , Pb^{2+} , In^{3+}) from Qdots is generally considered as the main cause of cytotoxicity [82]. Release of metal ions can be caused by the photo-oxidation of Qdot, therefore reduction of Cd and its release from the Qdot surface. Photo-activated Qdots can nonradiatively transfer their energy to proximal molecular oxygen to produce singlet oxygen. This can later produce ROS such as superoxide anions, hydroxyl radicals, and hydrogen peroxides, and result in cell death [83].

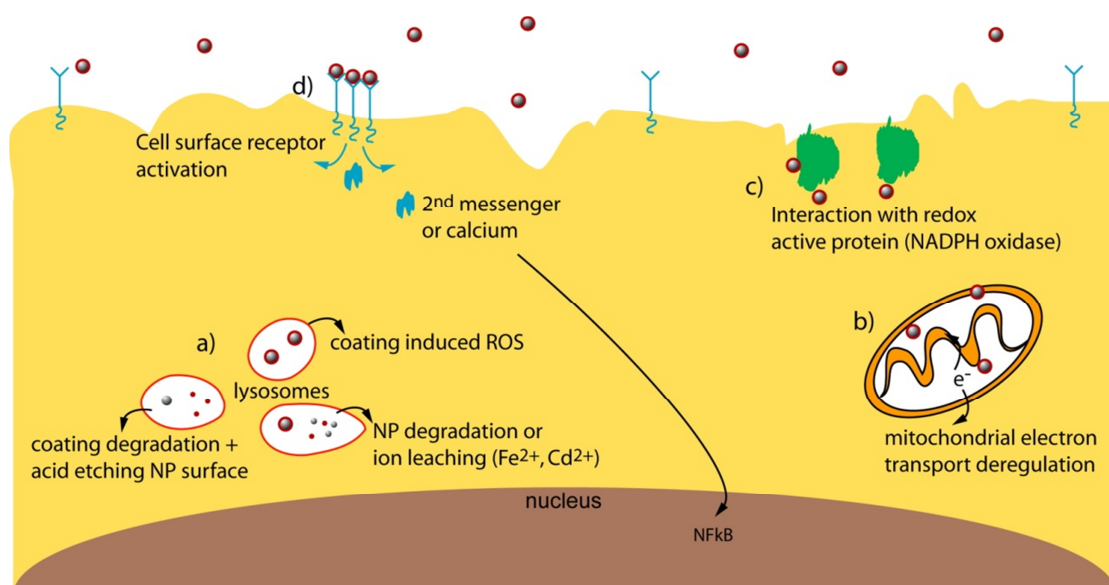


Fig. 12 Schematic overview of the different pathways by which NPs can induce oxidative stress: (a) NPs captured by lysosomes can generate ROS via direct reactivity of their surface coating, degradation of the surface coating or the whole NP in the acidic environment. Degradation of NP surface or itself can release its metal ions (Cd^{2+} , Pb^{2+} , In^{3+} , Fe^{2+}) to the intracellular environment which can in turn give rise to ROS levels by various chemical reactions. (b) NPs can also interact with mitochondria, destabilize its outer membrane, and can cause irregularities in electron transport chain of the oxidative phosphorylation. (c) NPs can directly interact with redox active proteins such as NADPH oxidase, therefore, can induce excess ROS formation in the immune cells [80]. (d) NPs can also cause receptor activation and following to that triggering intracellular signalling cascades by binding to cell surface receptors. This can result in upregulation of ROS by expression of stress-responsive genes [81]. Reprinted from reference [77].

Apart from photo-oxidative processes, stability of surface coating molecules, effectiveness of surface coverage, and presence of a protective inert shell material also play a significant role for the release of metal ions to the intracellular environment. As the Qdots are internalized by the cells, they are confined in intracellular vesicles. Upon their entrapment in the vesicles, their surrounding pH shifts from 7.4 to 6.0 (early endosomes) and 4.5 (lysosomes). The acidic environment in lysosomes can lead to acid-etching process, which will result in degradation of surface coating ligands, and Qdots itself [84]. Along with that, Qdots are also exposed to various degradative enzymes, such as cathepsin L [85]. These degradation processes may lead to generation of free metal ions from Qdot structure, and apart from that, a complete loss of Qdot functionality [78]. However, metal ion leaching is not solely responsible for the cytotoxicity of Qdots. A study reported by Cho *et al.* showed that CdCl₂ salt and Cd-based Qdots exhibited different side effects on metabolic activity of the cells. CdCl₂ salt showed a linear intracellular Cd²⁺ ion concentration, whereas Qdots showed a non-linear dose-dependent correlation. This was attributed to the fact that toxic effects of Qdots did not only originate from metal ion leaching [86]. This observation was later supported by Stern *et al.* [87], Chen *et al.* [82], and Domingos *et al.* [88], pointing out that the whole Qdot with regard to its distribution in cellular subcompartments, such as lysosomes, endosomes, cytosol, and mitochondria, must be taken into account in terms of toxic features of Qdots. Furthermore, Bradburne *et al.* demonstrated that accumulation of Qdot aggregates on the cell membrane can impair cellular processes *via* disturbing cell membrane integrity [89]. Alterations of cell morphologies and deformation of cell cytoskeleton have also been reported for Qdots [73, 90]. For instance, according to Mahto and co-workers, CdSe/ZnSe Qdots caused significant structural changes in actin and tubulin networks in fibroblast cells [91]. The degree of Qdot toxicity depends on the colloidal stability of Qdots, therefore, deposition of passivating shell layers (e.g. ZnS) and development of surface-related characteristics of Qdots (e.g. polymer coating with PEG molecules, microencapsulation) comprise substantial advances at the first step to avoid or at least slow down the decomposition of Qdots in intracellular environments [39, 92-94]. Main Qdot characteristics, e.g. size, shape, purity, colloidal stability, surface charge and chemistry, which play crucial role for the minimization of Qdot-induced cytotoxicity, are schematized in **Fig. 13**.

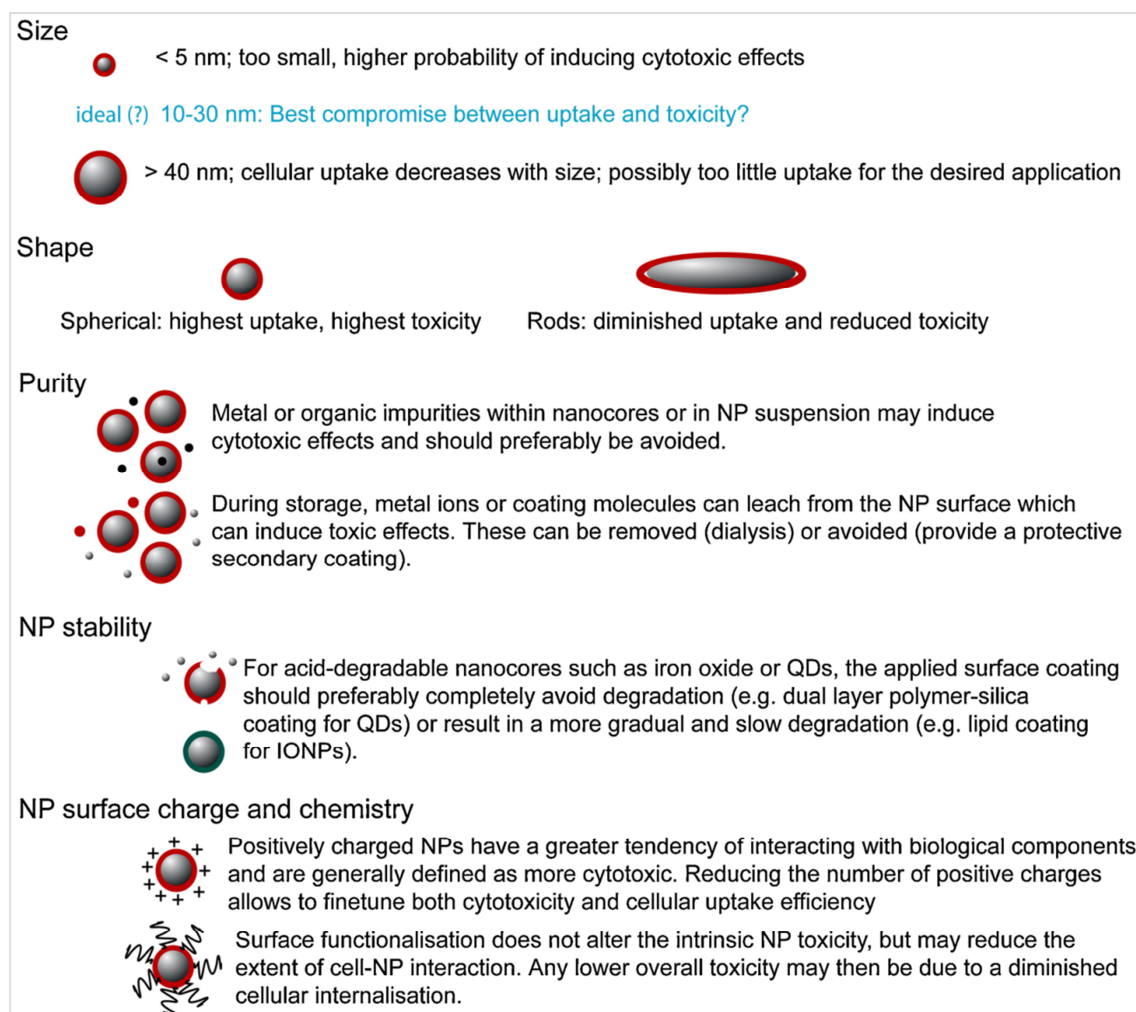


Fig. 13 Schematic overview of NP-related characteristics that minimize NP-induced cytotoxicity, e.g. size, shape, purity, colloidal stability, surface charge and surface chemistry. Reprinted from reference [77].

3.6. Features of Qdots as bio-imaging and therapeutic agents

Utilization of Qdots as fluorescence contrast agents for imaging and/or nanoscale vehicles for delivery of therapeutics have advanced the field of molecular theranostics. The high surface-to-volume ratio of Qdots enables the construction of ‘smart’ multifunctional nanoplatforms, where the Qdots serve not only as an imaging agent but also a nanoscaffold hosting therapeutic and diagnostic modalities [95]. Nowadays, physicochemical and optical properties of Qdots can be manipulated in order to confer Qdots desired functionality (size, emission wavelength, fluorescence intensity, and surface chemistry). Qdots with an enhanced brightness and improved stability play a critical role in utilization of Qdot probes for quantitative bioanalytics, single-molecule

detection, real-time molecular tracking, temperature/pH/oxygen sensing, *in vivo* imaging, drug delivery, and photothermal therapy [96, 97]. In addition, the unique electronic structure of Qdots and availability of high surface area for adsorption allow the resonance transfer of electrons across the molecules, making Qdots ideal candidate in fluorescence resonance energy transfer (FRET) quenching assays for sensing applications [98, 99]. When compared to conventional organic fluorophores, Qdots; (i) are 10-20 times brighter with high quantum yields, (ii) have broad absorption spectrum that allows free selection of the excitation wavelength and thus enables direct separation of excitation and emission, and simultaneous excitation of multiple colours, (iii) have 10-50 times higher molar absorption coefficients, (iv) possess longer fluorescence lifetimes and larger Stokes shifts (the distance between emission and excitation peaks) enabling straightforward discrimination of the signal from cellular autofluorescence and scattered excitation light, thereby enhancing the sensitivity, (v) have higher resistance against photo-oxidation making Qdots suitable for continuous real-time tracking studies over a long period of time [100-103]. Although, to achieve high level of sensitivity, specificity and multiplexibility for *in vitro* and/or *in vivo* cellular imaging studies, a site selective targeting of Qdots is required. This emphasizes the vital need for controlled surface functionalization of Qdots [103].

Water-soluble Qdots carry various chemical moieties (i.e. $-\text{SH}$, $-\text{NH}_2$, $-\text{COOH}$, and $-\text{OH}$) that bring Qdots a great functionality for their conjugation with biomolecules. Through an appropriate selection of targeting molecules and efficient cross-linking chemistry, the obtained bioconjugated-Qdots can target and label any structures, compartments, and molecules in cells [104]. A huge variety of suitable cross-linking reactions can be found in textbooks [105]. An overview of the different surface coating strategies and functionalization pathways are summarized in **Fig. 14** [33], and detailed additional information about the principles of covalent and noncovalent binding of biomolecules to the surface of functionalized Qdots is reviewed elsewhere [42, 45, 96, 102, 103, 106].

Recent studies demonstrating application of conjugated-Qdots with various biological molecules of interest (e.g. biotin, folic acid, cell-penetrating peptides, antibodies, proteins, enzymes, or DNA) in imaging, single molecule tracking, drug delivery, and sensing are listed in **Table 1**.

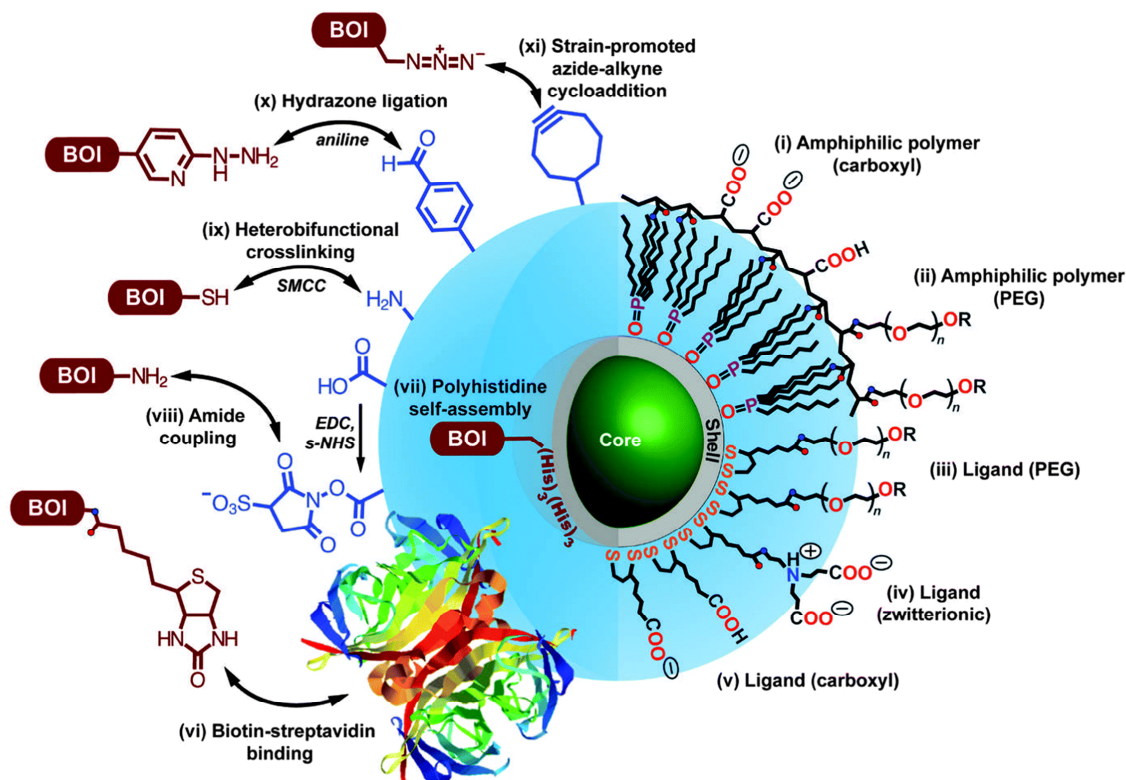


Fig. 14 Overview of different surface coating (right side) and bioconjugation strategies for core/shell Qdots. Surface coating molecules are as follows: amphiphilic polymer coating with (i) carboxyl(ate) groups; (ii) PEG ligands; coordination of shell Zn^{2+} ions with dithiol-ligands containing (iii) PEG molecule; (iv) zwitterionic functionality; (v) carboxyl(ate) groups. R groups include carboxyl, amine, thiol, or methoxy moieties. Conjugation methods for biomolecules of interest (BOI) to the surface of Qdot are as follows: biotin-streptavidin binding; (vii) polyhistidine self-assembly; (viii) amide coupling using EDC/s-NHS activation; (ix) heterobifunctional cross-linking using succinimidyl-4-(N-maleimidomethyl)cyclohexane-1-carboxylate (SMCC); (x) aniline-catalyzed hydrazone ligation; and (xi) strain-promoted azide-alkyne cycloaddition. Reprinted from reference [33].

Emission profiles of Qdots can be tuned to lie within the biological window (700–1100 nm), where tissues do not scatter the light as much as in the UV–visible, and there is less absorption and almost no autofluorescence. Employing near-infrared (NIR) emitting Qdots for *in vivo* imaging could potentially help in monitoring deeper cellular compartments on the order of centimeters with a minimum damage to the cells [29, 122]. NIR Qdots (e.g. CdTe, CdHgTe, HgTe, InP, PbS, PbSe, PbTe, Ag₂S, or AgSe) can be easily prepared by manipulation of synthesis protocols, material compositions, and sizes. This feature has been the key point for Qdots as it has broadened the utilization of Qdots for bioanalytical studies, and also has been the driven force for the design and development of high-quality NIR Qdots for *in vivo* studies [123]. There have been many successful applications of NIR Qdots in biological imaging studies ranging from tumor imaging, to single molecule tracking and photothermal therapy.

Table 1. Recent advances in the application of bioconjugated-Qdots in imaging, sensing, and theranostics.

Composition of Qdot	Bioconjugated molecule	Application
Ni-doped CdTeSe/CdS coated with amino- and carboxyl-PEG ligands	Folic acid	Simultaneous targeted cancer cell imaging and magnet-assisted cellular sorting [107]
SiO ₂ coated CdTe/ZnS	IgG through avidin-biotin connection	<i>In vitro</i> live cell imaging [108]
CdTe/ZnS coated with amphiphilic polymer	Anti-CD3	Selective application of T-cells [109]
CdSeTe/ZnS coated with amino-PEG ligands	Vascular cell adhesion molecule-1 binding peptide (VCAM-1 binding peptide)	<i>In vivo</i> and <i>in vitro</i> imaging of VCAM-1-expressing endothelial cells [110]
Zn _x Hg _{1-x} Se coated with MPA	Proteins (e.g. transferrin, hemoglobin, trypsin, lysozyme, serum albumin, folic acid)	Live cell imaging [111]
CdSe/ZnS coated with amphiphilic polymer	BRCA1 and Her2 antibody	<i>In vivo</i> gastric cancer imaging [112]
CdSe/ZnS modified with streptavidin	Biotin– H9N2 virus	Monitoring the immune responses of the infected cells [113]
CdSe/ZnCdS coated with DHLA-PEG derivatives	Streptavidin	Synaptic receptor tracking in live neurons [114]
CdTe/CdS coated with MPA	Thiolated-DNA	Nanosensor for nucleic acid detection [115]
CdTe/ZnS coated with amphiphilic polymer	Horseradish peroxidase	Determination of hydrogen peroxide and glucose [116]
CdSe/ZnSe functionalized with L-arginin/L-histidin/β-cyclodextrin	Doxorubicin (Dox) and siRNA	Delivery of Dox and siRNA to reduce multidrug resistance in cancer cells, and real-time tracking [117]
CdSe/ZnS coated with amphiphilic polymer	Cy3-labelled cell-penetrating peptide	Profiling matrix metalloproteinase activity at single cancer cell membrane [118]
InP/ZnS coated with PEG lipids	Arginine-rich cell-penetrating peptide	Intracellular delivery and targeted imaging of tumor cells [119]
CdSe/ZnS modified with streptavidin	Biotinylated anti-human CD29 and CD44 antibody	Monitoring migration mechanism of mesenchymal stem cells [120]
Poly(L-lactide) (PLA) and PEG-grafted graphene Qdots	Molecular beacon (specific-gene probes)	Intracellular miRNAs imaging and gene therapy [121]

For instance, Hu *et al.* prepared alloyed $\text{CdTe}_{1-x}\text{Se}_x/\text{CdS}$ NIR-emitting Qdots *via* organometallic synthesis approach. Water dispersion of the Qdots was accomplished by their encapsulation with PEG-grafted phospholipid micelles. Later, Qdots were coupled with cyclic arginine–glycine–aspartic acid (cRGD) peptide against $\alpha_v\beta_3$ integrins, and successfully applied for targeted *in vivo* imaging of angiogenic tumor vasculatures [124]. Another study by Chu *et al.* presented versatility of silica-coated CdTe NIR Qdots for the treatment of *in vivo* mouse melanoma tumor using photothermal therapy [125]. They demonstrated that Qdots irradiated by a 671-nm laser could effectively convert light energy into heat in combination with generating intracellular ROS. As a result, photothermal conversion of the irradiated light by Qdots as well as generation of ROS resulted in the cell death. Furthermore, Hu *et al.* established targeted *in vivo* tumor imaging *via* PEGylated phospholipid micelle-encapsulated NIR PbS Qdots [126]. Another study showed that MUA/MPA-modified CdSe/ZnS Qdots tagged with reduced graphene oxide (rGO) composites demonstrated promising photothermal therapeutic

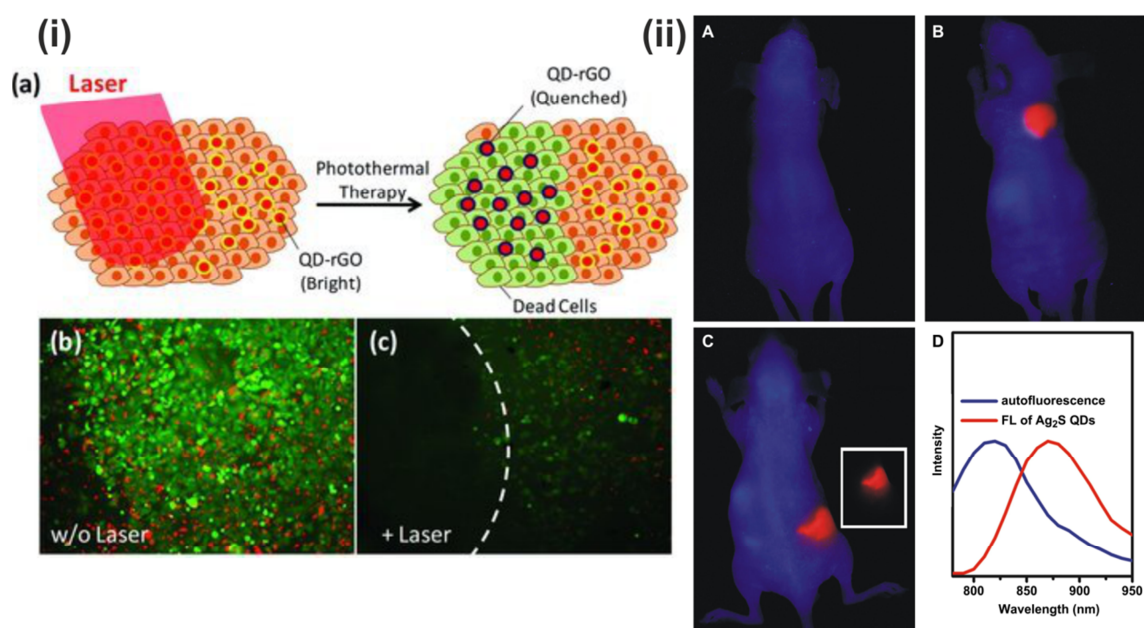


Fig. 15 Application of NIR Qdots in *in vivo* imaging and photothermal therapy: (i) Photothermal therapy efficiency of Qdots-rGO nanocomposites: (a) Schematic illustration of Qdot-rGO labelled MCF-7 cells exposed to irradiation (left) and after irradiation of Qdot-rGO causing cell death; (b) before irradiation cells were labelled with folic acid-targeted Qdot-rGO (red) and propidium (green) for live cell imaging; (c) after irradiation at 808 nm for 4 min, the area on the left side of marked line shows the fluorescence signal was diminished and the cells lost their viability. Reprinted from reference [127]. (ii) *In vivo* NIR fluorescence imaging of nude mice with water-soluble Ag₂S Qdots (emission at 910 nm): (A) control experiment, (B) with subcutaneous injection of Ag₂S Qdots, and (C) with celiac injection of Ag₂S Qdots (C, inset) shows the fluorescence signal of Qdots. (D) Corresponding emission spectra of autofluorescence of mice (blue) and Qdots labelled mice (red). Reprinted from reference [66].

activity on MCF-7 breast adenocarcinoma cells after 4 min laser irradiation (**Fig. 15i**) [127]. Moreover, Jiang *et al.* developed MPA-functionalized Ag₂S NIR Qdots with tunable emission wavelengths in the range of 510-1221 nm [66]. The as-prepared Qdots accumulated to nude mice, suggesting that the Ag₂S Qdots have a great potential for *in vivo* imaging (**Fig. 15ii**). Also, their heavy metal-free composition holds significant advantage for their minimized toxicity in comparison to heavy-metal containing Qdots [128]. Very recently, Yang *et al.* showed the synthesis of GSH-capped NIR HgS Qdots and the deposition of ZnS shell to improve fluorescence yield of the Qdots [129]. According to their result, the growth of the ZnS shell around HgS Qdots converted poorly fluorescence HgS Qdots into ultra-bright HgS/ZnS Qdots with quantum yield up to 43.8%. Moreover, fluorescence could be detected up to a depth of 2 cm within the tissue, proving that the developed Qdots are effective fluorescent labels for *in vitro* and *in vivo* imaging. Yet, another study from Duman and co-workers showed the transfection efficiency of MPA/PEI modified Ag₂S NIR Qdots [130]. The Qdots with low-toxicity exhibited 40% efficiency for the transfection of green fluorescence protein plasmid (pGFP) to HeLa and MCF-7 cell lines. The authors concluded that Ag₂S NIR Qdots showed great potential as new tools for theranostics.

3.7. Future aspects in Qdot development

Heavy-metal containing composition of Qdots has induced a great debate about the biocompatibility of Qdots in biological applications. Intrinsic toxicity of Qdots due to their hazardous element contents (cadmium, lead) has raised many questions in the scientific community about their possible risks [131]. The safety concerns for the environment and human health enforced the search for alternative ultra-stable nanocrystals with similar imaging performances, particularly in the NIR region. On this basis, recent studies for nanoprobe design have been concentrated on the synthesis of silica Qdots (Si-Qdots), carbon Qdots (C-Qdots), and organic Qdots. Si-Qdots with intrinsic biocompatibility and biodegradability in the environment represent attractive tools for bio-imaging studies. However, their low stability in physiological conditions remains a challenge in the development of stable Si-Qdots for long-term applications. Nevertheless, recent studies have made promising progress on the synthesis and development of water-soluble, stable, and highly fluorescence Si-Qdots [131-134], and

in their application for *in vivo* tumor imaging and drug delivery studies [135-137]. Very importantly, the U.S. Food and Drug Administration (FDA) recently approved the first clinical trial of PEG-coated Si-Qdots in humans which are developed at Cornell University (USA), so-called Cornell Dots. The trial involves five melanoma patients and will seek to verify that the Si-Qdots are safe and effective [138]. Yet, long-term effect of Si-Qdots in the body and their possibility to irritate lungs and initiate cancer themselves are one of the main concerns standing ahead of their use in humans.

Carbon quantum dots (C-Qdots) are a new class of carbon nanomaterials that have emerged recently as alternative to the conventional inorganic Qdots [139]. After their accidental discovery during the purification of single-walled carbon nanotubes by Xu *et al.* in 2004 [140], subsequent studies have been conducted to exploit the fluorescence properties of C-Qdots [141]. Their low toxicity, environmental friendliness, simple synthetic routes, tunable physicochemical properties, and surface functionality [142-145] have triggered their applications in the fields of biosensing [145], bio-imaging [147, 148], nanomedicine [145, 149-152], photo- and electro-catalysis [153]. A major challenge in C-Qdot research is the synthesis of NIR C-Qdots with brighter fluorescence emissions because of their low quantum yields. Therefore, future studies will be performed to enhance the quantum yield of C-Qdots, and to prepare C-Qdots with controlled shape, size and surface functionalities [141].

Organic Qdots that are fabricated from organic pigment molecules (indigos, quinacridones, and phthalocyanines) offer a cheap, less toxic and environment-friendly alternative to inorganic Qdots [154, 155]. Perylenes and their derivatives represent a showcase example as they are synthesized *via* typical colloidal chemical reactions in the presence of surface ligands. Moreover, the introduction of surface ligands allows surface functionality, size, and shape control [156, 157]. As a result, they display optical absorption and tunable photoluminescence properties across the visible to near-infrared region. Although the development of organic Qdots hasn't been advanced as far as that of inorganic Qdots, it is believed that they might pave the way toward a new generation of solution processed organic nanomaterials, benefiting from the high robustness of these materials, their optical and semiconducting properties, and their facile preparation methods [155, 158, 159].

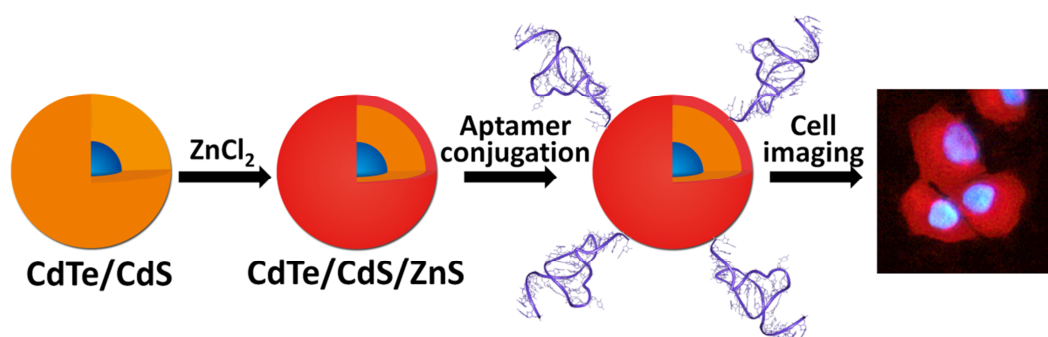
4. Experimental Investigations

The aim of this work is to develop water-soluble Qdots with enhanced optical properties and improved surface characteristics to fortify their application in fluorescence imaging studies, as well as to increase their biocompatibility. The results of this research project are presented in three chapters. The first chapter (4.1) summarizes the aqueous synthesis and characterization of 3-mercaptopropionic acid-functionalized CdTe/CdS and CdTe/CdS/ZnS Qdots, effect of ZnS shell on cytotoxicity and photostability of Qdots, and their application in targeted fluorescence imaging studies. The second chapter (4.2) addresses the dose-dependent cytotoxicity effects of Qdots on 3D spheroid cultures and applicability of Qdots to label 3D spheroid structures. The third chapter (4.3) covers the surface modification of Qdots with mPEG molecules to improve surface-related characteristics of Qdots, e.g. colloidal stability, toxicity, non-specific cell binding.

4.1. Aqueous synthesis of Qdots and their application in targeted imaging

The results of this chapter were published as Ulusoy et al., One-pot aqueous synthesis of highly strained CdTe/CdS/ZnS nanocrystals and their interactions with cells, *RSC Advances*, 2015, 5, 7485. It was reproduced by permission of The Royal Society of Chemistry.

Table of Contents Graphic



An aqueous approach enhancing the properties of small-core/thick-shell CdTe/CdS nanocrystals by deposition of an outer ZnS shell was developed. The as-prepared nanocrystals were conjugated with aptamer for the targeted imaging of cancer cells.

4.1.1. Summary

Optical properties of core nanocrystals (NCs) or quantum dots (Qdots), e.g. fluorescence wavelength, quantum yield, and lifetime, can be tuned by growing an epitaxial shell of another semiconductor material with a wide-band gap. This strategy provides a significant progress on the chemical synthesis of core/shell (CS) Qdots. Near-infrared (NIR) emitting Qdots composed of magic-core/thick-shell have been classified as a new type of nanocrystals exhibiting excellent lattice strain-induced optical properties. They feature great tunability and improved fluorescence lifetimes. However, extended excited-state lifetimes can increase the probability of non-radiative recombination events, causing a decrease in fluorescence efficiency. Therefore, overgrowth of an external shell, creating a core/shell/shell (CSS) system, can eliminate the problem while maintaining the spectral tuning properties.

In this study, this new strategy for the generation of magic-core/thick-shell Qdots was followed to fabricate NIR emitting water-soluble core/shell/shell Qdots. For that, a facile one-pot aqueous approach was developed to synthesize CdTe/CdS/ZnS core_(small)/shell_(thick)/shell_(thin) Qdots. In the first step, 3-mercaptopropionic acid (MPA)-functionalized CdTe_(small)/CdS_(thick) CS Qdots with emission wavelengths up to 750 nm were synthesized. For their synthesis, a rich Cd-thiol environment with very low Te-to-Cd molar ratio was created to facilitate consecutive formation of a magic-sized CdTe core and a thick CdS shell. As-prepared CdTe_(small)/CdS_(thick) Qdots exhibited very bright emission colors with a maximum quantum yield (QY%) of 57%. In the following step, the obtained crude solution was used for deposition of a ZnS outer shell. For that, a Zn²⁺ source was simply injected into the crude CS Qdots solution, and the reaction was proceeded for 6 h. As a result, high quality CdTe_(small)/CdS_(thick)/ZnS_(thin) CSS Qdots emitting in the red-to-near infrared window were obtained with improved fluorescence efficiency (QY_{max} ~ 64%). The as-prepared Qdots also demonstrated good monodispersity by exhibiting narrow emission bands with a maximum FWHM (full width at half maximum) values at 80 nm. X-ray powder diffraction (XRD) analysis and high-resolution transmission electron microscope (HRTEM) images showed the crystalline structure of as-prepared Qdots, and successful deposition of the ZnS shell without significant crystalline defects. Later, CdTe/CdS and their respective CdTe/CdS/ZnS Qdots were tested for their stability against photo-oxidation. Under continuous irradiation with UV light for 5 h, Qdots exhibited neither a decrease in fluorescence intensity nor a blue-shift in emission wavelengths. However, instead of photo-degradation, they displayed a photo-annealing process under UV-irradiation.

Qdots were further characterized for their size- and composition-dependent *in vitro* cytotoxicity to conventional A549 adenocarcinoma cell cultures. The cell viability results obtained from CellTiter-Blue (CTB) assay revealed that the smaller Qdots showed increased toxicity when compared to their larger counterparts. Moreover, overgrowth of the ZnS shell reduced the toxicity of Qdots, and an increase in ZnS shell thickness resulted in a concomitant decrease in Qdot-induced toxicity. Later, the as-prepared CdTe/CdS/ZnS Qdots were coupled with DNA aptamer molecules against A549 adenocarcinoma cells to test their performances in targeted cell imaging studies. Qdot modified with a random oligonucleotide was used as the negative control conjugate. Fluorescence

microscopy studies showed that aptamer–Qdot bioconjugates were successfully uptaken by A549 cells, whereas the negative control samples weren't internalized by the cells within the given incubation conditions. Promisingly, the aptamer-Qdot bioconjugates maintained their brightness after 24 h of internalization, proving their structural stability in intracellular environment.

In conclusion, epitaxial growth of the ZnS shell over CdTe/CdS Qdots provided a physical barrier between the optically active core/shell material and the surrounding medium, thus making the Qdots less sensitive to environmental changes. The ZnS shell further enabled an efficient passivation of the surface trap states, giving rise to a strongly enhanced fluorescence quantum yield. Furthermore, aptamer-conjugated Qdots were successfully utilized in targeted cell imaging, proving that the developed Qdot represents a suitable candidate as a fluorescent probe for bio-imaging applications.

4.1.2. Abstract

In this work, a very simple one-pot synthetic approach was developed to generate aqueous CdTe/CdS/ZnS type-II/type-I red-emitting nanocrystals (NCs). Strain-induced optical properties of CdTe/CdS particles having core_(small)/shell_(thick) structure with a maximum quantum yield (QY_{\max}) ~ 57% were further improved with the overgrowth of a ZnS shell, resulting in a core_(small)/shell_(thick)/shell_(small) structure (QY_{\max} ~ 64%). The spectral properties were tuned further to the near-infrared region as the ZnS shell grew in thickness. X-ray powder diffraction (XRD) analysis and high-resolution transmission electron microscope (HRTEM) images showed the crystalline structure of NCs proving the epitaxial growth of ZnS without crystalline defects. Under continuous UV-irradiation for 5 h, the NCs did not exhibit any photodegradation but instead displayed a photo-annealing process. These extremely photostable NCs were further characterized in terms of their cytotoxicity and their cell labeling performances. The presence of a ZnS shell was found to reduce the toxicity of the CdTe/CdS NCs. Furthermore, aptamer–conjugated NCs were successfully utilized in targeted cell imaging. Promisingly, the aptamer–NCs bioconjugates were internalized by A549 cells within 2 hours of incubation and retained their fluorescence even after 24 hours of internalization.

4.1.3. Introduction

Core/shell (CS) semiconductor nanocrystals (NCs) emitting in the near-infrared range are of particular interest owing to their deep tissue penetration which is important in biomedical imaging applications. Recent studies have mostly concentrated on developing new strategies which allow simple manufacturing of NCs with large spectral shifts. By using the lattice strain between a small soft core (CdTe) and a thick compressive shell (ZnS, CdS, ZnSe, CdSe), Nie and coworkers presented a new class of core_(small)/shell_(thick) NCs displaying type-II behavior with greater photostability and giant spectral shifts in comparison to traditional core_(small)/shell_(thick) NCs [1]. When the small CdTe core is subjected to a large stress arising from the epitaxial overgrowth of a lattice-mismatched shell, the CdTe core can overcome this stress due to its elasticity while maintaining excellent spectral properties without causing any defect trap sites. The first aqueous synthesis of CdTe/CdS so-called ‘magic-core/thick-shell’ NIR emitting NCs was reported by Deng and coworkers [2]. They first synthesized magic sized CdTe clusters (~ 0.8 nm), then deposited a thick CdS shell with thickness up to 5 nm creating magic-core/thick-shell NCs with very large spectral shifts and high fluorescence efficiencies. A further study was reported by Chen *et al.* who used an air-stable Te source (Na₂TeO₃) instead of NaH₂Te resulting in a much simpler route to one-pot synthesis of NIR emitting CdTe_(small)/CdS_(thick) NCs within a reaction time of up to 24 h [3].

In type-II systems, despite the greater tunability of emission wavelengths and improved fluorescence lifetimes, extended excited-state lifetimes can increase the probability of nonradiative recombination events. One of the separated charge carriers which is confined in the shell region can very likely be trapped in the surface defect sites which further causes the inevitable decrease in fluorescence efficiency [1]. Therefore, the growth of an external shell, resulting in a core/shell/shell (CSS) system, with a wide bandgap serving as an outer protection layer can create more stable NCs while maintaining the lattice strain induced spectral tuning properties [4]. Taking this into consideration, core_(small)/shell_(thick)/shell type-II/type-I CSS NCs can be classified as a new generation of NCs with better optical and structural characteristics. For the fabrication of a CSS structure, zinc sulfide has traditionally been the shell material of choice due to its chemical inertness and negligible toxicity, which attracts specific interest in biological applications [5, 6]. Its wide bandgap energy assures efficient

passivation and charge-carrier confinement preventing electron-hole delocalization towards the outer surface, which is hindered by surface traps that reduce fluorescence quantum yields. As a result, a ZnS shell improves chemical stability as well as the optical properties of NCs [7].

On this basis, a preliminary study was published by Green *et al.* using the aqueous overgrowth of a ZnS shell around CdTe/CdS NCs in 24 h [8]. Very recently, this strategy was further improved by Zhu and coworkers with microwave-assisted irradiation of CdSeTe_(small)/CdS_(thick) CS NCs and further deposition of a very thin ZnS shell [9]. As a result, QY values were increased by a further ~ 4% to 63% with the overgrowth of a ZnS shell and growth rates were remarkably accelerated in the aqueous phase. However, microwave irradiation is limited in scale-up production and on-line monitoring of the reaction process. Therefore, development of a rapid, facile and user-friendly route to produce high quality water-soluble NCs, especially those of emission wavelengths in the red to near-infrared range, is still highly desirable for the efficient and safe applications of NCs in bio-imaging studies.

Herein, we followed this new generation of magic-core/thick-shell NCs and developed this further for the fabrication of NIR emitting water-dispersed CSS NCs. We have developed a simplified strategy to synthesize core_(small)/shell_(thick)/shell NCs composed of CdTe/CdS/ZnS based on conventional methods. First, by creating a rich Cd-thiol environment with a very low Te-to-Cd molar ratio, a one-pot aqueous synthesis of type-II CdTe_(small)/CdS_(thick) with emission wavelengths up to 750 nm (QY_{max} ~ 57%) was achieved. Afterwards, an outer ZnS shell was grown over the CS NCs by simply injecting a Zn source directly into the crude CS NCs solution. After 3 h of reaction, high quality CdTe_(small)/CdS_(thick)/ZnS_(thin) CSS NCs emitting in the red-to-near infrared window were obtained with improved fluorescence efficiency (QY_{max} ~ 64%). As a result, the one-pot synthesis of highly tunable NIR emitting type-II/type-I CdTe/CdS/ZnS CSS NCs with a very narrow FWHM (full width at half maximum) values (max. 80 nm) and high quantum yields was performed without precursor injection and purification steps.

These improved optical properties allowed us to successfully implement these NCs in targeted cell imaging after conjugation with S15 DNA aptamers which specifically bound to lung cancer cells [10]. Aptamers are short, single-stranded oligonucleotides generated from an *in vitro* process known as SELEX (Systematic Evolution of Ligands by Exponential enrichment) [11]. Their high binding affinity and selectivity towards

numerous targets, including small molecules, proteins, receptors, and cells in addition to their chemical stability, economic production and convenient modification introduced aptamers as a novel type of recognition molecules [10]. There are various successful reports presenting the efficiency of aptamer conjugated nanoparticles for sensing [7, 12–15], imaging and therapeutic applications [16–19]. Fluorescence microscopy studies showed the effective up-take of aptamer–NCs bioconjugates by A549 lung cancer cells.

4.1.4. Results and discussion

Production and optical analysis of NCs

For the one-pot synthesis of CdTe_(small)/CdS_(thick) NCs, a Cd-rich environment was created by using a very low Te-to-Cd (1 : 25) molar ratio. 3-Mercaptopropionic acid (MPA) was utilized as a sulphur source as well as the surface functionalization agent. At the early stage of particle growth, the usage of a very low Te-to-Cd molar ratio resulted in the formation of a small population of small particles [20]. In this case, depletion of free monomers proceeded slower than in the case of higher Te-to-Cd ratios. The extended depletion time of monomers avoided the Oswald ripening process, a process which originated from a slow-growth rate, resulting in a broadening of size distributions [21]. At this early stage of crystal growth, the monomer concentrations should be rather high and addition of monomers to the crystals should be predominant for the growth of particles. In this case, diffusion controlled growth *via* monomer addition facilitates faster growth of smaller particles than the larger ones. Moreover, Cd precursors which are improved by high pH and Te precursor stability support this fast growth process [22]. In regards to the effect of ligand-to-Cd ratio on the growth rate of NCs, the ligand-to-Cd molar ratios lower than 2 : 1 create an environment dominant with monothiol complexes rather than dithiol complexes. Under high pH conditions (>11), these monothiol complexes have greater solubility which improves the release of Cd and therefore support formation of CdTe monomers for nucleation and particle growth. Thus, a fast growth rate is achieved by means of accelerated Cd release for crystal growth under low ligand-to-Cd molar ratios and high pH conditions [22]. Once the Te source is depleted, the remaining Cd-monothiol complexes give a Cd rich surface which supports CdS shell formation around those very small CdTe particles

resulting in core_(small)/shell_(thick) CdTe/CdS nanocrystals. This mechanism explains the high quality optical characteristics obtained by one-pot formation of core/shell (CS) structures.

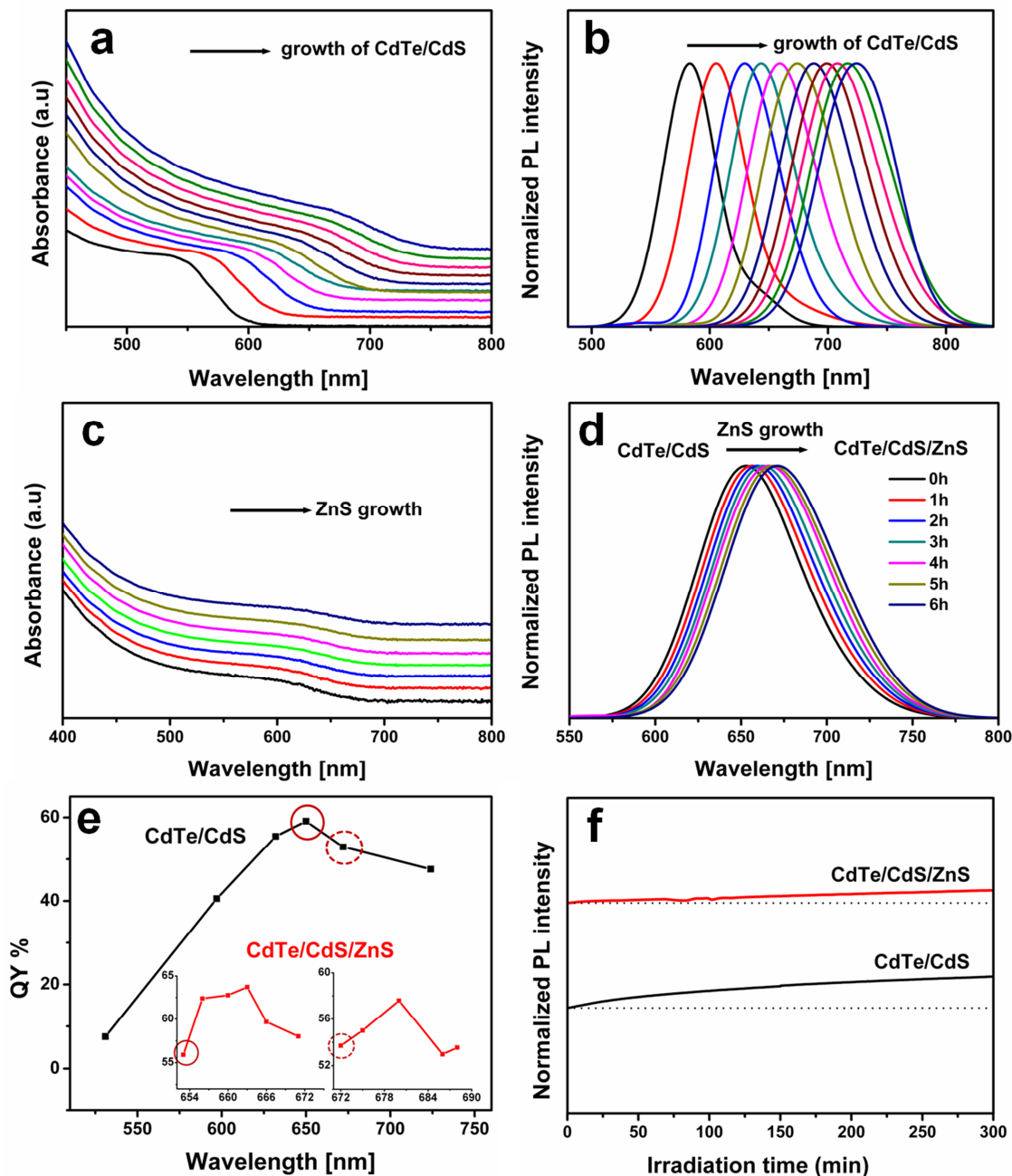


Fig. 1 Optical characteristics of NCs. Absorbance (a) and fluorescence emission spectra of CdTe/CdS CS NCs during particle growth for 6 h (b). Absorbance (c) and fluorescence emission profiles of CdTe/CdS/ZnS CSS NCs during ZnS shell growth for 6 h ($\lambda_{\text{excitation}} = 470$ nm) (d). Fluorescence efficiencies of CS and CSS NCs in terms of quantum yields (QY%) (e). Right insert shows the QY% of CSS NCs deposited on CS NCs ($\lambda_{\text{emission}} = 672$ nm). Left insert shows the QY% of CSS NCs deposited on CS NCs ($\lambda_{\text{emission}} = 652$ nm). Photostability of CS NCs and corresponding CSS NCs during continuous irradiation under UV light at 360 nm for 5 h (f).

Absorbance and fluorescence spectra of the resulting CdTe/CdS NCs, shown in **Fig. 1a** and **b**, reveal the gradual spectral shift to the longer wavelength as the CdS shell proceeded to grow in thickness. Notably, samples did not show a sharp first exciton absorption peak but a featureless profile with the increase of particle size. This complete disappearance of the first exciton absorption peak can be attributed to transition of type-I to type-II behaviour [1]. During this switch, gradual strain induced spectral changes did not exhibit abrupt transformations allowing the preservation of tunability of emission spectra by lattice strain. The soft CdTe core was able to compress elastically as the CdS shell grew in thickness causing a large stress to the core. This elasticity of the very small CdTe core material allowed these NCs to maintain and even improve their optical properties. CdTe/CdS NCs emitting at 730 nm were obtained after 6 h of synthesis at 90 °C. Quantum yields (QY %) reached a maximum value of 57% when the emission wavelength shifted to around 650–660 nm which was followed by a decrease as the CdS shell proceeded to grow further (**Fig. 1e**). It is likely that the CdTe core could no longer withstand the strain without forming surface traps.

Interestingly, when a ZnS shell material with a larger lattice mismatch was overgrown on the surface, the QY started to increase again but only until a certain shell thickness. When the ZnS shell was deposited around CdTe/CdS NCs having a $QY_{\max} \sim 57\%$ ($\lambda_{\text{emission}} = \sim 650\text{--}660$ nm), the resulting CSS NCs exhibited improved fluorescence behaviour with a $QY_{\max} \sim 64\%$ (**Fig. 1e**, left-inset). Later, another CS NCs having a reduced QY $\sim 53\%$ ($\lambda_{\text{emission}} = 672$ nm) was used for the ZnS shell formation. Again, the fluorescence efficiency of the resulting CSS NCs was improved further to a $QY_{\max} \sim 57\%$ (**Fig. 1e**, right-inset). To the best of our knowledge, the obtained optical yields for the water-dispersed red-emitting CdTe/CdS/ZnS NCs are one of the highest values in comparison to the literature values (**Table 1**). These results indicated that epitaxial growth of a ZnS shell around a CdS shell improved the surface structure of NCs by passivating the dangling bonds on the surface. However, we should note that the big lattice mismatch (16.4%) between CdTe and ZnS did not allow us to grow a thick epitaxial ZnS shell without crystalline defects. After a very thin ZnS formation, NCs could not maintain their excellent fluorescence efficiencies causing reduced QY values. It is remarkable that highly strained CdTe/CdS/ZnS CSS heterostructures exhibit excellent photoluminescence properties especially when it is considered that crystallinity of the core and the homogeneity of shells were achieved at very low

Table 1. Comparison of optical properties of core/shell/shell NCs synthesized with aqueous approaches

Core/shell/shell structure	Emission	QY _{max} %	Synthetic route	Reference
CdTe _(large) /CdS _(thin) /ZnS _(thin)	615 nm	43	microwave (step-wise)	He <i>et al.</i> , 2008 (ref. 23)
CdTe _(large) /CdS _(thick) /ZnS _(thin)	660 nm	n.d ^a	conventional (one-pot)	Green <i>et al.</i> , 2009 (ref. 8)
CdTe _(large) /CdS _(thin) /ZnS _(thin)	615 nm	45	autoclave/conventional	Tian <i>et al.</i> , 2010 (ref. 24)
CdTe _(large) /CdS _(thin) /ZnS _(thin)	625 nm	42	conventional (step-wise)	Li <i>et al.</i> , 2011 (ref. 25)
CdTe _(large) /CdSe _(thin) /ZnSe _(thin)	670 nm	<5	conventional (one-pot)	Green <i>et al.</i> , 2011 (ref. 26)
CdTe _(large) /CdS _(thin) /ZnS _(thin)	613 nm	15	conventional (one-pot)	Zhang <i>et al.</i> , 2012 (ref. 27)
CdSeTe _(small) /CdS _(thick) /ZnS _(thin)	648 nm	63	microwave/conventional	Li <i>et al.</i> , 2013 (ref. 9)
CdTe _(small) /CdS _(thick) /ZnS _(thin)	650-660 nm	64	conventional (one-pot)	present study

^a Not determined.

temperatures under atmospheric conditions. Another promising feature of the external ZnS shell growth is the gradual tuning of the emission spectra to longer wavelengths without formation of any deep-trap emission (**Fig. 1c** and **d**). After 6 h of reaction, emission wavelengths were shifted approximately 16–19 nm to the near-infrared region. As expected from the type-I behaviour of the CdS/ZnS shell/shell heterostructure, the spectral shifts are not as large as in type-II behaving CdTe/CdS core/shell NCs. Moreover, utilization of MPA as a sulphur source for the ZnS shell formation which is already present in the crude CdTe/CdS solution, created more controllable and reproducible shell formation with reduced growth rates in comparison to sodium sulfide (Na₂S). Sodium sulfide has relatively high decomposition rate causing uncontrolled release of sulphur ions and thus a fast growth rate [21]. However, deposition of an even ZnS shell required a slow growth step [8].

Structural analysis of NCs

Diffraction patterns of CS-I (CdTe/CdS, $\lambda_{\text{emission}} = 550$ nm), CS-II (CdTe/CdS, $\lambda_{\text{emission}} = 655$ nm) and its corresponding CSS-I (CdTe/CdS/ZnS, $\lambda_{\text{emission}} = 668$ nm) and CSS-II (CdTe/CdS/ZnS, $\lambda_{\text{emission}} = 687$ nm) NCs revealed that these nanoparticles had a zinc blende cubic crystal structure (**Fig. 2**). For the CS NCs, as the CdS shell grew in thickness, diffraction angles shifted to higher values towards the position of standard CdS diffraction angles. As an outer ZnS shell was grown over CS-II, a further shift of the diffraction peaks to higher angles was observed whilst maintaining the pattern of the cubic lattice. The peak widths and shapes of CSS-I and CSS-II NCs remained

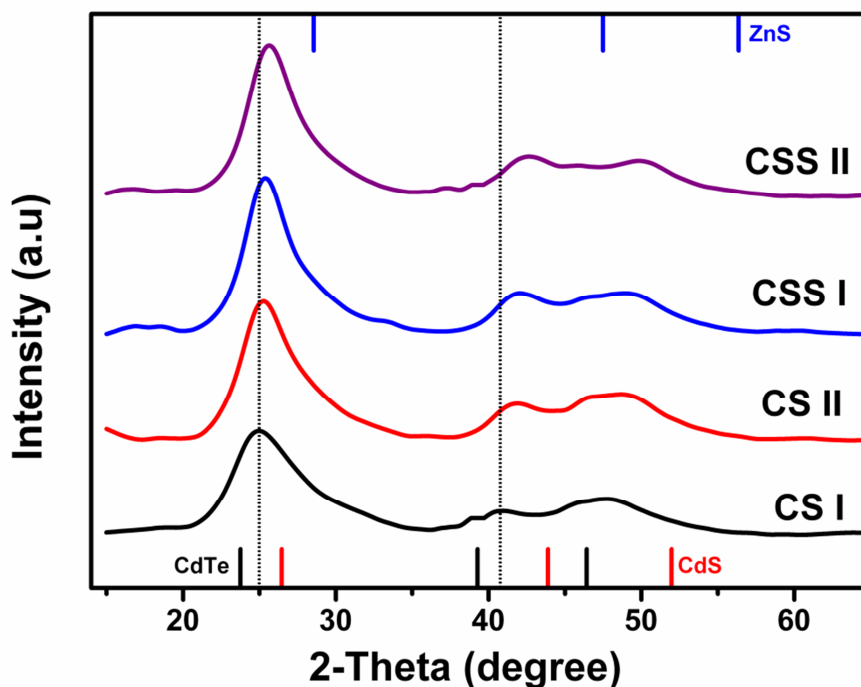


Fig. 2 Diffraction patterns of CS-I (CdTe/CdS, $\lambda_{\text{emission}} = 550$ nm), CS-II (CdTe/CdS, $\lambda_{\text{emission}} = 655$ nm) and its corresponding CSS-I (CdTe/CdS/ZnS, $\lambda_{\text{emission}} = 668$ nm) and CSS-II (CdTe/CdS/ZnS, $\lambda_{\text{emission}} = 687$ nm). The standard diffraction pattern of the reference cubic structures of CdTe (lattice constant $a = 6.4827$ Å), CdS ($a = 5.8304$ Å) and ZnS ($a = 5.4109$ Å) is also shown.

nearly unchanged in comparison to those of the CS nanocrystals, which confirmed the formation of a core/shell/shell structure rather than an alloyed structure. A homogeneous alloy would result in a significant narrowing of XRD peak widths upon increasing particle size [23].

High-resolution transmission electron microscopy (HRTEM) was used to further investigate the morphology and crystal structure of the NCs. **Fig. 3a–d** show low and high magnification TEM images of the as-prepared CdTe/CdS CS NCs, indicating these nanocrystals have either spherical or tetrahedral structures with an average size of 3.68 ± 0.74 nm. HRTEM images of different typical tetrahedral NCs are displayed in **Fig S1†**. The mean crystalline diameter of CdTe/CdS was further confirmed from the line width of the XRD spectrum using Scherrer's formula; $d = 0.94 \lambda / (B \cos \theta_B)$, where λ is the X-ray wavelength ($\text{CuK}\alpha = 1.54$ Å), B is the full width at the half maximum of the diffraction peak (radians), and θ_B is the half angle of the (111) diffraction peak on the 2θ scale [27]. It was calculated to be 3.35 nm which is consistent with TEM size analysis proving NCs have an almost single crystalline structure. HRTEM images of CdTe/CdS/ZnS NCs in **Fig. 3e** and **f** and the indexed fast-Fourier transformation (FFT)

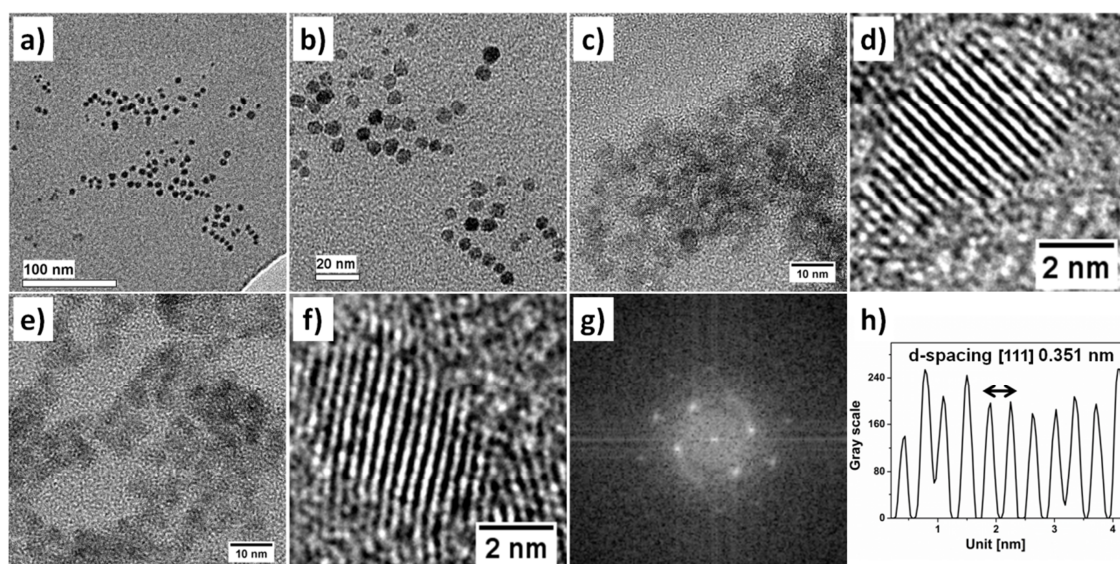


Fig. 3 TEM images of CdTe/CdS NCs with low (a) and high magnifications (b), HRTEM images of CdTe/CdS NCs with a low (c) and a high magnification (d), HRTEM images of CdTe/CdS/ZnS NCs with a low (e) and a high magnification (f), a corresponding fast-Fourier transformation (FFT) profile of CdTe/CdS/ZnS NCs (g) and plotted profile of lattice plane distances along the CdTe/CdS/ZnS lattice lines (h).

feature further confirmed the crystallinity of the NCs with the existence of well-resolved lattice planes. The lattices stretch straight across entire nanocrystals demonstrating coherent epitaxial growth of shell material without forming crystalline defects. Further, atomic force microscopy (AFM) images of CdTe/CdS/ZnS NCs are depicted in **Fig. S2†** showing a topographical view of single nanocrystals. From the TEM images, the average size of CdTe/CdS/ZnS NCs was calculated to be 4.31 ± 0.76 nm. ZnS shell thickness was determined to be 0.31 nm which corresponds to ~ 1.1 monolayers (ML), assuming a monolayer of cubic ZnS is 2.705 \AA (half the cell unit). Resulting NCs will be presented in the following text as CSS (1.0 ML).

The as-prepared CdTe/CdS and CdTe/CdS/ZnS NCs showed an average d-spacing [111] of 0.344 nm and 0.351 nm, respectively, which appeared inbetween the standard interplanar distances of cubic CdTe (0.374 nm) and CdS (0.336 nm). The lattice distances of [111] planes were also estimated by using the Bragg formula of X-ray diffraction which is $d = n\lambda / (2 \sin \theta_B)$, where λ is the X-ray wavelength ($\text{CuK}\alpha = 1.54 \text{ \AA}$), n is an integer, and θ_B is the half scattering angle of the (111) diffraction peak on the 2θ scale. It was found to be 0.353 nm for CdTe/CdS and 0.351 nm for CdTe/CdS/ZnS, which are in good agreement with the lattice spacing values obtained from HRTEM images. These obtained d-spacing values of highly-strained CdTe/CdS/ZnS NCs being shifted towards to lattice spacing of standard cubic CdS

reveals that CSS NCs mostly maintain the structural details of the CdS shell. These results are quite expected when it is considered that the compressive behavior of a CdS shell means it will adopt its bulk lattice parameters once it reaches a thickness large enough to compress the CdTe core [1]. Moreover, the thin ZnS shell (1.0 ML) at the surface adopted the lattice constant of the CdS inner shell and therefore did not exhibit any observable effect on the lattice spacing values of the as-prepared CSS NCs.

Furthermore, time-resolved fluorescence decay curves of CSS NCs were analyzed in order to measure excited-state lifetimes of the as-prepared NCs (**Fig. S3†**). Fluorescence decay curves were fitted by tri-exponential model using the Levenberg–Marquardt algorithm. The fit parameters are listed in **Table S1†**. As a result, CSS NCs feature an average lifetime of 51.7 ns, consistent with a typical type-II structure [2, 9].

Photostability

Photostability studies of CdTe/CdS and corresponding CdTe/CdS/ZnS revealed that both NCs were extremely stable under continuous UV-irradiation for 5 h (**Fig. 1f**). During the irradiation, the fluorescence intensity of CdTe/CdS increased by ~30% of the initial signal whilst the fluorescence intensity of CdTe/CdS/ZnS showed only a ~12% increase. After the irradiation, the emission profiles of the NCs were measured and no significant spectral shifts to the blue region were observed which eliminates the possibility of photo-oxidation (**Fig. S4†**). This increase in fluorescence intensity under irradiation phenomenon can be either attributed to photo-brightening or photo-annealing processes. Photo-annealing is caused by the structural rearrangements at the core/shell interfaces as well as at the surface and, is therefore permanent. On the other hand, photo-brightening effects vanish once the excitation source is removed, thereby being only temporary [28]. Since the fluorescence enhancement was permanent when the UV light was removed, we can assume that the photo-annealing effect is the most likely reason for the increase. Moreover, the photo-annealing effect under irradiation can be more pronounced for the NCs with a higher concentration of surface defects at the particle surface [12]. This reasonably explains the predominant enhancement in fluorescence intensity of CdTe/CdS NCs.

Cytotoxicity

For biomedical applications, the toxicity of Cd-based NCs is a critical point of discussion because of their heavy metal (Cd^{2+} , Te^{2-}) containing composition [29].

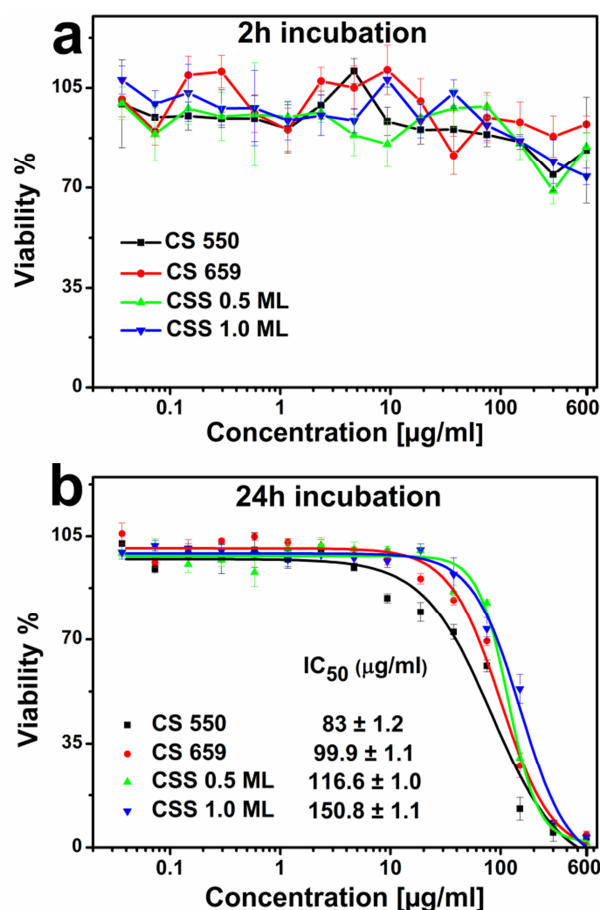


Fig. 4 Viability of A549 adenocarcinoma lung cancer cells treated with CS 550 (CdTe/CdS, $\lambda_{\text{emission}} = 550$ nm), CS 659 (CdTe/CdS, $\lambda_{\text{emission}} = 659$ nm) and its corresponding CSS 0.5 ML (CdTe/CdS/ZnS, 0.5 ML ZnS) and CSS 1 ML (CdTe/CdS/ZnS, 1 ML ZnS) with a concentration range 0.002–600 $\mu\text{g ml}^{-1}$. CellTiter-Blue assay was performed with the cells incubated with NCs for 2 h (a) and 24 h (b). Half maximal inhibitory concentration (IC₅₀) values were calculated by fitted dose–response curves (presented data as mean \pm standard deviation of 4 replicates).

Therefore, *in vitro* cellular toxicity of NCs must be studied prior to *in vivo* application. In this study, *in vitro* cytotoxicity effects of developed NCs on A549 adenocarcinoma lung cancer cells was studied by treating the cells with different concentrations (0.002–600 $\mu\text{g ml}^{-1}$) of NCs composed of different sizes, shell compositions and shell thicknesses. First, cells were exposed to CS 550 and CS 659 (CdTe/CdS emitting at 550 nm and 659 nm, respectively) to investigate the NC size effect on cellular toxicity. In the next step, a ZnS shell (0.5 ML) was deposited on CS 659 NCs to evaluate the effect of outer shell composition. In the final step, a thicker ZnS shell (1.0 ML) was overgrown around CS NCs to compare the impact of ZnS shell thickness on the toxic effects of NCs. Cell viability obtained from a CellTiter-Blue assay showed that cells retained more than 70% of their viability when they were exposed to high concentrations of NCs for 2 h (**Fig. 4a**). Since $\leq 30\%$ reduction in cell viability is the

accepted limit for the biocompatibility of the tested material according to ISO 10993–5:2009 cytotoxicity standards, it can be assumed that NCs didn't generate significant toxicity after 2 h of exposure time. When the exposure time was prolonged to 24 h, high concentrations of NCs induced toxicity at different levels with a correlation to the particle size, shell composition and ZnS shell thickness (**Fig. 4b**). IC_{50} values (half-maximal inhibitory concentration, i.e. the dose applied by which 50% of cells died) demonstrate that smaller CS NCs caused more toxicity (IC_{50} 83 $\mu\text{g ml}^{-1}$) in comparison to their larger CS counterparts (IC_{50} 99.9 $\mu\text{g ml}^{-1}$). When a ZnS (0.5 ML) shell was overgrown around the CS NCs, the resulting CSS NCs exhibited significantly reduced cellular toxicity when compared to their CS NCs counterpart. As ZnS shells grew in thickness (1.0 ML), the IC_{50} value was increased further from 116.6 to 150.8 $\mu\text{g ml}^{-1}$. The main cause of cellular toxicity of Cd-containing NCs has been mostly attributed to the release of Cd^{2+} ions to the intracellular environment after particle internalization. The internalized NCs likely underwent a degradation process followed by a loss of their surface coating molecules and later the release of their metal ions *via* surface etching processes. Moreover, NCs with sizes less than 10 nm, which have high surface area to volume ratios, induce more pronounced cellular damage in comparison to larger NCs [30, 31]. In general, the toxicity decreases with increasing particle sizes [32]. Regarding the size-dependent cytotoxicity of NCs, we confirmed the pronounced toxicity of smaller NCs in comparison to larger ones with the same core/shell composition as well as similar surface structure. On the other hand, the presence of a well-passivating protective ZnS shell layer can likely minimize the destabilization of NCs to a large extent and therefore prevent the release of highly toxic metal ions [23, 33]. The obtained cell viability results of CSS NCs meet the expectations of the inert nature of ZnS, building a strong electronic barrier at the NCs surface and therefore resulting in reduced cytotoxic effects.

Cell imaging with aptamer conjugated NCs

CdTe/CdS/ZnS NCs modified with aptamers were tested for their targeted *in vitro* cell imaging applicability. We first conjugated the carboxyl terminated CdTe/CdS/ZnS NCs to amine-terminated S15 DNA aptamers which target adenocarcinoma lung cancer cells (dissociation constant, K_d 56.8 nM) [10] using EDC coupling chemistry (S15–NCs). As a negative control, bare NCs and NCs conjugated with a random oligonucleotide (Oligo–NCs) were applied to the A549 cells using the same experimental conditions.

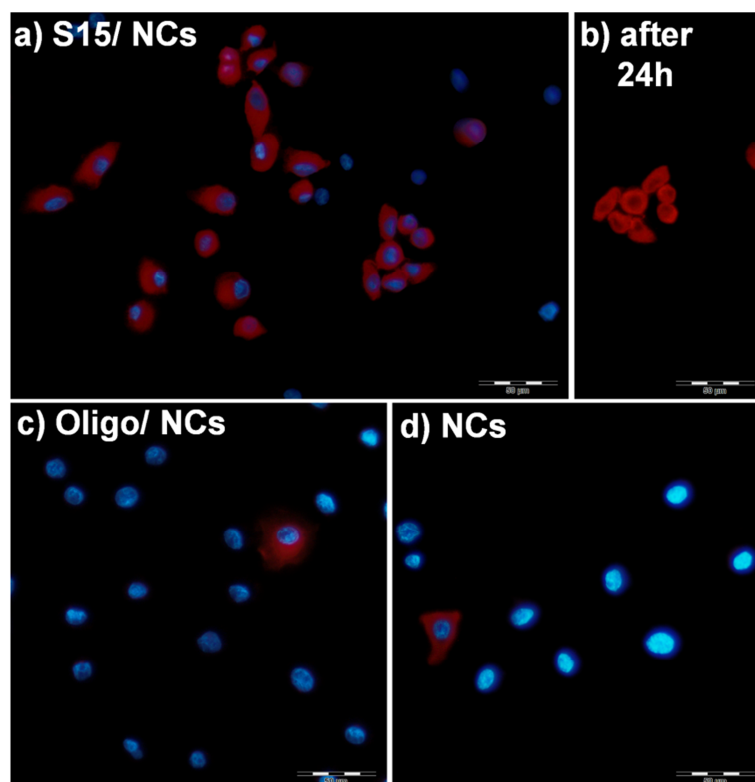


Fig. 5 Fluorescence microscope images of A549 adenocarcinoma lung cancer cells treated with S15 aptamer–NCs conjugates (a), Oligo–NCs (c), and bare NCs (d) for 2 h. Images of cells treated with S15–NCs after 24 h of internalization (b). Cell nuclei were counterstained with DAPI. Scale bar 50 µm.

Migration behaviors of NC conjugates were analyzed with agarose gel electrophoresis (**Fig. S5†**). As predicted, NCs conjugated to aptamer or oligonucleotide migrated slower in comparison to bare NCs. However S15–NCs and Oligo–NCs exhibited similar migration pattern despite of different molecular weights. We attribute this effect to the reduced sizes of oligonucleotides in their three-dimensional structures which are rather indistinguishable in terms of their electrophoretic mobility.

Fluorescence microscopy images illustrated in **Fig. 5**, reveal the internalization of S15–NCs in the lung cancer cells within 2 h of incubation (**Fig. 5a**). At the same time, Oligo–NCs as well as bare NCs did not accumulate in the cells within the given incubation time (**Fig. 5c** and **d**). Promisingly, aptamer–NC conjugates were still observable under the microscope after 24 h of internalization, indicating the long-term stability of developed NCs inside the cells (**Fig. 5b**). Accordingly, we can draw the conclusion that S15 DNA aptamers are efficient as a targeting moiety against lung cancer cells and in combination with the excellent optical properties of the NCs, present a novel platform for the application of developed NCs for targeted cell imaging studies.

4.1.5. Experimental

Materials

CdCl₂ · 2^{1/2} H₂O (cadmium chloride (pentahydrate), 98%>), Na₂TeO₃ (sodium tellurite, 99.5%), ZnCl₂ (zinc chloride, anhydrous, 99.99%), 3-mercaptopropionic acid (MPA, 99%), NaBH₄ (sodium borohydride, >98.0%), trisodium citrate dehydrate, *N*-(3-dimethylaminopropyl)-*N'*-ethylcarbodiimide hydrochloride (EDC), boric acid and rhodamine 6G (dye content ~95%) were purchased from Sigma-Aldrich GmbH, Munich. Qdot® 655 ITK™ carboxyl quantum dots (QY 87%) were obtained from Life Technologies GmbH, Darmstadt. CellTiter-Blue cell viability assay reagent was purchased from Promega GmbH, Mannheim. S15-amino(C6) aptamer and control DNA-amino(C6) were purchased from BioSpring GmbH, Frankfurt. All chemicals were used as they were received without any purification. All solutions were prepared with distilled water if not indicated otherwise.

Sequence of 5'-amino(C6)-S15 DNA aptamer.

5'ACGCTCGGATGCCACTACAGGCTATCTTATGGAAATTTTCGTGTAGGGTTTGTGTGGCGGGGCTACTCATGGACGTGCTGGTGAC3' [10]

Sequence of random 5'-amino(C6)-oligonucleotide.

5'ATACGGGAGCCAACACCAGCAGTCAAGAAGTTAAGAGAAAAACAATTGTGTATAAGAGCAGGTGTGACGGAT3'

For cell culture experiments, Dulbecco's Modified Eagle Medium (DMEM, Sigma-Aldrich GmbH, Munich) supplemented with 10% (v/v) fetal calf serum (FCS, Biochrom GmbH, Germany) and 1% (v/v) penicillin/streptomycin (P/S, Biochrom GmbH, Germany) was used as cell culture medium. For fluorescence imaging experiments, cells were seeded on LabTek® II glass chamber slide systems with CC2 treatment (Nalge Nunc International, USA).

Buffers

Aptamer selection buffer (pH 7.4) was prepared with 2.67 mM calcium chloride, 1.47 mM calcium dihydrogen phosphate, 137.93 mM sodium chloride, 8.06 mM disodium hydrogen phosphate, 5 mM magnesium chloride, 4.5 g L⁻¹ glucose and 1 mg ml⁻¹ bovine serum albumin (Sigma-Aldrich GmbH, Munich). Incubation buffer was prepared from the selection buffer by addition of 2% (v/v) FCS. Phosphate buffered

saline (PBS) was prepared with 137 mM sodium chloride, 2.7 mM calcium chloride, 10.1 mM disodium hydrogen phosphate and 1.8 mM calcium dihydrogen phosphate. Solution pH was adjusted to 7.4 and then sterilized.

Synthesis of CdTe/CdS

CdCl₂ (125 mM, 1 ml), 18.5 µl 3-mercaptopropionic acid (MPA), trisodium citrate dehydrate (42.5 mM, 1 ml), sodium tellurite (5 mM, 1 ml) and sodium borohydride (125 mM, 1 ml) were added sequentially into a three-neck round bottom flask. 21 ml ddH₂O was added to give a final volume of 25 ml. The molar ratio of Cd/Te/MPA was set to be 1/0.04/1.7. Under mixing, the solution pH was adjusted to 11.4 with 1 M NaOH. Reaction solution was then heated to 90 °C at a heating rate of approximately 3.5 °C min⁻¹. The solution was then refluxed with an air condenser (Findenser, Radleys, UK) eliminating the necessity of any tubing systems for water cooling making the procedure simpler and more economic. Once the reaction solution reached a temperature of 90 °C, the samples were collected at different time intervals during 6 h. Absorbance and fluorescence measurements were made with crude samples after cooling to room temperature. For storage, samples were precipitated with 2-propanol and collected via centrifugation. The precipitate was weighted after it was dried. Later, it was re-dissolved in water and stored at 4 °C.

Deposition of ZnS shell

The as-prepared CdTe/CdS solution ($\lambda_{\text{emission}} = 650\text{--}660$ nm, QY~ 57%) was directly used for the external synthesis of ZnS. 12 ml of the CdTe/CdS crude solution, 12 ml ddH₂O and 1 ml ZnCl₂ solution (25 mM) was stirred giving a final volume of 25 ml. The final pH of the reaction solution was adjusted to 11.5 with 1 M NaOH. Then, the solution was heated slowly to 65 °C and the ZnS shell growth was monitored for 6 h. Apart from dilution, no post-synthesis treatment was made for any of the samples before absorbance and fluorescence measurements. For cell culture experiments, samples were precipitated with 2-propanol and collected via centrifugation. The colloidal precipitate was weighed after drying and re-dissolved in water. Later, this was washed with ddH₂O using 10 kDa MWCO membrane filters (PES, Vivaspin, Sartorius Stedim Biotech GmbH, Germany) and stored at 4 °C.

Measurement of QY%

Fluorescence quantum yields (QY%) were determined by using commercially available Qdot® 655 ITK™ carboxyl quantum dots (QY 87%) as a reference. Rhodamine 6G was used first as a cross-reference to confirm the QY% of the commercial Qdot655 and it was found to be $86.7 \pm 0.5\%$ which is consistent with the QY value given by the manufacturer. Then, the as-prepared colloidal samples as well as the reference solution were diluted to give an equal absorbance below 0.1 at the excitation wavelength (470 nm). The integrated area of corresponding emission curves were analyzed and compared with the integrated area of emission curve of reference Qdot655 sample in the same solvent (eqn (1)).

$$\text{QY \%}_{(\text{sample})} = \text{QY \%}_{(\text{reference})} \frac{\text{Area}_{(\text{sample})} / \text{Area}_{(\text{reference})}}{\text{Abs}_{(\text{reference})} / \text{Abs}_{(\text{sample})}} \quad (1)$$

Photostability study

To exclude the effect of residual reagents, purified CdTe/CdS and CdTe/CdS/ZnS samples were tested for their photostability. 1 ml of diluted samples were irradiated with UV light (360 nm) continuously for 5 h by using 150 W xenon lamp. The corresponding fluorescence intensity was recorded every 10 s.

Structural analysis

X-ray diffraction patterns of CdTe/CdS NCs and corresponding CdTe/CdS/ZnS NCs were analyzed with a Bruker D8 Advance diffractometer using Cu K α radiation ($\lambda = 1.5418 \text{ \AA}$). For the measurements, samples were precipitated with 2-propanol after synthesis and dried under vacuum to yield powdered samples, which were deposited on a single-crystal Si wafer. Transmission electron microscopy (TEM) and high-resolution transmission electron microscopy (HRTEM) measurements were conducted with FEI Tecnai T20 (FEI, USA) and FEI Tecnai G2 F20 TMP-TEM with a 200 kV FEG (field emission gun) in bright field mode, respectively. Samples were prepared from solution by placing a droplet on a carbon coated mesh copper grid and drying in air. Topographic images of CdTe/CdS/ZnS NCs were taken with Nanowizard II atomic force microscope (AFM) from JPK-Instruments AG (Berlin, Germany). Images of

2 μm –2 μm size were collected at a 0.5 Hz scan rate and 1024 x 1024 pixel resolutions. In order to reach high resolution, a very sharp AFM cantilever of MSNL (nominal tip radius approx. 2 nm, nominal force constant 0.6 N m⁻¹) from Bruker Corporation (CA, USA) was used. A drop of 50 ml of diluted NCs suspension was placed onto a clean polysine microscope adhesion slide (Thermo Fisher Scientific Inc. USA) and was allowed to dry at room temperature. The glass slide was then mounted onto an inverted light microscope (AxioObserver D1, Zeiss AG, Jena, Germany). Thereafter, the AFM was placed on the light microscope and imaging was employed in air using contact mode. Fluorescence decay curves were collected by a HPM 100–40 detector (Becker&Hickl GmbH, Germany), and time-correlated single photon-counting (TCSPC) was achieved by a SPC-150 module (Becker&Hickl GmbH, Germany). 10 μL of the NC suspension was placed on the stage of a Leica TC SP2 inverted scanning confocal microscope with a water 1.2NA 63x objective. The sample was excited by a picosecond pulsed diode laser (Hamamatsu Photonics, Japan) at 467 nm with a repetition rate of 1 MHz.

Cytotoxicity study

For the cytotoxicity studies, human lung adenocarcinoma A549 cells (ACC107) purchased from DSMZ (German Collection of Microorganism and Cell Cultures) were used with a passage number of less than 20. CellTiter-Blue (CTB) cell viability assay was performed for an indirect estimation of the numbers of viable cells to evaluate the cytotoxicity of CdTe/CdS and CdTe/CdS/ZnS NCs. It uses the indicator dye resazurin which is reduced by viable cells into highly fluorescent resorufin (579_{Ex}/584_{Em}). The procedure was performed as follows: A549 cells (8000 cells per well) in culture medium (DMEM supplemented with 10% FCS and 1% P/S) were cultured in 96-well plates (100 μl per well) and incubated for 2 days at 37 °C, 5% CO₂, >90% humidity. NC dilution series were prepared with cell culture medium, and 100 μl of NC solutions were added to each well. A549 cells were treated with NCs for 2 h and 24 h. After incubation, cells were washed gently with PBS buffer 2 times. CTB reagent was diluted 1 : 6 with DMEM medium (without supplement), and 100 μl of mixture was added to each well and incubated for 2 h (37°C, 5% CO₂). Finally, the resulting fluorescence intensities were recorded, and cell viability was calculated using the fluorescence intensity of untreated cells as a reference. Dose-dependent response curves were evaluated by fitting the concentration-dependent experimental cell viability data with

dose–response non-linear fitting function (Origin Pro 8.5, Origin Lab Corp. USA). Half-maximal inhibitory concentrations (IC_{50}) were calculated from the fitted dose–response curves.

Conjugation with aptamer

CdTe/CdS/ZnS NCs ($\lambda_{\text{emission}} = 668\text{--}670\text{ nm}$) were labeled with S15-Amino aptamers for targeting of A549 lung adenocarcinoma cells through EDC coupling reaction between carboxyl groups of NCs and amino groups of aptamer molecules. S15-Amino aptamer (177 μM , 16 μl) solution was added to CdTe/CdS/ZnS (9 mg ml^{-1} , 24.4 μl) solution dissolved in sodium borate buffer (10 mM , pH 7.4) to give a final volume of 100 μl , and mixed for 5 min at room temperature. Then, 10 mg ml^{-1} EDC solution (6.5 μl) dissolved in sodium borate buffer (10 mM , pH 7.4) was added to the mixture and incubated for 3 h at room temperature. After coupling, S15–NCs conjugates were purified with centrifugation through membrane filters (50 kDa MWCO PES, Vivaspin, Sartorius Stedim Biotech GmbH, Germany). The purification step was repeated 8–9 times with 50 mM sodium borate buffer (pH 8.3). As a negative control, CdTe/CdS/ZnS NCs were conjugated with a random oligonucleotide (Oligo–NCs) using the same procedure. 20 μl of NCs conjugates were applied to agarose gel electrophoresis. 1.5% agarose gel was run at 100 V for 10 min and then viewed with a gel imaging system equipped with an UV transilluminator (INTAS Science Imaging Instruments GmbH, Germany) after 0.40 seconds of exposure time.

Cell imaging

A549 cells were treated with unconjugated and aptamer–conjugated CdTe/CdS/ZnS NCs. NC conjugates were first transferred to binding buffer prior to treatment. A549 cells in cell culture medium were seeded on glass chamber slides (Nunc LabTek-II with CC2 treatment) and allowed to grow for 2 days at 37 °C, 5% CO_2 . After cell culture medium was removed, cells were treated for 15 min with incubation buffer (selection buffer with 2% FCS). Incubation buffer was then removed and cells were treated with 200 μl of bare NCs (0.125 mg ml^{-1}), S15–NC (0.125 mg ml^{-1}) and Oligo–NC conjugate solutions (0.125 mg ml^{-1}) which were diluted in incubation buffer. A549 cells were then incubated with the conjugates for 2 h. After that, incubation buffer was removed and cells were washed gently with warm PBS solution 2 times. For the imaging experiments, a fluorescence microscope (Olympus Ix50) equipped with an

Olympus camera (SC30, Japan) was used to capture the images of cells with CellSens Standard (Olympus Co. Japan) software (Excitation filter: BP530–550, barrier filter: BA590).

4.1.6. Conclusions

We demonstrated a simple one-pot aqueous synthesis approach to generate red-emitting CdTe/CdS/ZnS CSS nanocrystals. Strain-induced optical properties of type-II CdTe/CdS NCs with a very small core and a very thick shell were further improved with the external growth of a wide bandgap ZnS shell material. The band offsets between CdS and ZnS allowed efficient exciton confinement in the type-II core/shell and, therefore led to increased fluorescence efficiencies (QY_{\max} 64%) and stability. Moreover, cytotoxicity studies proved the reducing effect of an outer ZnS shell by minimizing the destabilization of the NCs. Also, preliminary cell imaging experiments with aptamer–conjugated NCs exhibited effective cell internalization. Remarkably, the aptamer–NC conjugates were stable inside the cells even after 1 day of internalization. In conclusion, the developed CdTe/CdS/ZnS NCs exhibit very high optical efficiencies, stability, as well as reduced toxicity representing an ideal candidate as a fluorescent probe for bio-imaging applications.

4.1.7. Acknowledgements

M. Ulusoy would like to acknowledge the German Academic Exchange Service (DAAD) for financial support. Also, we thank Martin Paehler for technical assistance at agarose gel electrophoresis study and Dr Fritz Schulze Wischeler from Laboratory of Nano and Quantum Engineering (LNQE) for his support for HRTEM analysis.

4.1.8. Notes and references

1. A. M. Smith, A. M. Mohs and S. Nie, *Nat. Nanotechnol.*, 2009, **4**, 56–63.
2. Z. T. Deng, O. Schulz, S. Lin, B. Q. Ding, X. W. Liu, X. X. Wei, R. Ros, H. Yan and Y. Liu, *J. Am. Chem. Soc.*, 2010, **132**, 5592–5593.
3. L. N. Chen, J. Wang, W. T. Li and H. Y. Han, *Chem. Commun.*, 2012, **48**, 4971–4973.
4. P. Reiss, M. Protiere and L. Li, *Small*, 2009, **5**, 154–168.
5. S. Tamang, G. Beaune, I. Texier and P. Reiss, *ACS Nano*, 2011, **5**, 9392–9402.
6. R. G. Xie, M. Rutherford and X. G. Peng, *J. Am. Chem. Soc.*, 2009, **131**, 5691–5697.

7. F. Todescato, A. Minotto, R. Signorini, J. J. Jasieniak and R. Bozio, *ACS Nano*, 2013, **7**, 6649–6657.
8. M. Green, P. Williamson, M. Samalova, J. J. Davis, S. Brovelli, P. Dobson and F. Cacialli, *J. Mater. Chem.*, 2009, **19**, 8341–8346.
9. L. L. Li, Y. Chen, Q. Lu, J. Ji, Y. Y. Shen, M. Xu, R. Fei, G. H. Yang, K. Zhang, J. R. Zhang and J. J. Zhu, *Sci. Rep.*, 2013, **3**, 1529.
10. Z. L. Zhao, L. Xu, X. L. Shi, W. H. Tan, X. H. Fang and D. H. Shangguan, *Analyst*, 2009, **134**, 1808–1814.
11. M. Meyer, T. Scheper and J. G. Walter, *Appl. Microbiol. Biotechnol.*, 2013, **97**, 7097–7109.
12. D. V. Talapin, A. L. Rogach, E. V. Shevchenko, A. Kornowski, M. Haase and H. Weller, *J. Am. Chem. Soc.*, 2002, **124**, 5782–5790.
13. M. Lonne, G. H. Zhu, F. Stahl and J. G. Walter, *Biosensors Based on Aptamers and Enzymes*, 2014, **140**, 121–154.
14. J. G. Walter, S. Petersen, F. Stahl, T. Scheper and S. Barcikowski, *J. Nanobiotechnol.*, 2010, **8**, 21.
15. M. Lubbecke, J. G. Walter, F. Stahl and T. Scheper, *Eng. Life Sci.*, 2012, **12**, 144–151.
16. V. Bagalkot, L. Zhang, E. Levy-Nissenbaum, S. Jon, P. W. Kantoff, R. Langer and O. C. Farokhzad, *Nano Lett.*, 2007, **7**, 3065–3070.
17. D. Kim, Y. Y. Jeong and S. Jon, *ACS Nano*, 2010, **4**, 3689–3696.
18. W. J. Kang, J. R. Chae, Y. L. Cho, J. D. Lee and S. Kim, *Small*, 2009, **5**, 2519–2522.
19. H. Shi, X. S. Ye, X. X. He, K. M. Wang, W. S. Cui, D. G. He, D. Li and X. K. Jia, *Nanoscale*, 2014, **6**, 8754–8761.
20. E. V. Shevchenko, D. V. Talapin, H. Schnablegger, A. Kornowski, O. Festin, P. Svedlindh, M. Haase and H. Weller, *J. Am. Chem. Soc.*, 2003, **125**, 9090–9101.
21. V. Lesnyak, N. Gaponik and A. Eychmuller, *Chem. Soc. Rev.*, 2013, **42**, 2905–2929.
22. L. Zou, Z. Y. Gu, N. Zhang, Y. L. Zhang, Z. Fang, W. H. Zhu and X. H. Zhong, *J. Mater. Chem.*, 2008, **18**, 2807–2815.
23. Y. He, H. T. Lu, L. M. Sai, Y. Y. Su, M. Hu, C. H. Fan, W. Huang and L. H. Wang, *Adv. Mater.*, 2008, **20**, 3416–3421.
24. J. N. Tian, R. J. Liu, Y. C. Zhao, Y. Peng, X. Hong, Q. Xu and S. L. Zhao, *Nanotechnology*, 2010, **21**, 305101–305108.
25. Z. Li, C. Q. Dong, L. C. Tang, X. Zhu, H. J. Chen and J. C. Ren, *Luminescence*, 2011, **26**, 439–448.
26. S. Taniguchi, M. Green, S. B. Rizvi and A. Seifalian, *J. Mater. Chem.*, 2011, **21**, 2877–2882.
27. Y. Y. Zhang, J. Y. Kim, Y. Kim and D. J. Jang, *J. Nanopart. Res.*, 2012, **14**, 1117–1125.
28. W. Jiang, A. Singhal, J. N. Zheng, C. Wang and W. C. W. Chan, *Chem. Mater.*, 2006, **18**, 4845–4854.
29. M. Bottrill and M. Green, *Chem. Commun.*, 2011, **47**, 7039–7050.
30. S. J. Soenen, P. Rivera-Gil, J. M. Montenegro, W. J. Parak, S. C. De Smedt and K. Braeckmans, *Nano Today*, 2011, **6**, 446–465.
31. P. Rivera-Gil, D. J. De Aberasturi, V. Wulf, B. Pelaz, P. Del Pino, Y. Y. Zhao, J. M. De La Fuente, I. R. De Larramendi, T. Rojo, X. J. Liang and W. J. Parak, *Acc. Chem. Res.*, 2013, **46**, 743–749.
32. A. Nel, T. Xia, L. Madler and N. Li, *Science*, 2006, **311**, 622–627.
33. G. X. Liang, L. L. Li, H. Y. Liu, J. R. Zhang, C. Burda and J. J. Zhu, *Chem. Commun.*, 2010, **46**, 2974–2976.

4.1.9. Supplementary Information

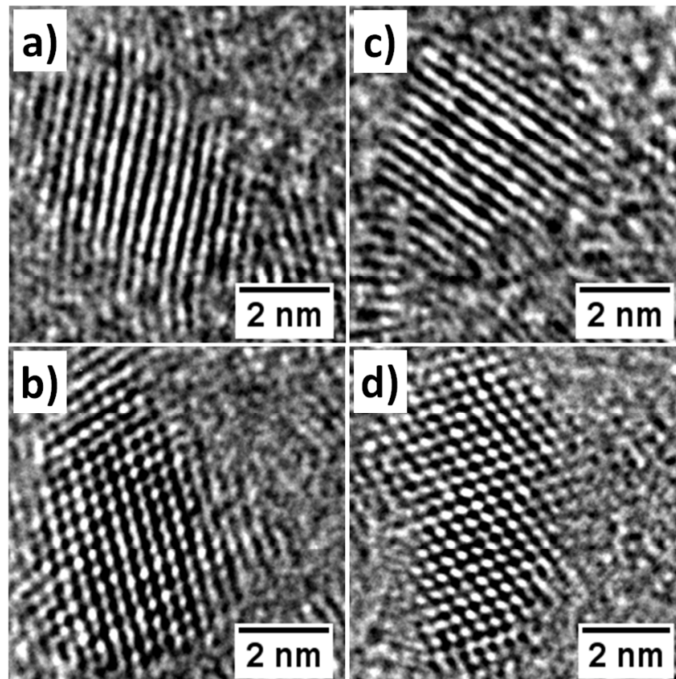


Fig. S1 HRTEM images of CdTe/CdS/ZnS NCs with high magnifications showing different tetrahedral shapes.

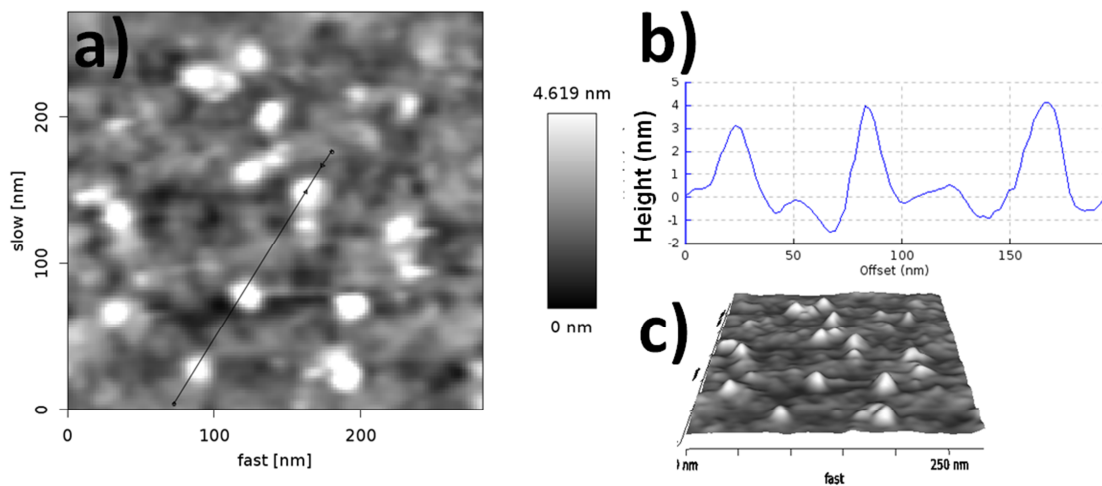


Fig. S2 Atomic force microscopy (AFM) images of CdTe/CdS/ZnS nanocrystals deposited on poly lysine coated glass slides (a), the height profile of the cross-section marked with black straight line (b), 3-D surface plot of AFM image in (c).

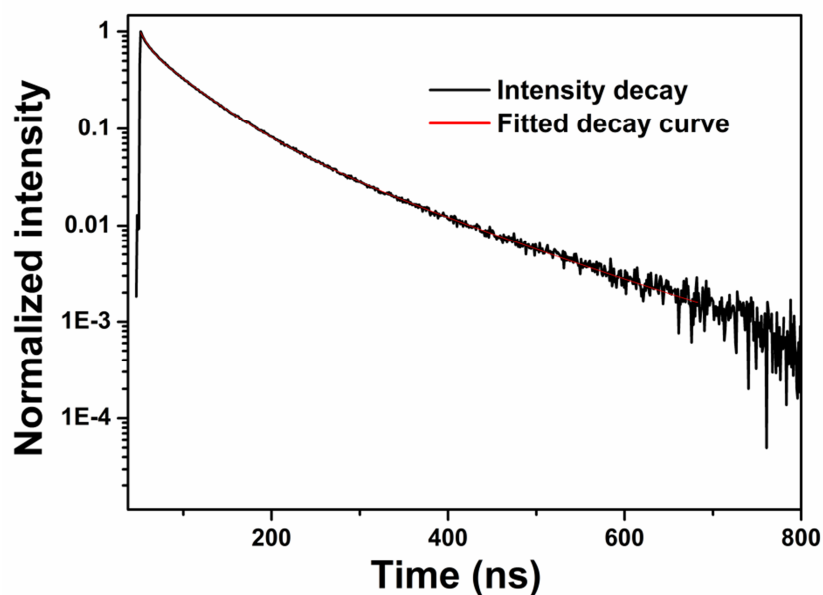


Fig. S3 Fluorescence lifetime decay profile of CdTe/CdS/ZnS NCs ($\lambda_{\text{emission}}=683$ nm). Sample was excited at 467 nm with a repetition rate of 1MHz. Sample was scanned for 30 seconds to constitute a single decay. This operation was repeated 5 times. An average decay was computed from all repeats for subsequent fitting (red line).

Table S1. Fluorescence lifetime characteristics of CdTe/CdS/ZnS NCs ($\lambda_{\text{emission}}=683$ nm)

A1 (%)	τ_1 (ns)	A2 (%)	τ_2 (ns)	A3 (%)	τ_3 (ns)	τ_{av} (ns) *
25.2 ± 0.6	9.0 ± 0.3	57.6 ± 0.5	50.7 ± 0.8	15.1 ± 0.8	134 ± 3	51.7

*Fit parameter derived using the tri-exponential fitting function:

$$I(t) = y_0 + A_1 e^{-\frac{t}{\tau_1}} + A_2 e^{-\frac{t}{\tau_2}} + A_3 e^{-\frac{t}{\tau_3}}$$

Where τ_1 , τ_2 and τ_3 are the decay constants and A_1 , A_2 , A_3 their relative amplitudes, y_0 is the offset and approaches zero in appropriately background-corrected data. The intensity-weighted average lifetime was calculated according to:

$$\tau_{\text{av}} = (A_1 \tau_1^2 + A_2 \tau_2^2 + A_3 \tau_3^2) / (A_1 \tau_1 + A_2 \tau_2 + A_3 \tau_3)$$

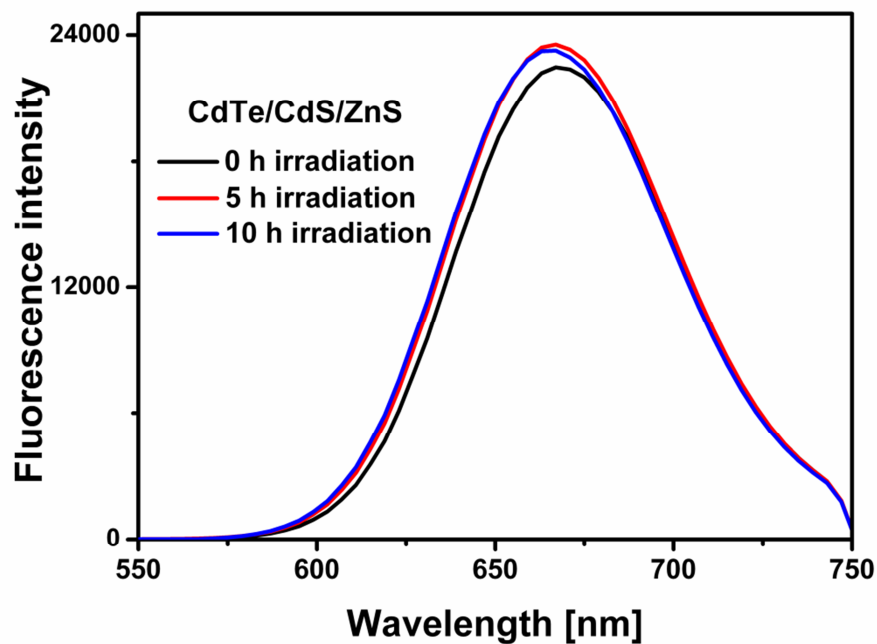


Fig. S4 Fluorescence emission spectra of CdTe/CdS/ZnS NCs before and after irradiation under UV light at 360 nm for 5 h and 10 h. Fluorescence intensity was recorded every 10 s.

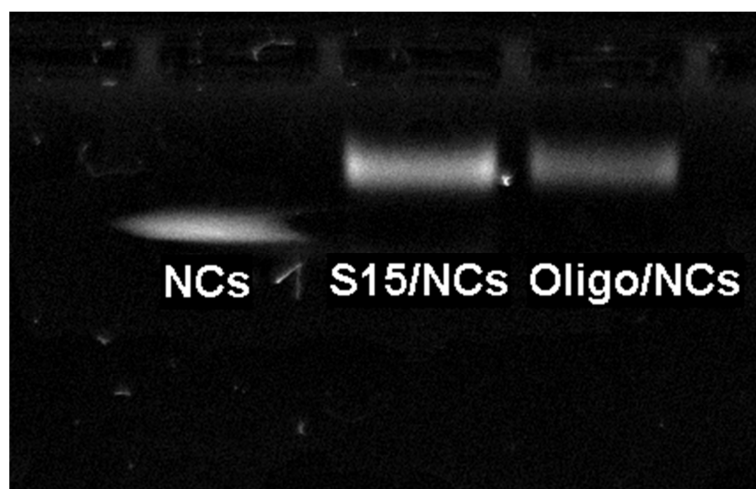
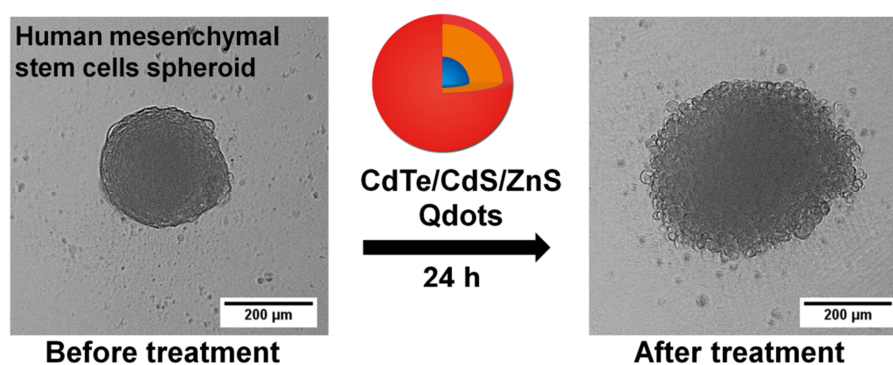


Fig. S5 Digital image of agarose gel electrophoresis for CdTe/CdS/ZnS NCs, S15 aptamer conjugated NCs (S15/NCs) and oligonucleotide conjugated NCs (oligo/NCs) (exposure time: 0.4 s)

4.2. Application of Qdots to 3D spheroid cultures

The results of this chapter were published as Ulusoy *et al.*, Evaluation of CdTe/CdS/ZnS core/shell/shell quantum dot toxicity on three-dimensional spheroid cultures, *Toxicological Research*, 2015, 5, 126-135. It was reproduced by permission of The Royal Society of Chemistry.

Table of Contents Graphic



Three-dimensional hAD-MSCs spheroid cultures, with the ability to resemble closely *in vivo* tissue structures, were assessed for evaluation of dose-dependent cytotoxicity effects of CdTe/CdS/ZnS quantum dots.

4.2.1. Summary

After the establishment of the aqueous synthesis of carboxyl-functionalized CdTe/CdS/ZnS core_(small)/shell_(thick)/shell_(small) Qdots with high quantum yields (QY%) up to ~ 64% and great stability against photobleaching in the previous chapter, herein *in vitro* cytotoxicity of as-prepared Qdots, and their labelling efficiency in three-dimensional (3D) spheroid cultures were investigated in detail. 3D cell culture models hold potential to mimic tissue-like morphology through well developed cell-cell and cell-extracellular matrix (ECM) interactions and distinct diffusion/transport characteristics. Among them, spheroid structures are the most widely used model for high-throughput screening assays since they don't require an external scaffold for the aggregation of the cells.

In this report, 3D spheroid cultures of human adipose-derived mesenchymal stem cells (hAD-MSCs) were utilized to assess dose-dependent adverse effects of carboxyl-

functionalized Qdots. hAD-MSCs were used as model cells since they were found to be more susceptible to Qdot toxicity (IC_{50} 40 $\mu\text{g ml}^{-1}$) in comparison to A549 lung adenocarcinoma cell lines (IC_{50} 150 $\mu\text{g ml}^{-1}$) according to the previous investigations. Moreover, they are considered to be a promising candidate for cell therapy studies. The effects of Qdots on 3D spheroids were first assessed by examining the morphology of spheroids upon Qdot incubation. For that time-lapse microscopy as well as end-point microscope analyses were conducted to monitor morphological alterations. In the next step, metabolic activity of spheroid cultures was determined with two different cell viability assays; CellTiter-Blue (CTB) and adenosine triphosphate (ATP) assays. The obtained results were later compared with 2D monolayer cultures.

As a result, 3D spheroid cultures were found to be more resistant to Qdot-induced cytotoxicity in comparison to 2D monolayer cultures. When cells were exposed to different levels of Qdots at the beginning of spheroid formation, Qdots at high concentrations ($\geq 600 \mu\text{g ml}^{-1}$) impaired cell-cell and cell-ECM interactions, and impeded aggregation of cells to form spheroids. When cells were incubated with Qdots after spheroid formation, effects of Qdots became mild. Only at high Qdot doses ($\geq 600 \mu\text{g ml}^{-1}$), spheroid surfaces became rough and formation of rounded cells was pronounced. It indicates significant increase in cell death. The granule cells did not detach from the spheroid surface, therefore overall spherical structure was preserved. Moreover, the diameter of the spheroid increased by 48% due to protruding of granular shaped cells. Metabolic activity results obtained from ATP assay revealed significant differences between 2D and 3D spheroid cultures that were treated with Qdots. Interestingly, dose-response curves for 2D culture featured a reproducible biphasic model, whereas for 3D cultures a monotonic dose-response pattern was observed. The obtained results suggest the presence of two distinct cell populations in 2D cultures with different sensitivity to Qdots, although that effect wasn't observed in 3D spheroids. Meanwhile, CTB assay was found to be an unreliable viability assay for 3D cultures due to diffusion limitations for assay metabolites (resazurin/resorufin) in such densely packed stem cell spheroids. In the final step, Qdots were tested for their ability to label spheroid structures by using fluorescence and confocal microscopy studies. Accordingly, carboxyl-functionalized Qdots were readily internalized into the cells in the spheroid structure instead of being non-specifically captured by extracellular matrix material. According to the z-stacked confocal microscopy images, Qdot showed

maximum labelling at peripheral regions of the spheroids, and fluorescence signals of Qdots decreased towards the inner region of the spheroids. These observations suggest the presence of diffusion limitation for the transport of Qdots into spheroid inner region for the given incubation time.

In conclusion, 3D spheroid cultures were found to be more resistant to Qdot-induced toxicity than 2D monolayer cultures. The results of this study will help to predict *in vivo* toxicity of Qdots and provide essential screening steps prior to any biological application. Moreover, penetration ability of highly fluorescent Qdots to densely-packed stem cells spheroids showed the versatility of Qdots in 3D spheroid imaging.

4.2.2. Abstract

In this work, three-dimensional (3D) spheroid cultures of human adipose-derived mesenchymal stem cells (hAD-MSCs), with tissue-mimetic morphology through well developed cell–cell and cell–matrix interactions and distinct diffusion/transport characteristics, were assessed for dose-dependent toxic effects of red-emitting CdTe/CdS/ZnS quantum dots (Qdots). Morphological investigations and time resolved microscopy analysis in addition to cell metabolic activity studies revealed that 3D spheroid cultures are more resistant to Qdot-induced cytotoxicity in comparison to conventional 2D cultures. The obtained results suggest the presence of two distinct cell populations in 2D cultures with different sensitivity to Qdots, however that effect wasn't observed in 3D spheroids. Our investigations were aimed to improve the prediction of nanotoxicity of Qdot on tissue-level and provide the essential screening steps prior to any *in vivo* application. Moreover, penetration ability of highly fluorescent Qdots to densely packed spheroids will fortify the biological application of developed Qdots in tissue-like structures.

4.2.3. Introduction

Conventional two-dimensional (2D) cell culture where a cell monolayer grows on flat plastic or glass surfaces does not reflect the essential physiology of real tissues. Since cells in the body grow in a three-dimensional (3D) environment, a 3D approach as an alternative to 2D culture can reduce the gap between cell culture and living tissue. Therefore, a 3D culture exhibits significant potential to improve the physiological

relevance of cell-based assays [1–4]. In many studies, 3D cell cultures were proven to display the induced extracellular matrix (ECM)-related biological functions such as intercellular signaling and interactions, cellular function and maintenance, molecular transport and tissue morphology [5–7]. Cellular spheroids, being a simplified model of 3D cell cultures, take advantages of natural tendency of cells to aggregate [8]. The cells produce ECM which in turn enhances intercellular adhesion. Thus, they don't require an external scaffold for the aggregation of the cells. For that reason, it is the most widely used model for high-throughput screening of straightforward cell function and toxicity analysis for biomedical applications [6, 9, 10]. For nanoparticle (NP)-based cytotoxicity, labeling and delivery studies, 3D spheroid models have advantages over monolayer cell cultures [3]. Monolayer cell cultures produce less dense ECM material on an apical side whereas cells grown in 3D extend ECM matrix production to all dimensions. Therefore, 2D models present a less significant barrier for transport and reduced cell binding compared to cells in 3D environment [11]. For that reason, results obtained from NP-based research on 2D cell cultures do not reflect similar results as obtained from 3D cultures.

3D models, however, possess some limitations in terms of translation compared to available 2D-based analysis methods. Some cell-based high-throughput screening methods for rapid analysis of drug or NP-based cellular responses (such as dose-dependent cell viability, cell migration and cell–cell/cell–matrix interaction) haven't been optimized for 3D culture models yet. Remaining limitations to overcome are scalability, reproducibility, sensitivity and compatibility of analytical methods with available screening systems. Despite the increasing number of publications for 3D-based cell culture studies, optimization of available analytical methods in order to address the nanoparticle and drug interactions remains a challenge [12].

Nanocrystals of semiconductors, so-called quantum dots (Qdots), represent one of the most diverse NP class owing to a wide range of optical and structural properties which allow numerous application areas from molecular imaging to targeted drug delivery [13–15]. Based on their size-tunable optical features, narrow emission and broad absorption bands in combination with broad-band excitations and long fluorescence life time, Qdots take a special position when compared with other nanoparticles and organic fluorophores [16, 17]. However, vast application of Qdots in cellular uptake studies come with some concerns, of which their toxicity comprises one of the major points of issue. Their fate in the organism as well as their toxicity which has a direct

relation to their structure, size, surface chemistry and colloidal stability became an important research topic for their engineering and development. For that reason, investigation of any Qdot-related side effects on the cell level must be accomplished prior to their bioapplication. Until now, for almost all studies on Qdot toxicity, 2D cell cultures were used for the determination of dose-dependent adverse effects, and the results of the studies are difficult to translate to *in vivo* models. Regarding Qdot-related toxicity, to best of our knowledge, there is only one study by Lee and coworkers where effect of single dose CdTe Qdots on HepG2 spheroid cultures was reported [18]. However, applied Qdot doses comprise one of the major parameters in toxicity studies; hence, dose-dependent adverse effects must be investigated in details in order to understand the Qdot interactions in a better way. Therefore, exploration of dose-dependent Qdot effects on 3D spheroid models should be considered as an essential step for the prediction of Qdot toxicity on micro-tissue structures.

In this report, we describe the evaluation of dose-dependent adverse effects of carboxyl-functionalized CdTe/CdS/ZnS core_(small)/shell_(thick)/shell_(small) (CSS) Qdots on 3D spheroid cultures. One-pot aqueous synthesis of near-infrared emitting CdTe/CdS/ZnS core_(small)/shell_(thick)/shell_(small) CSS Qdots with high quantum yields (~64%) and impressive stability against photobleaching was recently reported in our previous study [19]. The developed CSS Qdots hold a great potential for cellular imaging studies to owing near-infrared emission, which will give them an advantage to be monitored in thick and highly scattering 3D tissue samples [20]. As a model system, we utilized human adipose-derived mesenchymal stem cells (hAD-MSCs) spheroid cultures as they are considered to be a promising candidate for cell therapy [21]. Stem cells were also found to be more susceptible to Qdot toxicity (IC₅₀ 40 µg ml⁻¹) in comparison to A549 lung adenocarcinoma cell lines (IC₅₀ 150 µg ml⁻¹) according to our previous study [19]. For that reason, hAD-MSCs were chosen as a suitable candidate to investigate Qdot-induced cytotoxicity. The adverse effects of Qdots were examined using two different approaches, including morphology and metabolic activity. Dose-dependent cell viability was determined with two different cell viability assays; CellTiter-Blue (CTB) and adenosine triphosphate (ATP) assays, and results were compared with monolayer 2D cultures. Morphological observations as well as metabolic activity studies were discussed in details. In the later step, the ability of Qdots to label spheroid structures was tested via fluorescence and confocal microscopy studies. Our results highlighted significant physiologically relevant data for Qdot-

induced toxicity. We believe that outcomes of this study will provide important data to increase our understanding of Qdots-induced toxicity on tissue levels. They can also contribute to the establishment of analytical methods for nanoparticle-based cytotoxicity studies in tissue-like *in vitro* systems. Additionally, the penetration ability of Qdots to densely packed stem cell spheroids in combination with their high fluorescence yield with near-infrared emission feature will greatly aid future exploration of Qdots for the targeted imaging studies in 3D models, and potentially will broaden up their range of applications to the delivery of therapeutic agents to 3D compact tumors for diagnosis and disease treatment.

4.2.4. Experimental procedures

Materials

CdCl₂·2^{1/2}H₂O (cadmium chloride hemi(pentahydrate), >98%), Na₂TeO₃ (sodium tellurite, 99.5%), ZnCl₂ (zinc chloride, anhydrous, 99.99%), 3-mercaptopropionic acid (MPA, 99%), NaBH₄ (sodium borohydride, >98.0%) and trisodium citrate dehydrate were purchased from Sigma-Aldrich GmbH, Munich. CellTiter-Blue® and CellTiter-Glo® cell viability assay kits were purchased from Promega Corp., USA. For cell culture experiments, Minimum Essential Medium Alpha (MEM-α, Gibco Invitrogen, USA) supplemented with 10% human serum (HS, c.c.pro GmbH, Germany) and 0.5% gentamicin (Biochrom GmbH, Germany) was used as cell culture medium. For 2D cell cultures, 96-well flat bottom standard plates (Sarstedt AG&Co. Germany) and for 3D spheroid cultures, 96-well round bottom plates coated with ultra-low attachment surface (Corning Inc., USA) were used.

Synthesis of CdTe/CdS/ZnS quantum dots

CdTe/CdS/ZnS Qdot were synthesized as described previously [19]. First, CdTe/CdS Qdot having a core_(small)/shell_(thick) structure was synthesized as follows: 21 ml ddH₂O, CdCl₂ (125 mM, 1 ml), 18.5 μl 3-mercaptopropionic acid (MPA), trisodium citrate dehydrate (42.5 mM, 1 ml), sodium tellurite (5 mM, 1 ml) and sodium borohydride (125 mM, 1 ml) were added sequentially into a three-neck round bottom flask. The molar ratio of Cd/Te/MPA was set to be 1/0.04/1.7. Under mixing, the solution pH was adjusted to 11.4 with 1 M NaOH. The reaction solution was then refluxed with an air condenser (Findenser, Radleys, UK) at 90 °C. When the emission wavelength of

CdTe/CdS Qdot reached to 655 ± 5 nm, the nanoparticle growth was stopped by simply cooling the reaction temperature to 4 °C. The as-prepared CdTe/CdS solution was directly used for the external synthesis of ZnS shell. 12 ml of the CdTe/CdS crude solution, 12 ml ddH₂O and 1 ml ZnCl₂ solution (25 mM) were added together giving a final volume of 25 ml. The final pH of the reaction solution was adjusted to 11.5 with 1 M NaOH. Then, the solution was heated slowly to 65 °C and the ZnS shell growth was proceeded for 3 h, yielding in CdTe/CdS/ZnS core_(small)/shell_(thick)/shell_(small) Qdot ($\lambda_{\text{emission}} = 670 \pm 5$ nm), $QY_{\text{max}} \sim 64\%$). Later, samples were precipitated with 2-propanol and collected via centrifugation. The colloidal precipitate was weighed after drying under vacuum and re-dissolved in water. For storage, it was washed with ddH₂O using 10 kDa MWCO PES membrane filters (Vivaspin, Sartorius Stedim Biotech GmbH, Germany) and kept at 4 °C. For cell culture applications, Qdots solutions after dilution with culture medium were filtrated with 0.2 µm pore-sized high-flow syringe filters (Sartorius Stedim Biotech GmbH, Germany) for sterilization.

Cell culture and Qdot treatment

Human adipose-derived mesenchymal stem cells (hAD-MSCs) were isolated from subcutaneous adipose tissues of 3 different patients scheduled for abdominoplasty after obtaining informed written consent, as approved by the Institutional Review Board, project #2251-2014 on 15th May, 2014. The isolated populations have been extensively characterized as mesenchymal stem cells by surface marker analysis and functional properties (differentiation capacity). Cells were cultured with MEM- α medium supplemented with 10% HS and 0.5% gentamicin in standard T-175 culture flasks (Sarstedt AG&Co, Germany) until they reached desired sub-confluency (37 °C, 5% CO₂). After washing with warm PBS, they were detached from the culture flask using accutase solution (Sigma-Aldrich). Following centrifugation at 300 g for 5 min, cell suspension was collected and the number of viable cells was determined by trypan blue exclusion. For 2D culture, 8000 cells in 100 µl of culture medium were seeded to 96-well flat bottom standard plates. After 24 h of adhesion at 37 °C, 5% CO₂, medium was replaced with 100 µl of Qdot solutions diluted with culture medium. A control group was treated with fresh culture medium without Qdots. For 3D culture, two different treatment models were applied according to the Qdot exposure time. In the first model, Qdots were introduced to cells after 24 h when they completed spheroid formation ($t_{\text{QDOT}} = 24$ h). The procedure was performed as follows: 3000 cells in 75 µl of culture

medium were seeded to 96-well round bottom spheroid plates and incubated for 24 h for spheroid formation. Afterwards, 75 μl of Qdot solutions in culture medium were added to each well and incubated further for another 24 h. In the second model, cells were exposed to Qdots solution at the beginning of spheroid formation ($t_{\text{QDOT}} = 0$ h). The procedure was performed as follows: 3000 cells in 75 μl of culture medium and 75 μl of Qdot solutions in culture medium were seeded together to spheroid well-plates and incubated for 24 h (37 °C, 5% CO₂).

For labeling experiments, hAD-MSCs after spheroid formation ($t_{\text{QDOT}} = 24$ h) were treated with Qdot solution (250 $\mu\text{g ml}^{-1}$) for 4 h at 37 °C, 5% CO₂. After Qdot treatment, live cells in spheroids were stained with Calcein-AM (EMD Chemicals, Inc. CA) by adding 1 μl Calcein-AM (1 mg ml^{-1}) solution to the culture medium. Spheroids were washed carefully with PBS prior to DAPI staining. After that, cell nuclei were stained with DAPI (Sigma-Aldrich GmbH, Munich) by adding 100 μl DAPI staining solution (1 $\mu\text{g ml}^{-1}$). After 20 min of incubation spheroids were washed gently with PBS solution and placed on μ -slide glass bottom microscopy chamber slides (ibidi GmbH, Germany) for fluorescence and confocal imaging studies.

Adenosine triphosphate (ATP) assay

ATP assay was performed by using CellTiter-Glo assay kit (Promega Corp., USA) according to manufacturer instructions. Intracellular ATP amount was measured via enzymatic reaction of luciferase in presence of ATP, Mg²⁺ and molecular oxygen. The luminescent signals produced from the reaction are proportional to the amount of ATP present in metabolically active cells. Assay kit enables cell lysis for the release of intracellular ATP for the production of luminescence signal. For 2D cell culture, after removing culture medium, 50 μl CellTiter-Glo stock solution and 50 μl supplement-free MEM- α medium was added to the wells and incubated for 10 minutes (37 °C, 5% CO₂). For 3D spheroid cultures, 75 μl of culture medium was replaced carefully with 75 μl of CellTiter-Glo stock solution and incubated for 2 h under continuous shaking at 250 rpm (37 °C, 5% CO₂) in order to allow spheroid lysis. The resulting luminescence signals were measured with Perkin-Elmer Wallac Victor 2v HTS Counter 1420.

CellTiter-Blue (CTB) assay

The metabolic activity of viable cells in terms of their reduction capacity of resazurin was measured via CTB assay kit (Promega Corp., USA). For 2D cell culture, culture

medium was removed gently and 100 μ l of CTB reagent (diluted 1 : 6 with supplement-free MEM- α medium) was added to each well and incubated for 2 h (37 °C, 5% CO₂). For 3D spheroid cultures, 100 μ l of medium was replaced with CTB reagent (diluted 1 : 4 with supplement-free MEM- α medium, giving a final dilution of 1 : 6). Spheroids incubated for 48 hours under continuous shaking at 250 rpm (37 °C, 5% CO₂) for the release of fluorescence resorufin dye. The resulting fluorescence intensities (544_{Ex}/590_{Em}) were recorded with fluorometer (Fluoroskan Ascent, Thermo Fischer Scientific Inc. USA).

Statistical analysis

Concentration-dependent normalized cell viability data obtained from ATP and CTB assays were fitted from 0 to 100 by using non-linear curve fitting/growth/sigmoidal/dose–response fitting functions (OriginPro 8.6.0 b70, OriginLab Corp. USA). Half-maximal inhibitory concentrations (IC₅₀) were calculated from the fitted dose–response curves. The shown data are from at least two independent experiments, and all individual experiments were conducted with four replicates (n = 4). Levene’s test was performed first to assess the homogeneity of variance of replicates at the level of 0.01 ($\alpha = 0.01$). Then, one-way analysis of variance (ANOVA) and Tukey tests for the comparisons of mean values of independent groups were performed at the level of 0.01 (OriginPro 8.6.0 b70). A significant effect was reported at * $p < \alpha(0.01)$.

Microscopy studies

Bright field images of spheroids were taken prior to viability assays with inverse microscope (Olympus IX50, Olympus Corp., Japan) using cellSens software (cellSens standard 1.7.1, Olympus). The mean diameter of spheroids was measured using areas of spheroids, assuming they are all spherical, with ImageJ 1.49b software. Time-lapse bright field microscope images of spheroids were captured using 4 \times objective with LumaScope 600 microscope (Etaluma Inc., USA). For fluorescence imaging experiments, a fluorescence microscope (Olympus Ix50) equipped with an Olympus camera (SC30, Japan) was used to capture the images of spheroids with cell-Sens Standard (Olympus Co. Japan) software (Excitation filter: BP530-550, barrier filter: BA590). Confocal microscope images were taken using Zeiss LSM-510 Meta (Zeiss, Germany).

4.2.5. Results and discussion

Morphological investigations

Initially, single spheroids in the middle of each well were produced as liquid overlay spheroid cultures in commercially available low-attachment 96 well-plates. Spheroid growth, size and morphology were monitored by means of bright-field and time-lapse microscopy. Spheroid sizes between 100–500 μm have been commonly accepted to be representative of healthy spheroid structures owing to sufficient oxygen and nutrition transport [22–24]. Alternatively, small spheroids (<100 μm) might fail to display the complexity of real tissue with little growth rates, whereas large spheroids (>500 μm) might have pronounced necrotic cores due to diffusion limitations for oxygen and nutrition [22]. For that reason, we produced intermediate sized spheroids with a mean diameter of 312 $\mu\text{m} \pm 20$ (CV = 6%, n = 30) to ensure optimum growth and diffusion rates. The low variation in spheroid size proved the reproducibility of spheroid formation by using low-attachment 96 well-plates which is one of the most important criteria in obtaining reproducible data.

Following this, we investigated the morphological changes of hAD-MSCs spheroids when they were treated with different doses of Qdots, thereby providing initial data on any adverse effects. For this, two different treatment models were used according to Qdot exposure time. In the first model, cells were exposed to Qdots 24 h after formation of the spheroids ($t_{\text{QDOT}} = 24$ h) in order to investigate the effect of Qdots to spheroids. In the second model, cells were treated with Qdots at the beginning of spheroid formation ($t_{\text{QDOT}} = 0$ h) to observe the Qdots effect on the spheroid formation. Firstly, different Qdots concentrations were administered to hAD-MSCs spheroids for 24 h after cells were incubated for 24 h for spheroidal formation ($t_{\text{QDOT}} = 24$ h). Microscope images of spheroids revealed that Qdots induced significant effects to the morphology of hAD-MSCs spheroids with a concentration-dependent manner (**Fig. 1**). Low Qdot concentrations (<300 $\mu\text{g ml}^{-1}$) did not result in any observable alterations to spheroids whereas higher Qdot doses caused a rough surface formation due to protruding of granular shaped cells. As the Qdot concentration was increased to 1200 $\mu\text{g ml}^{-1}$, an observable increase in the surface roughness was pronounced and formation of round cells became obvious, corresponding to a significant increase in cell death. The round cells, however, did not detach from the spheroid, preserving the

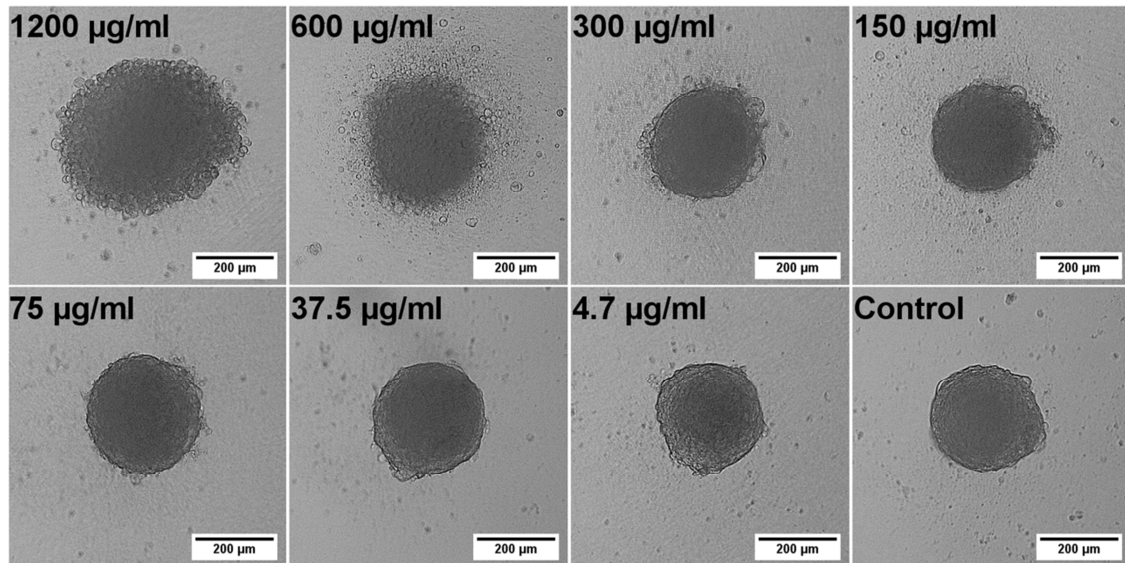


Fig. 1 Bright-field microscope images of hAD-MSCs spheroids treated with different Qdot concentrations for 24 h. The Qdot solutions were introduced to the spheroids after cells were incubated for 24 h for spheroid formation ($t_{\text{QDOT}} = 24$ h). Scale bar is 200 μm .

overall spherical structure, but they increased the diameter of the spheroid by 48%. hAD-MSCs form very tightly packed spheroids due to tight cell junctions preventing cells from losing their interactions and allowing them to remain in the spheroid [18]. Time-lapse microscope images of hAD-MSCs spheroid treated with $1200 \mu\text{g ml}^{-1}$ Qdots are given in **Fig. S1** (see also ESI, **Video S1†**). After 3 h of Qdot exposure, cells started to slowly morph into granular shapes and to swell outward from the spheroid forming a rugged surface, resulting in a concomitant increase in spheroid diameter. Interestingly, the increase in spheroid diameter showed a linear relationship for exposure times in the range of 2 h–8 h ($\text{Adj. } R^2 = 0.977$). After 8 h of exposure, the increase in diameter slowed down and reached a plateau until 20 h (see **ESI, Fig. S2†**). Stem cell spheroids with compact structures might create stronger diffusion barrier for nanoparticle transport, thus mitigate nanoparticle interactions. Despite the fact that NPs *in vivo* face very similar and potentially severe diffusion limitations, we also aimed to explore the effect of Qdots on spheroid formation by seeding the hAD-MSCs directly with Qdots ($t_{\text{QDOT}} = 0$ h), eliminating diffusion related issues, and ensuring that all cells made contact with the Qdots. Following that, the morphologies of spheroids were imaged after 24 h of incubation (**Fig. 2**). Herein, the Qdots induced the cells to undergo more significant morphological alterations in comparison to previous model (**Fig. 1**). At concentrations of $300 \mu\text{g ml}^{-1}$ and lower, the Qdots didn't result in any observable effect, whereas higher amounts elicited distinct changes in the cellular aggregation

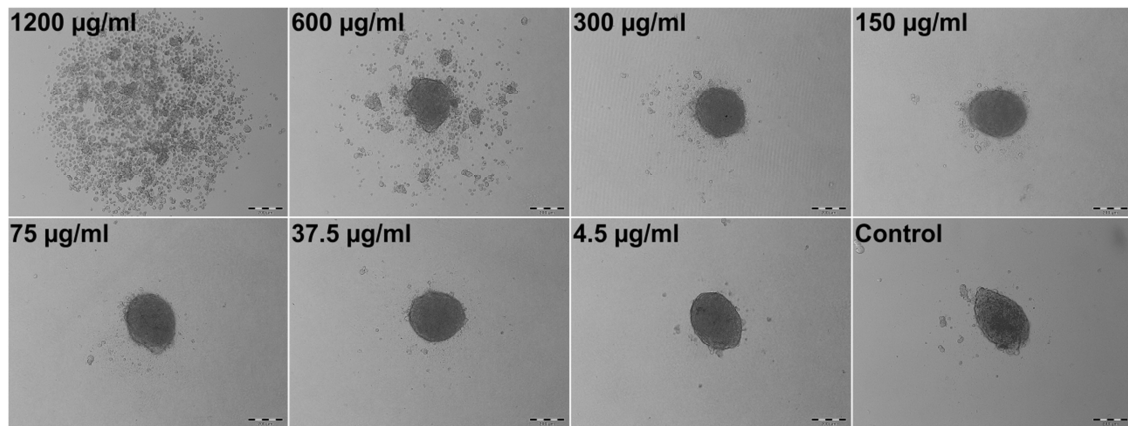


Fig. 2 Effect of Qdot nanoparticles to the formation of hAD-MSCs spheroids. hAD-MSCs were exposed to different Qdot concentrations at the beginning of spheroid formation ($t_{\text{QDOT}} = 0$ h). Bright-field microscope images were taken after 24 h of Qdot treatment. Scale bar is 200 μm .

behaviour of hAD-MSCs. Cell–cell/cell–ECM interactions were weakened significantly resulting in the formation of several smaller spheroids instead of one large spheroid. When cells were exposed to $1200 \mu\text{g ml}^{-1}$ of Qdot, the effect became more significant and cells lost their ability to form aggregates completely. Furthermore, in respect to their granular structure, it can be assumed that they also lost their viability. Consequently, we can confirm that high Qdot doses impaired cell–cell/cell–ECM interactions, thus preventing cells to form spheroids. This drastic phenomenon wasn't observed in the previous 3D model ($t_{\text{QDOT}} = 24$ h). We suggest that, in the later 3D model ($t_{\text{QDOT}} = 0$ h), the cells were not protected by well-developed ECM when they were subjected to toxic Qdot doses. Due to the absence of ECM, their contact with neighboring cells was reduced to a minimum level. Time-lapse microscope images of hAD-MSCs, which were treated with $600 \mu\text{g ml}^{-1}$ Qdots before spheroid formation ($t_{\text{QDOT}} = 0$ h) are presented in **Fig. 3** (see also **ESI, Video S2†**). After 6 h of incubation in the presence of high Qdots concentration, hAD-MSCs started to feature distinct cell aggregation behaviour. Afterwards uneven sized spheroids formation was observed. One explanation for this effect may be the nonspecific interaction of Qdots with transmembrane integrin proteins which may impair the receptor–ligand interactions for cell adhesion. Integrins regulate cell–cell/cell–ECM interactions and therefore play critical roles in cell proliferation, migration, differentiation, adhesion and apoptosis [25]. They were also identified on MSCs cell surfaces and various studies showed their importance for the attachment and survival of MSCs [26]. Shinto *et al.* proposed a nonspecific carboxyl (COOH)–integrin interaction mechanism which may cause

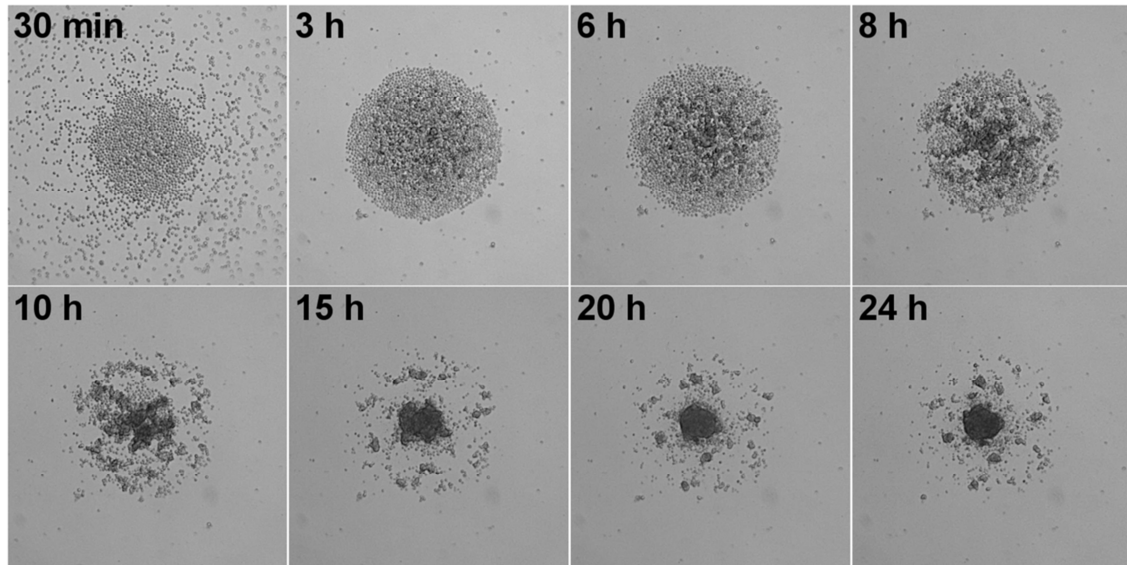


Fig. 3 Time-lapse bright-field microscope images of hAD-MSCs exposed to $600 \mu\text{g ml}^{-1}$ Qdots solution at the beginning of spheroid formation ($t_{\text{QDOT}} = 0 \text{ h}$). The effect of Qdots to the spheroid formation was monitored for 24 h.

blocking of actual integrin–ligand interactions [27]. Since Qdots used in this study utilized surface COOH groups for their aqueous stabilization, such nonspecific COOH/integrin interactions might have occurred. Additionally, unmodified Qdots tend to bind non-specifically to cell membranes in order to reduce their high surface energy [28]. These two phenomena both separately or in combination can result in nonspecific binding of Qdots to cell surface integrin receptors, and in turn might impair cell–cell/cell–ECM interactions. Furthermore, it was found that when the integrin–ligand binding was blocked, the cells rounded up and elevated expression of matrix metalloproteinases (MMPs) which are responsible for partial degradation of surrounding ECM in order to facilitate cell motility [29, 30]. Fujita *et al.* supported these finding by discovering titanium dioxide (TiO_2) nanoparticles induced overexpression of MMPs in 2D cell culture of HaCaT cells [31]. Recently, Liu and co-workers have also found out that gold nanoparticles after being internalized by lung cancer cells modulated cell invasion by causing overexpression of MMPs [32]. Thereby, we can presume that high Qdot doses might exhibit similar inflammatory effects which can be later associated with diminishing cell–cell/cell–ECM interactions in hAD-MSCs. These hypotheses, however, need further examinations.

Cell viability studies

Following the morphology investigations, cell viability assays were performed in order to give more detailed insight into Qdots-based cellular toxicity with respect to hAD-MSCs metabolic activities. Nanoparticles featuring broad absorption spectra such as Qdots, carbon nanotubes and silver nanoparticles might restrict the application of various conventional viability assays based on colorimetric measurements, such as acid phosphatase (APH) and methyl tetrazolium (MTT) assays [33–35], although they were successfully utilized for determination of cell viability in untreated 3D cell cultures [18, 35, 36]. Moreover, high Qdot concentrations can interfere with the signals, thus causing significant false positive results as well as distorted data in viability results [37]. For that reason, we performed adenosine triphosphate (ATP) luminescence cell viability assay and CellTiter-Blue (CTB) fluorescence viability assay as an alternative. The ATP assay is based on the enzymatic activity of luciferase enzyme to produce luminescent oxyluciferin in the presence of ATP, molecular oxygen and Mg^{2+} . The amount of luminescence signal produced from the enzymatic reaction is proportional to the ATP content present in viable cells. ATP assays also require cell lysis for the release of ATP *via* disrupting the cell membrane. Alternatively, the CTB viability assay is based on intracellular reduction of resazurin by metabolically active cells which yield a highly fluorescent resorufin compound. The disruption of cells is not particularly necessary due to the diffusion of reduced resazurin outside of the cells. Therefore, cells maintain their activity during the assay for given incubation periods. Both assays were tested for their cross-reactivity with highest Qdots dose ($1200 \mu\text{g ml}^{-1}$) in cell culture medium in absence of cells and there wasn't any signals detected higher than the background signals.

Concentration-dependent cell viability results including dose–response fit curves obtained from ATP assay are shown in **Fig. 4**. Monolayer 2D cell culture exhibited distinct dose–response pattern featuring biphasic dose–response (non-monotonic) unlike 3D spheroid cultures which exhibited monophasic (monotonic) dose–response pattern. Biphasic behaviour of hAD-MSCs in 2D culture might be explained by presence of two distinct cell populations with different sensitivity to Qdots. Initially, there occurred a sharp decrease in viability to $\sim 50\%$ at concentrations approaching to $20 \mu\text{g ml}^{-1}$. Beyond this concentration point, the viability of cells was decreased slightly when the dose was increased to $150 \mu\text{g ml}^{-1}$. This was followed by a moderate

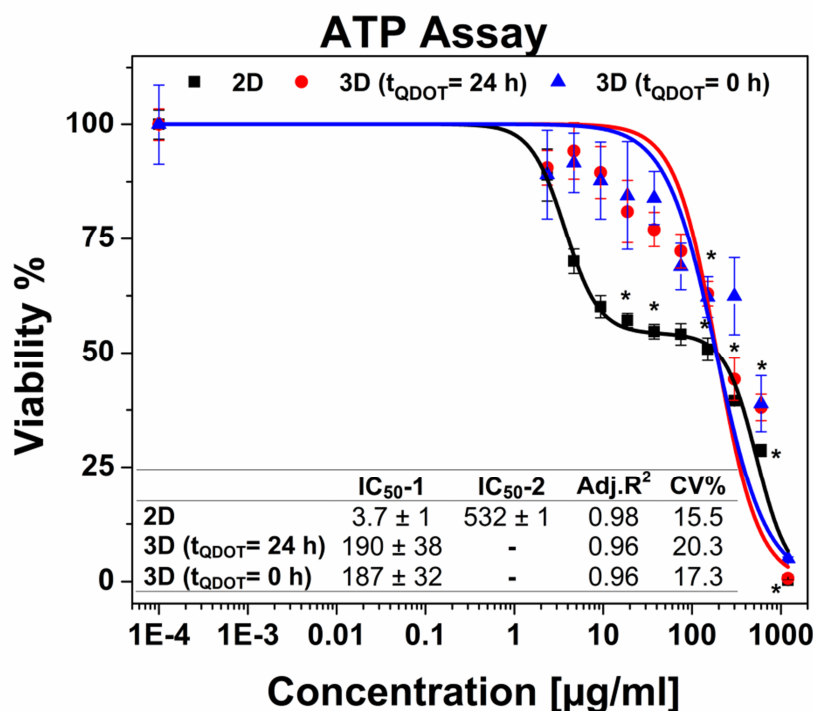


Fig. 4 Cell viability data obtained from ATP assay. Data points are means \pm standard error of 3 ± 1 independent experiments which each were conducted in 4 replicates. * indicates significant difference at 0.01 level. $p < \alpha = 0.01$ (ANOVA one-way). Inset table shows half-maximal inhibitory concentrations (IC₅₀) in $\mu\text{g ml}^{-1}$. 2D cell culture having a biphasic dose–response curve possesses two IC₅₀ values (IC₅₀-1 and IC₅₀-2) whereas each 3D spheroid cultures have one IC₅₀ value owing to monotonic dose–response pattern. Acceptance criteria is CV (coefficient of variance) $< 20\%$.

decrease at the highest Qdot concentration ($1200 \mu\text{g ml}^{-1}$) at which all cells were dead. Meanwhile, 3D spheroid cultures demonstrated higher resistance to Qdot induced cellular toxicity than 2D culture with a mean IC₅₀ value of $190 \mu\text{g ml}^{-1}$ for 3D (t_{QDOT} = 24 h) and $187 \mu\text{g ml}^{-1}$ for 3D (t_{QDOT} = 0 h). Accordingly, the exposure of cells to Qdots didn't result in pronounced adverse alterations of the viability of the 3D (t_{QDOT} = 0 h) model despite cells being exposed to Qdots at the beginning of spheroid formation. Consequently, cells sustained their viability at the similar levels in both 3D models. The dose-dependent viability responses acquired from CTB assay for 3D cultures demonstrated an increase in viability at low Qdot doses in comparison to control samples (see ESI Fig. S3†). One may attribute this result to hormesis, which is a low-dose stimulatory or inhibitory effect in dose–responses above or below the toxicological thresholds [38]. NP-induced hormesis was attributed to increasing ROS levels with low-doses, giving rise to cell activities to suppress the imbalance, thus causing an increase in metabolic activities [39]. So far, various studies reported for several nanoparticles (CdTe, TiO₂, aluminium NPs, single-walled carbon nanotubes)

inducing hormesis [40, 41]. Though, CTB assay for 2D culture and ATP assay for 3D cultures didn't demonstrate similar patterns. Hence, we can neglect the possibility of hormesis. Meanwhile, O'Brien *et al.* described that cell lines with high metabolic rates can reduce resazurin further to colourless and nonfluorescent hydroresorufin [42]. In such a case, untreated cells with high metabolic activity can further reduce resazurin to nonfluorescent hydroresorufin resulting in low fluorescent signals at the end-point in comparison to treated cells [42–44]. This can lead to unsubstantial results causing misinterpretation of data and underestimation of cell activity. Moreover, in this study, the resazurin incubation time was prolonged to 48 h because of the slow diffusion of reduced resazurin from highly compact structured hAD-MSCs spheroids. Fluorescence signals only reached detectable levels after 48 h. For that reason, we can presume that the prolonged incubation time for resazurin (48 h) may have enabled over-reduction of resazurin by untreated cells followed by a decrease in their fluorescence signals. In the mean meantime, cells treated with Qdots sustained their reduction capacity and respectively produced higher signals than control samples. We should also note that, resazurin dye, also known as Alamar Blue, was proved to be toxic to the cells for long incubation periods (>24 h) [42, 45]. Finally, signal qualities of ATP and CTB assays were compared by determining signal-to-noise (S/N) ratios for all culture types. For 2D cultures, S/N ratios were calculated to be 172 ± 19 for ATP assay and 11 ± 4 for CTB assay. For 3D cultures, S/N ratios were estimated to be 27 ± 4 for ATP assay and 4 ± 1 for CTB assay. Consequently, ATP assay signal qualities were found to be 16-fold greater in 2D culture and 7-fold in 3D culture than CTB assay. We therefore concluded that the CTB assay is not a reliable method for the determination of Qdot toxicity in the case of highly active and densely-packed hAD-MSCs spheroids. However, other cell lines particularly those forming loose cell aggregates and have relatively low metabolic activities, such as A549 lung carcinoma, HepG2 hepatocellular carcinoma and medulloblastoma tumour cells, may be suitable for CTB assay [22, 46].

Similar to our findings, conventional monolayer cell cultures being more sensitive against NPs or drug molecules in comparison to various 3D cell culture systems have been also reported by other groups [5, 47–50]. According to the Lee and coworkers report, where they assessed single-dose toxicity of CdTe Qdots on HepG2 spheroid cultures, $10 \mu\text{g ml}^{-1}$ of CdTe reduced the cell viability to 56% in 2D culture and 31% in 3D culture after 12 h of Qdot exposure [18]. The results of the study cannot be directly compared to our findings since different cell types as well as different Qdot

compositions were tested. Nevertheless, we can state that the same dose ($10 \mu\text{g ml}^{-1}$) for core/shell/shell CdTe/CdS/ZnS Qdots did not cause any damage to hAD-MSCs spheroids. This may be attributed to the presence of protective outer shell layers acting as a strong barrier against Cd^{2+} leakage [19].

Regarding *in vivo* Qdot-induced toxicity analysis; Hauck *et al.* reported that CdSe/ZnS core/shell Qdot did not show any significant toxicity in healthy Sprague–Dawley rats [51]. Later, Chou *et al.* confirmed that Cd, Se and Zn containing Qdot did not cause toxicity in rats in 90 days [52]. Another study reported by Nurunnabi *et al.* pointing out that carboxylated graphene Qdots did not induce apparent toxicity in rats after 22 days of exposure [53]. The discrepancy in results in the context of Qdot toxicity between monolayer cell cultures and animal models was attributed to the presence of complex physiological processes in the body that NPs inevitable undergo after their uptake. Their circulation in blood stream, accumulation by specific organs and renal excretion play a deterministic role for their fate in the body [35]. Yet, structural diversities in Qdot properties, such as size, shape, charge, material composition, and surface chemistry etc., necessitate the investigation of every Qdot structure-based effects individually. We also note that petri-dish cultures lack all of these physiological processes, being isolated on plastic substrates and therefore all cells facilitate NP interactions easily without facing any transport limitations. On the other hand, complex and diverse *in vivo* uptake mechanisms reduce the interaction of Qdots with the target organ and therefore they cooperatively act to minimize the adverse effects of Qdots. Nevertheless, developments for *in vitro* 3D cultures fortify their potential to fill the gap between petri-dish cultures and animal models with the hope that they will also decrease the use of laboratory animals.

Labeling spheroids with Qdots

Carboxyl-functionalized Qdot were tested for their applicability in 3D spheroid imaging. For that, hAD-MSC spheroids treated with Qdots were monitored with fluorescence and confocal microscopes, and the obtained images are presented in **Fig. 5**. Fluorescence microscope images with a standard (x, y) view illustrated surface fluorescence of labelled spheroid (**Fig. 5a**). On the other hand, z-stacked confocal images provided a better insight to the penetration and the uptake of Qdots in spheroids [54]. According to the fluorescence confocal images, after 4 h Qdots appeared to be uptaken mostly by peripheral cells in the spheroid structure. As it can be seen from

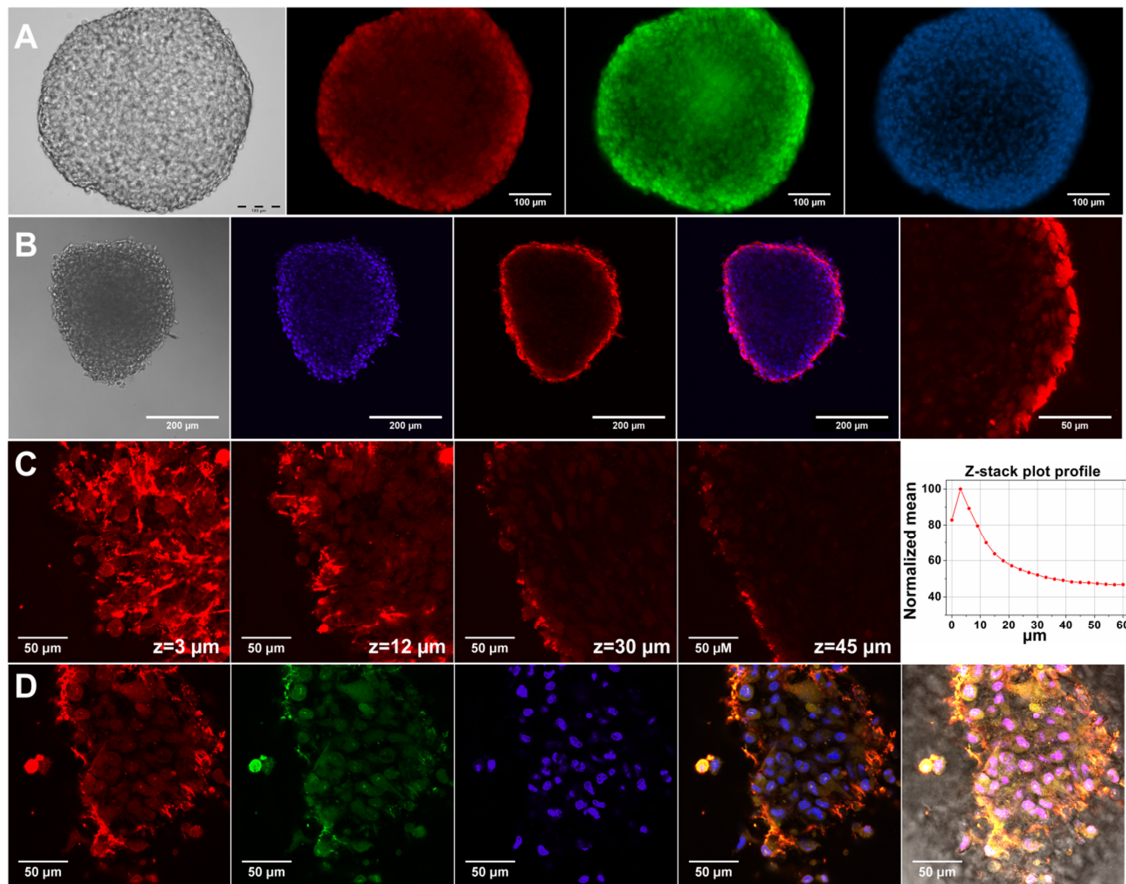


Fig. 5 Fluorescence imaging of hAD-MSCs spheroids treated with CdTe/CdS/ZnS Qdots for 4 h. (A) Fluorescence images captured from fluorescence microscopy from left-to-right: bright-field, Qdot (red), Calcein-AM (green) and DAPI (blue). (B) Single plane confocal images collected with 10 \times objective, from left-to-right: bright-field, DAPI (blue), Qdot (red), merge image of Qdot + DAPI and magnified spheroid. (C) Z-stacked confocal images of spheroid at individual z-planes. Z-stacks were acquired with 3 μ m step size. The inserted graphic shows z-stack plot profile for normalized Qdot fluorescence mean intensity versus z-stack height (μ m). (D) Single-plane confocal fluorescence images of spheroid at the bottom surface, from left-to-right: Qdot (red), Calcein-AM (green), DAPI (blue), merged image of Qdot + Calcein-AM + DAPI, and merge image of bright-field + Qdot + Calcein-AM + DAPI.

Fig. 5b, strong red fluorescence signals appeared only at the outer region, while signals decreased towards the inner region of the spheroid. In **Fig. 5c**, z-stacked images taken at individual z-planes at 3 μ m step size from bottom surface towards centre of spheroid showed that highest Qdot labelling occurred at peripheral regions. Z-stack mean intensity plot (**Fig. 5d-right**) reveals that fluorescence intensity of Qdots decreases by 50% within 36 μ m focal distance. These observations might suggest presence of diffusion limitations for the transport of Qdots into spheroid inner region [55]. Fluorescence images taken from the bottom edge of the spheroid (**Fig. 5d**) show that Qdots were internalized by the cells rather than being non-specifically captured by extracellular matrix material. Live cell staining with Calcein-AM (**Fig. 5d**) shows that

cells at the bottom surface of the spheroid retained their viability during Qdot treatment; thus, uptake of Qdots did not induce cell death. As a result, within the given incubation time (4 h) Qdots enabled staining into intact stem cell spheroids due to their inherent small size and surface structure. We can conclude that penetration of Qdots into tissue-like intact spheroid structures can make them a suitable tool for targeted imaging and drug delivery studies.

4.2.6. Conclusions

In summary, we described for the first time the dose-dependent adverse effects of CdTe/CdS/ZnS core_(small)/shell_(thick)/shell_(small) Qdots on the 3D spheroid culture of primary human mesenchymal stem cells. Morphological alterations in spheroid models ($t_{\text{QDOT}} = 0$ h, $t_{\text{QDOT}} = 24$ h) caused by toxic levels of Qdots revealed distinct characteristics. Either end-point microscope images or time-lapse studies demonstrated that Qdots expressed more drastic effect on spheroid formation, where cells were incubated in presence of Qdots during cell aggregation. Additionally, we detected a correlation in the spheroid diameters with increasing Qdot concentrations when hADMSCs were exposed to Qdots after spheroid formation ($t_{\text{QDOT}} = 24$ h). Further, ATP and CTB cell viability tests were assayed to address the impact of dose-dependent Qdot toxicity to cell metabolic activities. According to ATP assays, significant differences were observed between 2D and 3D cell cultures. Interestingly, dose-response curves for 2D culture featured a reproducible biphasic curve model in contrast to spheroid cultures with monotonic dose-response patterns. As a result, monolayer cell cultures, on one side attaching to plastic substrate and on the other side being exposed to medium and having only periphery cell contacts, were found to be more susceptible to Qdot toxicity. Alternatively, in 3D spheroids, fully formed cell-cell and cell-ECM interactions in all three dimensions played a protective role and resulted in greater resistance to Qdot-induced toxicity. Meanwhile, CTB assays were proved to be an unreliable viability assay for densely packed stem cell spheroids due to diffusion limitations for resazurin/resorufin and therefore produced aberrant results. Overall, well-defined 3D spheroid cultures with the presence of microtissue-like cell clusters and ECM layer as well as mass transport characteristics constitute an initial testing platform to address physiologically relevant toxicity issues of nanoparticles for automated cell based high-throughput screening methods. Lastly, penetration ability of

highly-fluorescent CdTe/CdS/ZnS Qdots demonstrates versatility of Qdots in 3D spheroid imaging. Their optical and structural features can be utilized in the future for targeted imaging and delivery studies using solid tumor spheroids.

4.2.7. Acknowledgements

This work was supported by BioFabrication for NIFE (initiative, which is financially supported by the Lower Saxony ministry of Science and Culture and the Volkswagen Foundation). We also would like to thank Dr Patrick Lindner for his support for statistical analysis, Prof. Dr-Ing. Birgit Glasmacher and Dr Lutz Dreyer (Institute for Multiphase Processes, Leibniz University of Hanover) for providing us access to confocal microscope and for their additional support with the analysis.

4.2.8. References

1. F. Pampaloni, E. G. Reynaud and E. H. K. Stelzer, *Nat. Rev. Mol. Cell Biol.*, 2007, **8**, 839–845.
2. M. M. Stevens, *Nat. Nanotechnol.*, 2009, **4**, 342–343.
3. E. L. da Rocha, L. M. Porto and C. R. Rambo, *Mater. Sci. Eng., C*, 2014, **34**, 270–279.
4. L. G. Griffith and M. A. Swartz, *Nat. Rev. Mol. Cell Biol.*, 2006, **7**, 211–224.
5. E. Kim, W. B. Jeon, S. Kim and S. K. Lee, *J. Nanosci. Nanotechnol.*, 2014, **14**, 3356–3365.
6. E. Fennema, N. Rivron, J. Rouwkema, C. van Blitterswijk and J. de Boer, *Trends Biotechnol.*, 2013, **31**, 108–115.
7. A. C. Luca, S. Mersch, R. Deenen, S. Schmidt, I. Messner, K. L. Schafer, S. E. Baldus, W. Huckenbeck, R. P. Piekorz, W. T. Knoefel, A. Krieg and N. H. Stoecklein, *PLoS One*, 2013, **8**, e59689.
8. N. T. Elliott and F. Yuan, *J. Pharm. Sci.*, 2011, **100**, 59–74.
9. A. Ivascu and M. Kubbies, *J. Biomol. Screening*, 2006, **11**, 922–932.
10. X. L. Zhang, W. Wang, W. T. Yu, Y. B. Xie, X. H. Zhang, Y. Zhang and X. J. Ma, *Biotechnol. Prog.*, 2005, **21**, 1289–1296.
11. T. T. Goodman, C. P. Ng and S. H. Pun, *Bioconjugate Chem.*, 2008, **19**, 1951–1959.
12. Z. H. Li and Z. F. Cui, *Biotechnol. Adv.*, 2014, **32**, 243–254.
13. M. Akin, R. Bongartz, J. G. Walter, D. O. Demirkol, F. Stahl, S. Timur and T. Scheper, *J. Mater. Chem.*, 2012, **22**, 11529–11536.
14. R. Tang, J. Xue, B. Xu, D. Shen, G. P. Sudlow and S. Achilefu, *ACS Nano*, 2015, **9**, 220–230.
15. C. E. Probst, P. Zrazhevskiy, V. Bagalkot and X. Gao, *Adv. Drug Delivery Rev.*, 2013, **65**, 703–718.
16. D. Ag, R. Bongartz, L. E. Dogan, M. Selec, J. G. Walter, D. O. Demirkol, F. Stahl, S. Ozelik, S. Timur and T. Scheper, *Colloids Surf., B*, 2014, **114**, 96–103.
17. M. Bottrill and M. Green, *Chem. Commun.*, 2011, **47**, 7039–7050.
18. J. Lee, G. D. Lilly, R. C. Doty, P. Podsiadlo and N. A. Kotov, *Small*, 2009, **5**, 1213–1221.
19. M. Ulusoy, J. G. Walter, A. Lavrentieva, I. Kretschmer, L. Sandiford, A. Le Marois, R. Bongartz, P. Aliuos, K. Suhling, F. Stahl, M. Green and T. Scheper, *RSC Adv.*, 2015, **5**, 7485–7494.

20. A. L. Rogach and M. Ogris, *Curr. Opin. Mol. Ther.*, 2010, **12**, 331–339.
21. P. Chang, Y. Qu, Y. Liu, S. Cui, D. Zhu, H. Wang and X. Jin, *Cell Death Dis.*, 2013, 4e99175.
22. D. P. Ivanov, T. L. Parker, D. A. Walker, C. Alexander, M. B. Ashford, P. R. Gellert and M. C. Garnett, *PLoS One*, 2014, **9**.
23. A. Asthana and W. S. Kisaalita, *Drug Discovery Today*, 2012, **17**, 810–817.
24. Y. Gao, M. G. Li, B. Chen, Z. C. Shen, P. Guo, M. GuillaumeWientjes and J. L. S. Au, *AAPS J.*, 2013, **15**, 816–831.
25. O. Lieleg, M. Lopez-Garcia, C. Semmrich, J. Auernheimer, H. Kessler and A. R. Bausch, *Small*, 2007, **3**, 1560–1565.
26. D. Docheva, C. Popov, W. Mutschler and M. Schieker, *J. Cell. Mol. Med.*, 2007, **11**, 21–38.
27. H. Shinto, Y. Aso, T. Fukasawa and K. Higashitani, *Colloids Surf. B*, 2012, **91**, 114–121.
28. A. Lesniak, A. Salvati, M. J. Santos-Martinez, M. W. Radomski, K. A. Dawson and C. Aberg, *J. Am. Chem. Soc.*, 2013, **135**, 1438–1444.
29. C. Brakebusch, D. Bouvard, F. Stanchi, T. Saki and R. Fassler, *J. Clin. Invest.*, 2002, **109**, 999–1006.
30. L. Heckmann, J. Fiedler, T. Mattes and R. E. Brenner, *Cells Tissues Organs*, 2006, **182**, 143–154.
31. K. Fujita, M. Horie, H. Kato, S. Endoh, M. Suzuki, A. Nakamura, A. Miyauchi, K. Yamamoto, S. Kinugasa, K. Nishio, Y. Yoshida, H. Iwahashi and J. Nakanishi, *Toxicol. Lett.*, 2009, **191**, 109–117.
32. Z. X. Liu, Y. C. Wu, Z. R. Guo, Y. Liu, Y. J. Shen, P. Zhou and X. Lu, *PLoS One*, 2014, **9**, e99175.
33. P. V. AshaRani, G. L. K. Mun, M. P. Hande and S. Valiyaveetil, *ACS Nano*, 2009, **3**, 279–290.
34. J. M. Worle-Knirsch, K. Pulskamp and H. F. Krug, *Nano Lett.*, 2006, **6**, 1261–1268.
35. K. M. Tsoi, Q. Dai, B. A. Alman and W. C. W. Chan, *Acc. Chem. Res.*, 2013, **46**, 662–671.
36. J. Friedrich, W. Eder, J. Castaneda, M. Doss, E. Huber, R. Ebner and L. A. Kunz-Schughart, *J. Biomol. Screening*, 2007, **12**, 925–937.
37. N. A. Monteiro-Riviere, A. O. Inman and L. W. Zhang, *Toxicol. Appl. Pharmacol.*, 2009, **234**, 222–235.
38. M. A. Nascarella and E. J. Calabrese, *Dose-Response*, 2012, **10**, 344–354.
39. Y. Y. Guo, J. Zhang, Y. F. Zheng, J. Yang and X. Q. Zhu, *Mutat. Res., Genet. Toxicol. Environ. Mutagen.*, 2011, **721**, 184–191.
40. E. Jan, S. J. Byrne, M. Cuddihy, A. M. Davies, Y. Volkov, Y. K. Gun'ko and N. A. Kotov, *ACS Nano*, 2008, **2**, 928–938.
41. I. Iavicoli, E. J. Calabrese and M. A. Nascarella, *Dose-Response*, 2010, **8**, 501–517.
42. J. O'Brien, I. Wilson, T. Orton and F. Pognan, *Eur. J. Biochem.*, 2000, **267**, 5421–5426.
43. A. Romoser, D. Ritter, R. Majitha, K. E. Meissner, M. McShane and C. M. Sayes, *PLoS One*, 2011, **6**, e22079.
44. D. Breznán, D. Das, C. MacKinnon-Roy, B. Simard, P. Kumarathasan and R. Vincent, *Toxicol. in Vitro*, 2015, **29**, 142–147.
45. H. Gloeckner, T. Jonuleit and H. D. Lemke, *J. Immunol. Methods*, 2001, **252**, 131–138.
46. F. Sambale, A. Lavrentieva, F. Stahl, C. Blume, M. Stiesch, C. Kasper, D. Bahnemann and T. Scheper, *J. Biotechnol.*, 2015, **205**, 120–129.
47. D. R. Albrecht, G. H. Underhill, T. B. Wassermann, R. L. Sah and S. N. Bhatia, *Nat. Methods*, 2006, **3**, 369–375.
48. M. Bokhari, R. J. Carnahan, N. R. Cameron and S. A. Przyborski, *J. Anat*, 2007, **211**, 567–576.
49. M. Oishi, Y. Nagasaki, N. Nishiyama, K. Itaka, M. Takagi, A. Shimamoto, Y. Furuichi and K. Kataoka, *ChemMedChem*, 2007, **2**, 1290–1297.
50. D. Mueller, L. Kramer, E. Hoffmann, S. Klein and F. Noor, *Toxicol. in Vitro*, 2014, **28**, 104–112.

51. T. S. Hauck, R. E. Anderson, H. C. Fischer, S. Newbigging and W. C. W. Chan, *Small*, 2010, **6**, 138–144.
52. L. Y. T. Chou and W. C. W. Chan, *Nat. Nanotechnol.*, 2012, **7**, 416–417.
53. M. Nurunnabi, Z. Khatun, K. M. Huh, S. Y. Park, D. Y. Lee, K. J. Cho and Y. K. Lee, *ACS Nano*, 2013, **7**, 6858–6867.
54. V. Charwat, K. Schutze, W. Holnthoner, A. Lavrentieva, R. Gangnus, P. Hofbauer, C. Hoffmann, B. Angres and C. Kasper, *J. Biotechnol.*, 2015, **205**, 70–81.
55. A. I. Astashkina, C. F. Jones, G. Thiagarajan, K. Kurtzeborn, H. Ghandehari, B. D. Brooks and D. W. Grainger, *Biomaterials*, 2014, **35**, 6323–6331.

4.2.9. Supplementary Information

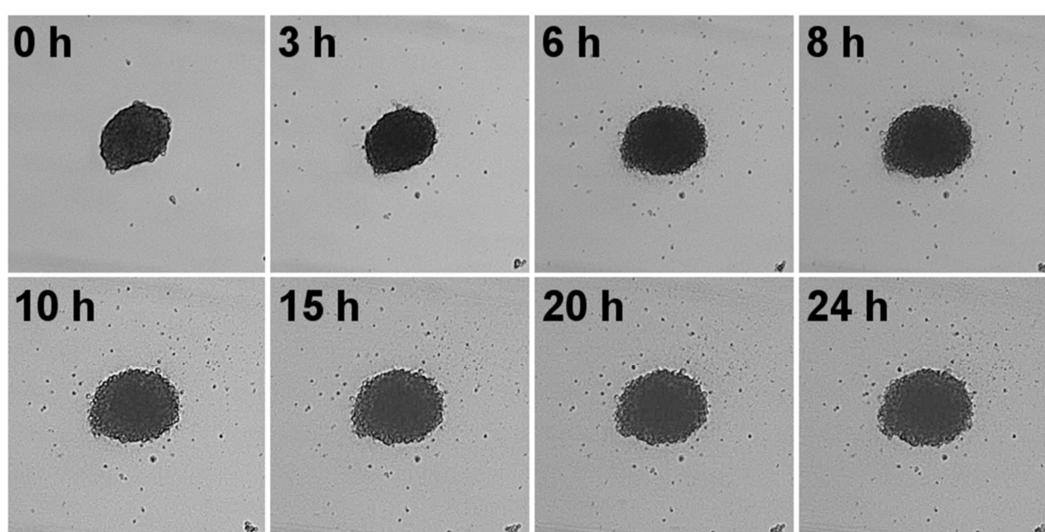


Fig. S1 Time-lapse microscope images of hAD-MSCs spheroids treated with 1200 $\mu\text{g/ml}$ Qdot solution. Qdots were introduced to the spheroid after cells were incubated for 24 h for spheroid formation ($t_{\text{QDOT}} = 24$ h). Effect of Qdots to spheroid morphology was monitored for 24 h.

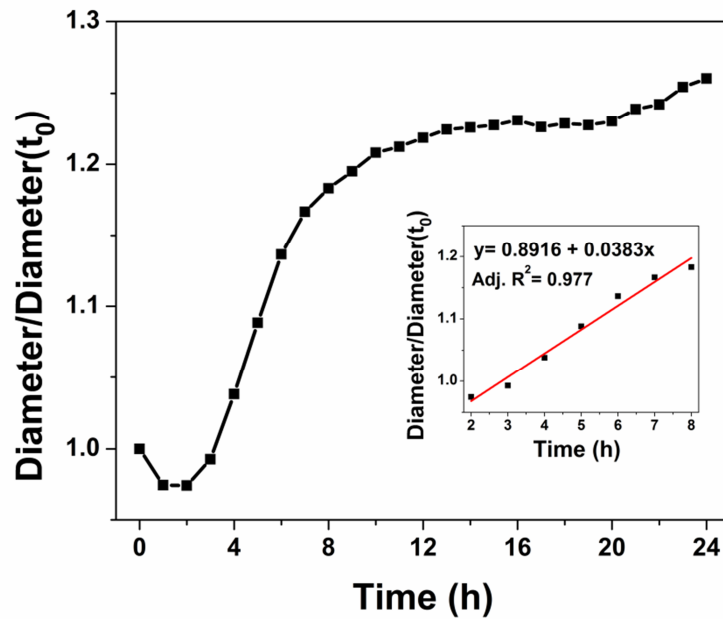


Fig. S2 Increase in hAD-MSCs spheroid diameters during Qdot exposure ($1200 \mu\text{g ml}^{-1}$) until 24 h. Spheroid diameters were normalized to the diameter of spheroid at the time= 0 h. Inset graph shows the linear relationship between the Qdot exposure time and the increase in spheroid diameter until 8 h (Adj. $R^2=0.977$).

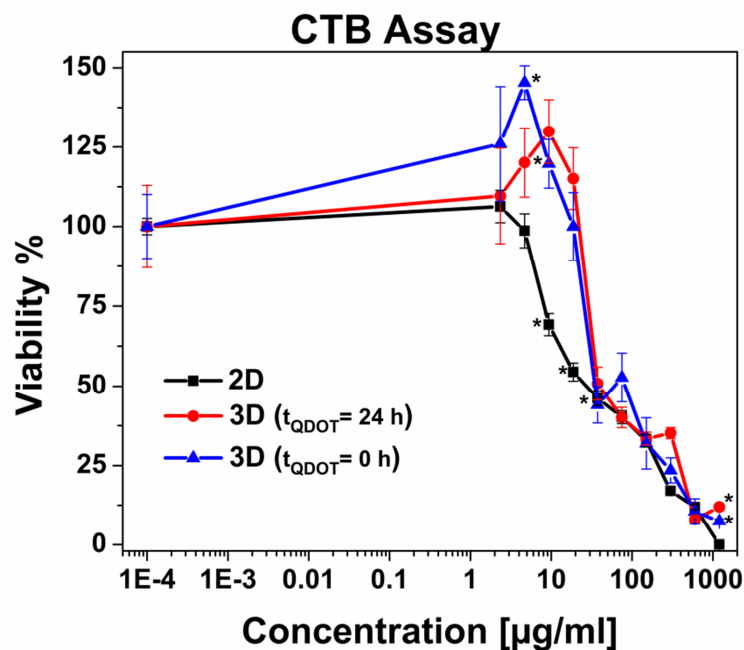
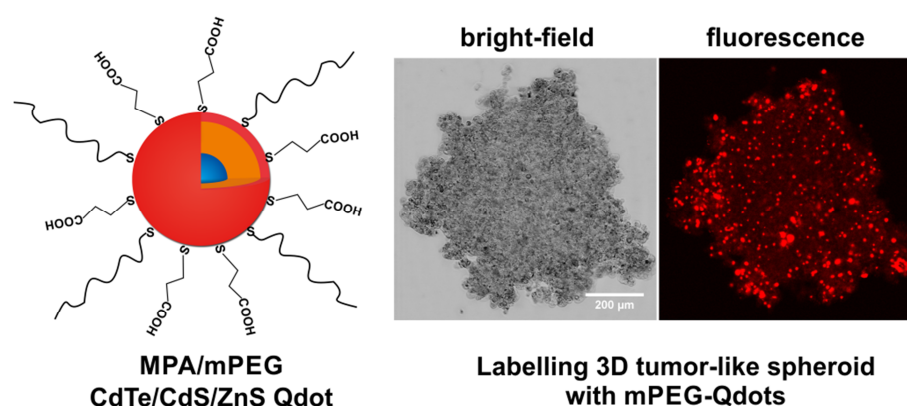


Fig. S3 Cell viability data obtained from CTB assay. The fluorescence signals were normalized to untreated control samples. Data points are means \pm standard error of 3 ± 1 independent experiments which were conducted with 4 replicates. * indicates significant difference at 0.01 level. $p < \alpha=0.01$ (ANOVA one-way).

4.3. Surface modification of Qdots with mPEG ligands

The results of this chapter were published as Ulusoy *et al.*, Aqueous synthesis of PEGylated quantum dots with increased colloidal stability and reduced cytotoxicity, *Bioconjugate Chemistry*, 2015, doi: 10.1021/acs.bioconjchem.5b0049. It was reproduced with permission from American Chemical Society, 2016.

Table of Content Graphic



4.3.1. Summary

In this chapter, development of CdTe/CdS/ZnS quantum dots (Qdots) with improved surface characteristics was aimed in order to increase colloidal stability of Qdots and amend their cytotoxicity issues. As is known, ligands used to manufacture the outer layer of colloidal nanoparticles (NPs) have a significant impact on physicochemical properties of NPs. Moreover, they play a deterministic role for interactions of NPs with their biological environment. In this sense, polyethylene glycol (PEG) molecules have found to be the most effective surface capping ligands due to their hydrophilic and non-toxic nature, as well as high exclusion volume. As a result, they improve colloidal stability of NPs via steric repulsion, and therefore reduce NPs-induced toxicity. Moreover, they mitigate nonspecific cellular interactions due to their high resistance to protein adsorption. They also hinder recognition of NPs by the immune system, thus reducing NP clearance by the reticuloendothelial system (RES).

Herein a practical and generic approach for *in situ* introduction of thiol-terminated methoxyPEG (mPEGthiol) groups to the surface of CdTe/CdS/ZnS Qdots was reported. By using a one-pot aqueous approach, deposition of a ZnS outer shell in the presence of 3-mercaptopropionic acid (MPA) and mPEGthiol molecules was achieved. In this *in situ* route, mPEG molecules and carboxyl groups of MPA were simultaneously incorporated to the outer ZnS shell surface to facilitate water solubilization as well as further functionalization of Qdots. Following the synthesis, the effect of mPEG ligands on the physicochemical properties of Qdots in terms of ZnS shell growth rate, surface characteristics, and colloidal stability were investigated. In the first chapter, it was shown that ZnS shell deposition virtually minimized Qdot-induced *in vitro* cytotoxicity and increased photostability. Nevertheless, slow oxidation of ZnS can cause loss of surface sulphur atoms under ambient conditions over time. This process will eventually result in decomposition of the ZnS shell, thus, adverse affects of Qdots will be induced again. Taking this into consideration, the effect of mPEG surface ligands on the cellular toxicity of Qdots was tested as a function of mPEG grafting density. To test dose-dependent *in vitro* cytotoxicity of PEGylated Qdots, two-dimensional (2D) monolayer cultures of A549 lung adenocarcinoma cells and three-dimensional (3D) tumor-like spheroid cultures were used. In the later step, cellular binding features of the resulting mPEG–Qdots were examined by using 3D tumor-like spheroids. By utilizing 3D tumor-like spheroids, interaction of PEGylated Qdots with physiologically relevant micro-scale tissue-like structures was explored in order to predict *in vivo* behavior of Qdots in the sense of cellular binding and uptake.

Overall, the results of this study showed that mPEG ligands influenced Qdot characteristics in a varying manner with respect to the grafting density of surface mPEG groups. A low mPEG density demonstrated a minimal effect on the deposition of the ZnS shell, and fluorescence efficiency of the resulting Qdots remained unchanged. Meanwhile, a higher mPEG density caused a significant decrease in ZnS deposition rate with a subsequent decrease in fluorescence efficiency. However, they were found to increase colloidal stability of Qdots, and mitigate Qdot-induced adverse effects to a great extent. Flow cytometry and confocal microscopy studies revealed that at a high mPEG grafting amount, Qdots showed minimal non-specific binding to cells and a low adsorption rate in 3D spheroid structures in comparison to their lesser- or nonPEGylated counterparts. After 24 h incubation with 3D spheroids, nonPEGylated

Qdots and Qdots with low mPEG density were internalized by outer cells, and their fluorescence intensities decreased towards the spheroid inner regions. In the meantime, Qdots with high mPEG density generally remained at the cell membranes with a partial internalization by outer cells, and they preserved their fluorescence intensity.

In summary, mPEG molecules were successfully coupled to the surface of Qdots by using *in situ* aqueous approach. PEGylated Qdots exhibited an increased colloidal stability, decreased *in vitro* toxicity, and minimized nonspecific cellular interactions. Moreover, 3D tumor-like spheroids provided a physiologically relevant platform to test the applicability of PEGylated Qdot to visualize 3D spheroid structures and to analyze their binding characteristics.

4.3.2. Abstract

Ligands used on the surface of colloidal nanoparticles (NPs) have a significant impact on physiochemical properties of NPs and their interaction in biological environments. In this study, we report a one-pot aqueous synthesis of 3-mercaptopropionic acid (MPA)-functionalized CdTe/CdS/ZnS quantum dots (Qdots) in the presence of thiol-terminated methoxy polyethylene glycol (mPEG) molecules as a surface coordinating ligand. The resulting mPEG-Qdots were characterized by using ζ potential, FTIR, thermogravimetric (TG) analysis, and microscale thermophoresis (MST) studies. We investigated the effect of mPEG molecules and their grafting density on the Qdots photophysical properties, colloidal stability, protein binding affinity, and *in vitro* cellular toxicity. Moreover, cellular binding features of the resulting Qdots were examined by using three-dimensional (3D) tumor-like spheroids, and the results were discussed in detail. Promisingly, mPEG ligands were found to increase colloidal stability of Qdots, reduce adsorption of proteins to the Qdot surface, and mitigate Qdot-induced side effects to a great extent. Flow cytometry and confocal microscopy studies revealed that PEGylated Qdots exhibited distinctive cellular interactions with respect to their mPEG grafting density. As a result, mPEG molecules demonstrated a minimal effect on the ZnS shell deposition and the Qdot fluorescence efficiency at a low mPEG density, whereas they showed pronounced effect on Qdot colloidal stability, protein binding affinity, cytotoxicity, and nonspecific binding at a higher mPEG grafting amount.

4.3.3. Introduction

Colloidal nanoparticles (NPs) have become an important class of nanomaterials with potential for applications ranging from medicine to optoelectronic devices [1]. The efforts of physical and material scientists to engineer NPs with unique material compositions and surface chemistries have led to tremendous progress in biological sciences to accomplish effective sensing, targeted delivery, imaging, and disease treatment [2]. Despite all the work to exploit their unique characteristics in biomedical sciences, still little is known with respect to their interactions with complex biological environments [3]. One of the dominating factors for NP interactions in their environments is the nature of their organic ligand coating (e.g., structure, ionic nature, packing density, hydrophobicity) that influences NP binding and uptake characteristics to a great extent [4]. Even slight changes in surface functionalities might lead to greatly varying cellular internalization [5], indicating that the effect of NP surface physiochemical properties on their cellular interactions is far more complicated than currently acknowledged [6, 7]. When NPs are exposed to biological environments, they inevitably interact with serum proteins, which are adsorbed onto the NP surface, forming so-called “protein corona” structures [8]. Adsorption of proteins to NP surfaces strongly affects the rate of NP adhesion to cell membranes, which is one of the key determinants for NP uptake efficiency. For instance, lower adhesion due to the presence of biomolecular corona may cause a decrease in nanoparticle internalization or might induce specific recognition of proteins adsorbed to the NP by cell membrane receptors and therefore mediate NP uptake via receptor-mediated endocytic pathways [6, 9]. For *in vivo* applications, nonspecific interactions are not desired because they can hinder projected targeting and delivery; furthermore their accumulation can cause adverse effects by impairing membrane integrity [10]. For that reason, engineering of NP surfaces to optimize physiochemical characteristics in order to reduce nonspecific interactions is a prerequisite to the application of NPs.

Among various approaches, surface modification of NPs with polyethylene glycol (PEG) ligands has proved to be one of the most successful strategies [11]. PEG ligands are nonbranched polymers that have high exclusion volumes due to their high conformational entropy, so as a result, they repel biomolecules [12]. Moreover, they provide colloidal stability via steric repulsion and introduce higher flexibility to NP surfaces; they have high resistance to protein adsorption and therefore reduce

nonspecific NP–cell membrane interactions [13-15]. Their hydrophilic and nontoxic nature also mitigates NP-induced adverse effects by preventing chemical degradation of NPs and release of their metal ions to intracellular environments [16, 17]. They also hinder recognition of NPs by the immune system, thus reducing NP clearance by the reticuloendothelial system (RES) and increasing retention times for NPs in blood circulation [17, 18]. It has already become clear that PEGylation density and the PEG spatial configuration have a great impact on its physiological properties. The amount and configuration of grafted PEG play determinant roles in NP colloidal stability, protein adsorption, and cellular internalization [11, 19, 20]. It has also been reported that densely packed, planar, PEGylated surfaces can suppress protein adsorption only in certain configurations [21].

PEG molecules can be linked to NP surfaces either via incorporating PEG chains *in situ* [11, 22] or through covalent attachment to the surface [23- 26]. When PEG polymers are covalently attached to surfaces, their chain entropy becomes the limiting factor for their grafting density. However, the *in situ* approach can enable a tight surface coverage, thereby providing greater efficiency in preventing protein adsorption [27]. Various *in situ* approaches for the synthesis of colloidal NPs in the presence of PEG molecules have been accomplished in previous studies. For instance, Mukhopadhyay *et al.* reported the synthesis of PEG-coated magnetite (Fe_3O_4) NPs to investigate their effect on cytochrome c reduction [28]. Seol *et al.* developed a one-step, microwave-assisted route for the synthesis of PEG-coated gold nanoparticles (GNPs) [29]. Shameli *et al.* facilitated PEG-mediated growth of silver nanoparticles (Ag-NPs) while applying an environmentally friendly approach [30]. Huang *et al.* managed a controllable large-scale synthesis of ultrasmall PEG–ZnO NPs in ethanol [31]. Moreover, Shen *et al.* presented one-pot hydrothermal synthesis of PEG-passivated graphene quantum dots and also studied their photoelectric conversion under near-infrared light [32]. Recently, Yinan *et al.* developed water-soluble Mn^{2+} -doped ZnS nanocrystals with PEG as a surface modifier without a ligand exchange protocol to render the NPs water-soluble [33]. Rao *et al.* introduced simultaneous synthesis and surface functionalization of $\text{BaLuF}_5:\text{Gd}/\text{Yb}/\text{Er}$ upconversion NPs (UCNPs) with PEG ligands as an ideal probe for dual imaging [34]. Despite all these successful synthesis attempts for NPs in the presence of PEG, the effects of PEG molecules on the generation of NPs and their physiochemical properties have not been thoroughly investigated.

In this study, we present a practical and generic approach for the *in situ* introduction of thiol-terminated methoxy PEG (mPEG) groups ($M_n = 800$) to the surface of CdTe/CdS/ZnS Qdots during synthesis of ZnS outer shell, with simultaneous incorporation of surface carboxyl groups for further functionalization. Further, we investigated the effect of mPEG ligands on the physiochemical properties of Qdots in terms of shell growth rate, surface characteristics, and colloidal stability. In our previous report, we established aqueous synthesis of near-infrared emitting CdTe/CdS/ZnS core_(small)/shell_(thick)/shell_(small) Qdots with high quantum yields up to 64%. There, we indicated that ZnS shell deposition virtually minimized Qdot-induced *in vitro* cytotoxicity and increased photostability [35]. Although ZnS is less susceptible to oxidation than CdS, the relatively slow oxidation of ZnS with a concomitant loss of surface sulfur atoms can take place under ambient conditions [36]. This process eventually results in the decomposition of the ZnS shell and brings delayed-release Qdot toxicity issues back into the discussion. Taking this into consideration, we tested the effect of mPEG surface ligands on the cellular toxicity of Qdots as a function of mPEG grafting density by using two-dimensional (2D) monolayer cell cultures and three-dimensional (3D) tumor-like spheroid cultures. Later, we explored cellular binding characteristics of PEGylated and nonPEGylated Qdots with 3D spheroids in order to understand their interactions on physiologically relevant microscale tissue-like structures to predict *in vivo* behavior of Qdots in the sense of cellular binding and uptake. We believe that the result of this study will highlight fundamental parameters that need to be explored in detail to boost the development and safe application of functionalized colloidal NPs in nanobiotechnology.

4.3.4. Results and Discussion

Synthesis of PEGylated CdTe/CdS/ZnS Qdots

Aqueous one-pot synthesis of 3-mercaptopropionic acid (MPA)-functionalized CdTe/CdS/ZnS Qdots with small-core/thick-shell/thin-shell structure was adopted from our previous study [35]. First, CdTe/CdS small-core/thick-shell Qdots emitting at 650–660 nm were synthesized. The crude solution was directly used for deposition of a ZnS shell, and the remaining MPA molecules in the crude solution were utilized as the sulfur source for ZnS formation as well as a surface-coordinating agent. In addition to

MPA, methoxy PEG thiol (mPEGthiol) molecules were introduced to the surface of the outer ZnS shell as a cocoordinating ligand. Thus, CdTe/CdS/ZnS Qdots with a mixture of carboxyl and mPEG surface groups were created. A schematic representation of ZnS shell overgrowth in the presence of MPA and mPEGthiols is depicted in **Figure 1 a**. The amount of mPEGthiol in the reaction solution was adjusted to give a [Zn/mPEGthiol] molar ratio of 1:5 and 1:10. The resulting mPEG-Qdots are respectively referred to as mPEG-Qdot (1:5) and mPEG-Qdot (1:10) elsewhere in the text. During the ZnS shell synthesis, fluorescence emission profiles showed red-shift indicating the deposition of a ZnS shell [35, 37-39]. However, the amount of red-shift declined in the presence of mPEGthiol molecules (**Figure 1 b**), indicating a slower growth of the outer ZnS shell. For mPEG-Qdot (1:5), ZnS shell formation proceeded slightly

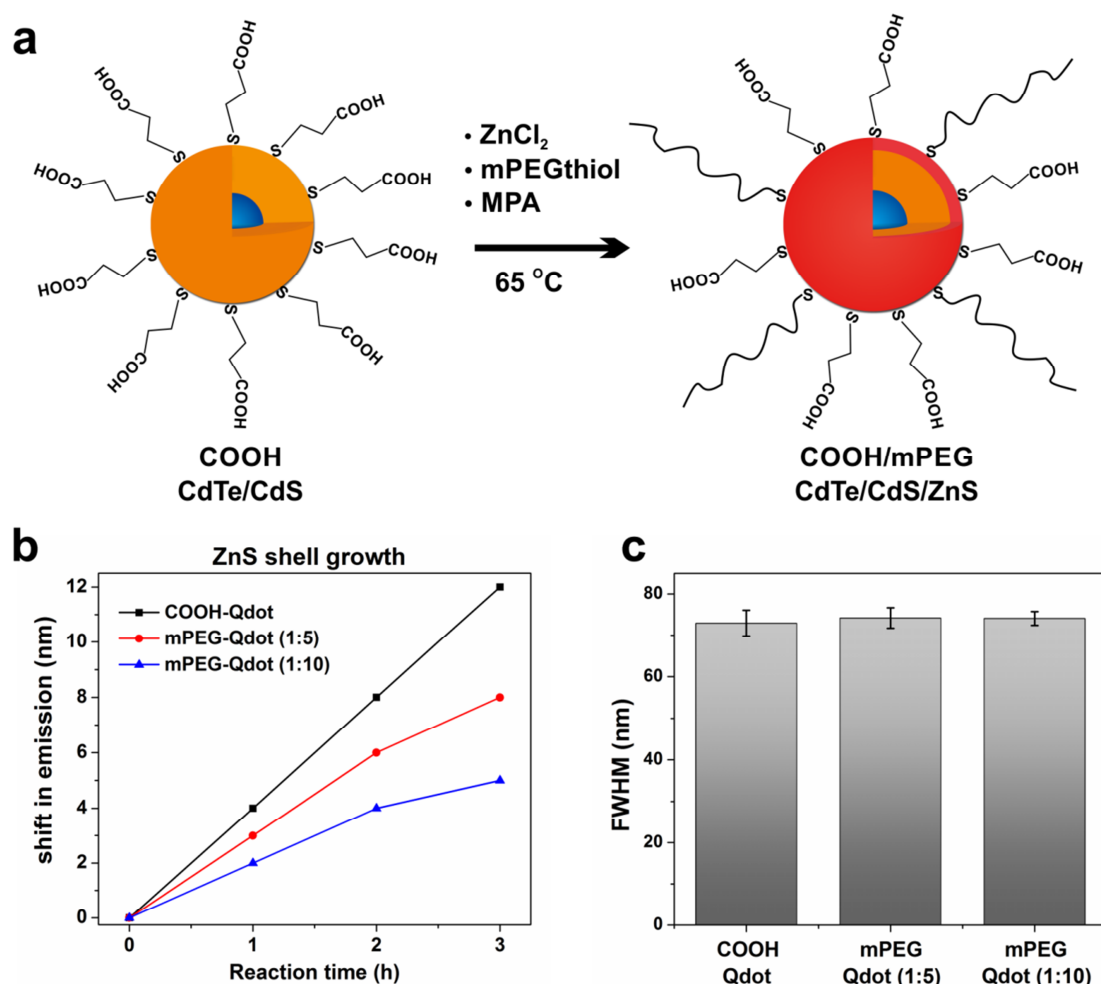


Figure 1. (a) Schematic illustration of PEGylated CdTe/CdS/ZnS Qdots synthesis in aqueous medium; (b) red-shift in emission profiles of Qdots during ZnS shell growth in the presence of mPEGthiols; (c) full-width at half-maximum (fwhm) values for resulting Qdots as an indicator for size variations. 3-Mercaptopropionic acid (MPA), which was used as sulfur source and at the same time as surface passivating ligand, coordinated at outer surface along with thiol-terminated mPEG molecules during ZnS shell growth.

slowly without any effect on Qdot fluorescence efficiency. As the amount of mPEG was increased to 1:10 in the reaction solution, ZnS shell deposition rate decreased drastically, with a subsequent decrease in quantum yields (QY, %) by $3 \pm 1\%$. For the growth of the ZnS shell, sulfur atoms from the Cd-SR on the surface of CdTe/CdS Qdots released their organic group $R = [-(CH_2)_2COOH]$ to bind with Zn^{2+} ions. Unreacted MPA molecules in the crude solution also bound with Zn^{2+} ions to form an outer shell as well as to coordinate on the shell surface [40]. In the meantime, mPEGthiol molecules attached to the ZnS shell surface by means of zinc-thiol binding. In the presence of excess mPEGthiols, the binding of the sulfur atoms of mPEGthiols to the Qdot surface might have taken place at the early stage of ZnS growth. Consequently, they might have hindered formation of Zn-MPA complexes, thus slowing deposition of the ZnS shell. Fluorescence emission peak widths (full-width at half-maximum, fwhm) of the resulting Qdots are given in **Figure 1 c**. COOH-Qdots, mPEG-Qdots (1:5), and mPEG-Qdots (1:10) showed very similar fwhm values at 72.9 ± 3.1 , 74.2 ± 2.5 , and 74.1 ± 1.7 , respectively. The spectral width values indicated that there was no significant difference in Qdot size distributions for the samples. That is to say, the applied PEGylation strategy did not cause a broadening of size distribution; as a result, Qdots preserved their monodispersity.

Characterization Studies

ζ -potential (ζ -Pot) analyses were conducted in order to measure the charge of the Qdots. COOH-Qdots with negatively charged carboxyl groups on their surface had a negative ζ -Pot value of -36.8 mV (**Figure 2 a**). Meanwhile, mPEG-capped Qdots featured reduced ζ potential values due to the partial replacement of carboxyl groups with nonionic mPEG molecules. mPEG-Qdots (1:5) showed ζ -Pot value of -31.1 mV, whereas mPEG-Qdots (1:10) showed -25.9 mV; thus, as the amount of mPEG molecules on nanoparticle surface was increased, the corresponding ζ -Pot value was reduced further. Although we lack the knowledge of the precise number of mPEG molecules attached per Qdot and their orientation on the surface, the ζ -potential analysis clearly indicates that mPEG-Qdot (1:10) conjugates possessed a higher degree of mPEG coating in comparison to mPEG-Qdots (1:5).

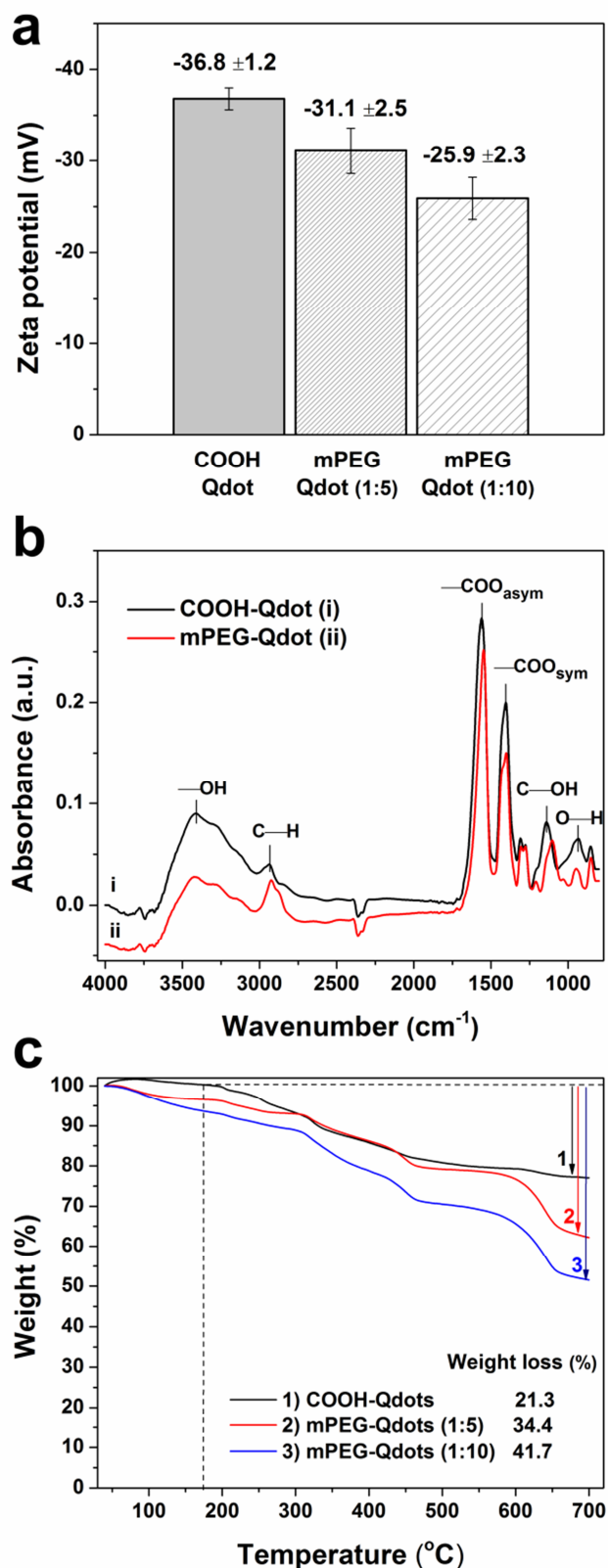


Figure 2. Characterization of COOH⁻ and mPEG-Qdots: (a) ζ -potential analysis; (b) ATR-FTIR spectra of (i) COOH-Qdot and (ii) mPEG-Qdot (1:10) films casted on a ZnSe-ATR crystal in water; (c) TG analysis of COOH-Qdots and mPEG-Qdots. The heating rate was 5 K min^{-1} under an 80% argon and 20% O_2 flow. The vertical line indicates the temperature at which most of the adsorbed water was considered to be evaporated ($175 \text{ }^\circ\text{C}$).

Attenuated total reflection Fourier transform infrared (ATR-FTIR) spectroscopy results for COOH-Qdots and mPEG-Qdots (1:10) are given in **Figure 2 b**. In general, vibration frequencies exhibited slight shifts for mPEG-Qdots in comparison to COOH-Qdots. According to the spectra, symmetric and asymmetric -COO stretching bands for COOH-Qdots were observed at 1404 and 1560 cm^{-1} , respectively [41], while for mPEG-Qdots they were shifted to 1402 and 1549 cm^{-1} with a concomitant decrease in their intensity. The O-H stretching bands (3412 cm^{-1}) and C-OH stretching peak (1140 cm^{-1}) for COOH-Qdots appeared at 3425 cm^{-1} and 1103 cm^{-1} respectively for mPEG-Qdots, and both experienced a decrease in their intensity. At the same time, the -OH bending peak for carboxylic acids (933 cm^{-1}) was shifted to 947 cm^{-1} for mPEG-Qdots, with a significant decrease in its intensity. These decreases can be attributed to partial replacement of COOH groups with mPEG molecules. Moreover, C-H stretching peak of alkyl group (2937 cm^{-1}) for COOH-Qdot was moved to 2924 cm^{-1} for mPEG-Qdot with a significant increase in its intensity. This increase can be attributed to the presence of terminal methyl groups (-CH_3) and -CH_2 groups of PEG backbone.

Thermogravimetric (TG) analysis was conducted to estimate the amount of mPEG molecules on the surface of Qdots. As shown in **Figure 2 c**, COOH- and mPEG-Qdots displayed different amounts of weight loss between 175 and 680 $^{\circ}\text{C}$ with respect to their surface ligand structure. The drop in all TG curves until 175 $^{\circ}\text{C}$ was attributed to the decomposition of adsorbed water. Between 175 and 525 $^{\circ}\text{C}$ all Qdot samples exhibited a similar mass-loss profile which was assigned to the gradual decomposition of MPA ligands from the surface of the Qdots [42]. The decomposition temperature of MPA, which is higher than the boiling point of pure MPA (157 $^{\circ}\text{C}$), demonstrates covalent bonding between MPA and the Qdot surface [43]. Meanwhile, mPEG-Qdots displayed a distinguishable weight loss at higher temperatures between 500 and 680 $^{\circ}\text{C}$ which was related to the degradation of mPEG molecules. In addition to that, the drop between 300 and 525 $^{\circ}\text{C}$ was found to be pronounced for mPEG-Qdots in comparison to COOH-Qdots, suggesting that decomposition of mPEG molecules had already started at low temperatures, which is in agreement with previous reports [44-46]. Regarding the organic capping materials, COOH-Qdots exhibited a weight loss of 21.3% whereas mPEG-Qdots (1:5) and mPEG-Qdots (1:10) showed a 34.4% and

41.7% weight loss, respectively. The increase in the amount of weight loss for the PEGylated Qdots corresponds to an increase in the amount of mPEG molecules on the surface of the Qdots. The corresponding mPEG amounts are approximately 13.1% and 20.4% for mPEG–Qdots (1:5) and mPEG–Qdots (1:10), respectively, suggesting that mPEG–Qdots (1:10) acquire 27% excess mPEG molecules in comparison to mPEG–Qdots (1:5). As a conclusion, these results indicate successful attachment of mPEG groups to the Qdot surfaces during ZnS shell synthesis.

Colloidal Stability

Ligand molecules on Qdot surfaces play an important role on colloidal stability of NPs by influencing their nanoenvironments [4]. 3-Mercaptopropionic acid (MPA), the main surface coordinating ligand for Qdots used in this study, plays a major role that determines the colloidal stability of Qdots. When Qdots are dispersed in pure water, carboxyl groups of MPA become negatively charged, since in pure water pH (7.0) \gg pK_{COOH} (4.32) [47]. As a result, the NP surface becomes saturated with negatively charged ($-\text{COO}^-$) groups and the NPs become colloidally stable due to the electrostatic repulsion between negative charges. In addition to electrostatic repulsion, NPs can also be stabilized via steric repulsion originating from macromolecular ligands, such as PEG [4].

Herein, we studied the colloidal stability of carboxylated and PEGylated Qdots in order to examine the cooperative influence of neutral mPEG molecules on Qdot stability. As is known, aggregation of Qdots in aqueous solution results in a red-shift in emission profiles with a subsequent decrease in their fluorescence intensity [31, 47, 48]. Considering this, changes in emission wavelength positions for respective Qdots upon their incubation in different aqueous media at different temperatures were established as an indicator of their colloidal stability. For that, diluted Qdots solutions ($\leq 1\text{mg mL}^{-1}$) were prepared in pure water, serum-free culture medium, and 10% serum-containing medium and incubated at 4 and 37 °C. The obtained results are depicted in **Figure 3**. Accordingly, both COOH–Qdots and mPEG–Qdots showed different levels of stability with regard to their mPEG content. As a general observation, COOH–Qdots showed a greater tendency for aggregation in all aqueous media tested in comparison to their PEGylated counterparts, and a high incubation temperature induced faster Qdot agglomeration. As a result, the red-shift in COOH–Qdots emission reached a plateau

earlier. In pure water, protonation of the thiol ligands of MPA may lead to an ultimate loss of surface agents [49]. The diluted Qdot concentration plays a major role in the irreversible loss of MPA due to the impaired dynamic equilibrium of detaching and rebinding of MPA [50]. Once the surface capping agent is detached from the surface, electrostatic repulsion forces become insufficient to ensure the stabilization of Qdots; in addition to that, free inorganic surface energy rises and in turn triggers interparticle attractions by van der Waals forces. This mechanism might be one of the main causes of the loss of colloidal stability in thiol-capped Qdots. Incorporation of neutral mPEG polymers to the Qdot surface facilitated a significant improvement in overall colloidal stability by introducing a steric barrier to prevent interparticle interaction. When compared to other Qdots, mPEG–Qdots (1:10) possessing the highest surface PEG amount had the highest colloidal stability. Increased grafting density might have provided a more stable brush layer through coordination of the thiol functional group with Zn^{2+} ions during ZnS shell growth. In serum-free culture medium, the presence of salt cations (e.g., Na^+ and Ca^{2+}) expedited aggregation of all Qdots, especially that of carboxyl-capped Qdots. The underlying reason is that the negative surface charges of

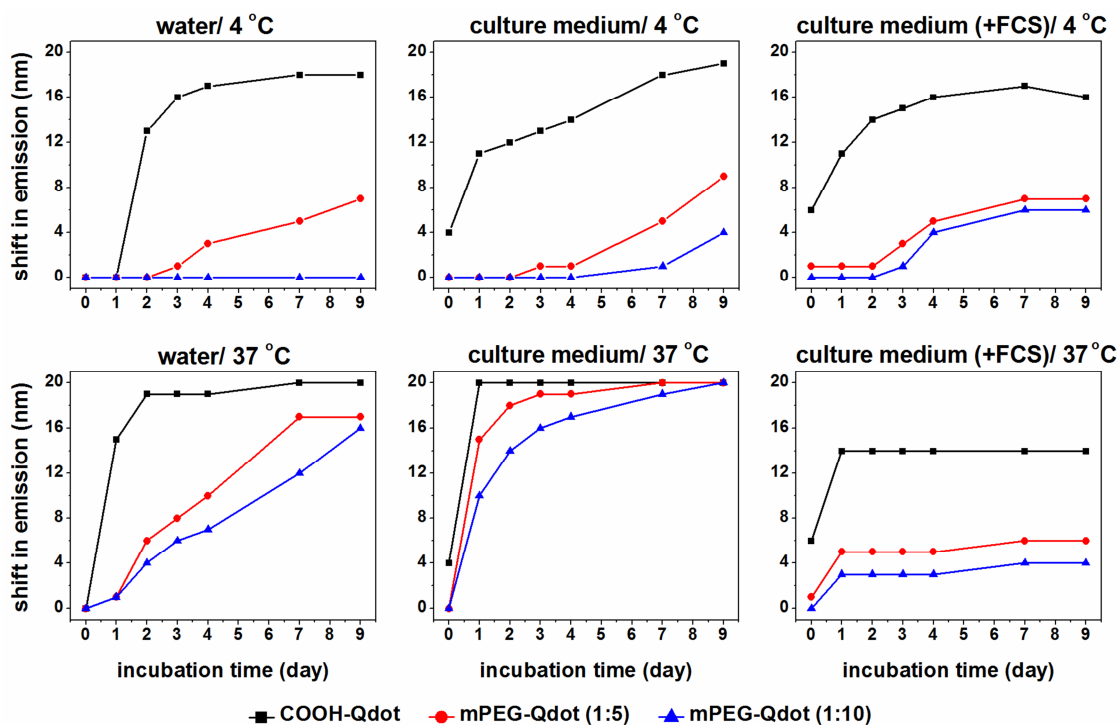


Figure 3. Structural stability of COOH–Qdots and mPEG–Qdots in water, DMEM cell culture medium with/without 10% fetal calf serum (FCS) at 4 and 37 °C. Graphics show red-shift in Qdots emission wavelengths versus incubation time in given aqueous media. The aggregation induced red-shift in Qdot emission shows different profiles regarding the mPEG content.

carboxyl groups are screened by the absorption of counterions from culture medium. Due to the screening effect, electrostatic repulsive forces were reduced. As a result, interparticle accumulation became favorable [50]. In serum-containing culture medium, all Qdots emissions exhibited smaller red-shifts in comparison to serum-free medium conditions, implying relatively higher colloidal stability in serum-containing medium. This can be accounted for by the formation of protein corona structures in the presence of serum proteins [9, 50]. Adsorption of a protein layer on colloidal NP surfaces has proven to improve the stability of NPs against agglomeration [51]. The degree of protein corona formation is closely related to the physiochemical properties of nanoparticles (e.g., size, charge, surface chemistry, colloidal stability) [3]. In the presence of serum proteins, formation of a protein corona should predominate Qdot agglomeration rather than interparticle attractions alone. In serum-containing medium at 4 °C, Qdots reached a plateau later than at 37 °C, suggesting that adsorption of proteins displayed a marked temperature dependency, and the temperature effects were pronounced at the physiologically relevant temperature at 37 °C. At physiological temperatures, structural fluctuations of proteins and/or polymer shells around Qdots might induce conformational arrangements which in turn might affect the binding affinity of proteins to the Qdot surface [52]. Therefore, the decreased agglomeration behavior for Qdots in serum-containing medium at 37 °C could be accounted for by a higher degree of protein adsorption to Qdot surfaces than at 4 °C. Overall, the obtained results proved that higher amount of mPEG molecules on the surface of ZnS shell enhanced colloidal stability of Qdots via steric repulsion effects to a great extent.

Effect of mPEG on Protein Adsorption

The influence of PEGylation on protein adsorption was further investigated by protein interaction analysis using bovine serum albumin (BSA) as a model protein prevalent in serum. We expect that mPEG–Qdots should possess a reduced degree of protein binding and thus a decreased protein corona formation. In order to prove this assumption, microscale thermophoresis (MST) analysis of Qdots and BSA was performed, and equilibrium dissociation constants determined for COOH– and mPEG–Qdots are given in **Figure 4** [53].

Hill model was used to extract quantitative data about binding affinity of BSA to the surface of Qdots with regard to their mPEG content [50, 51, 54].

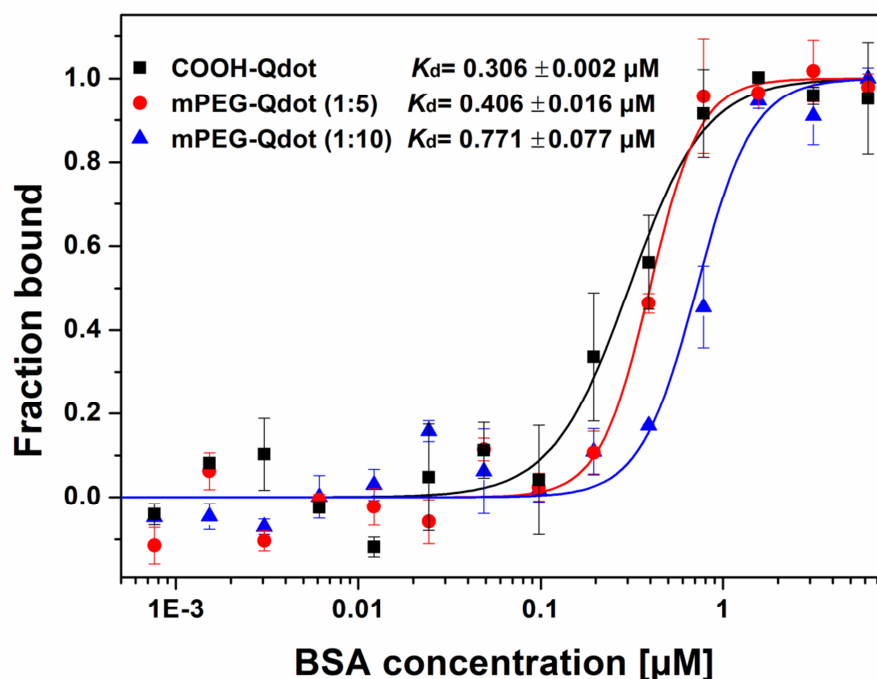


Figure 4. Determination of the dissociation constants of Qdots–BSA interactions by MST analysis. K_d values were calculated by fitting experimental data with Hill equation. Samples were excited at 470 nm with an excitation power of 10%, and thermophoresis analyses were conducted at room temperature with a 40% MST power. The error bars represent the standard deviation of at least two independent MST measurements.

By fitting experimental data with Hill equation, we obtained apparent equilibrium dissociation coefficient K_d values (concentration of protein at half saturation) of $K_d = 0.306 \pm 0.002 \mu\text{M}$ for COOH–Qdots, $K_d = 0.406 \pm 0.016 \mu\text{M}$ for mPEG–Qdots (1:5), and $K_d = 0.771 \pm 0.077 \mu\text{M}$ for mPEG–Qdots (1:10). Accordingly, binding affinities were found to decrease for Qdots in the following order: COOH–Qdots > mPEG–Qdots (1:5) > mPEG–Qdots (1:10). These results indirectly prove a higher amount of grafted mPEG for mPEG–Qdots (1:10) than that of mPEG–Qdots (1:5) and indicate that an increase in the mPEG amount caused a further decrease in the interactions of the Qdots with BSA proteins, confirming our expectation. The Hill coefficients were also determined to interpret the degree of cooperativity in protein binding to the surface of the Qdots. The Hill fit yielded a Hill coefficient of $n = 2.0 \pm 0.1$ for COOH–Qdots, $n = 3.1 \pm 0.7$ for mPEG–Qdots (1:5), and $n = 2.6 \pm 0.3$ for mPEG–Qdots (1:10), indicating a cooperative binding behavior ($n \geq 1$) for all Qdots. That is to say, the proteins bound on the Qdots surfaces influenced the adsorption of further proteins from the solution. The cooperative adsorption of proteins to NP surfaces has been reported before and was

attributed to stabilizing interactions between adjacent protein molecules that may contribute to formation of protein corona [51, 55].

Evaluation of in Vitro Cytotoxicity

The rapid emergence of quantum dots as highly efficient biological imaging agents brought along safety concerns related to their metal-containing compositions [56]. NP-induced toxicity is mostly ascribed to *in situ* NP degradation which is followed by release of metal ions (e.g., Cd^{2+} , Ag^+ , Pb^{2+} , In^{3+} , As^{3-} , Hg^{2+} , Au^+) to the intracellular environment. After their internalization, NPs are entrapped in endocytic vesicles and undergo a surface etching process under acidic conditions in lysosomes, which results in irreversible destruction of their photochemical properties [57-59]. NP-induced toxicity exhibits a direct relation to their material composition, size, surface chemistry, and colloidal stability. In our previous study, we addressed size and composition-dependent adverse effects of COOH-CdTe/CdS and COOH-CdTe/CdS/ZnS Qdots on monolayer cultures of A549 human lung adenocarcinoma cells [35]. The results demonstrated that deposition of an outer ZnS shell mitigated the toxic effects of Qdots by providing effective surface passivation. Herein, we aim to address the subsequent effect of mPEG molecules grafted to ZnS shell surfaces on Qdot-induced toxicity as a function of mPEG density. Additionally, 3D tumor-like spheroid cultures of A549 cells were utilized in order to assess physiologically relevant cytotoxicity effects of PEGylated Qdots. Spheroid cell cultures are a relatively simple technique of 3D cell cultures that takes advantage of the natural tendency of cells to aggregate [60]. They provide a more accurate *in vitro* model, since they closely resemble *in vivo* tissue structures in terms of intercellular communication, extracellular matrix development, and complex diffusion/transport mechanisms in comparison to 2D monolayer cell cultures. For that reason, the utilization of 3D cell culture models holds great potential to produce more physiologically relevant data for NP-based studies [61-64]. The cell viability results obtained from CTB assay are given in **Figure 5**. In 2D monolayer cultures, PEGylated Qdots exhibited significantly reduced toxicity in comparison to carboxylated Qdots (**Figure 5 a**). Half-maximal inhibitory concentrations (IC_{50}) were calculated to be $152.1 \pm 21.4 \mu\text{g mL}^{-1}$ for COOH-Qdots and $282.9 \pm 26.4 \mu\text{g mL}^{-1}$ for mPEG-Qdots (1:5), thus meaning $\sim 86\%$ decrease in cellular toxicity upon

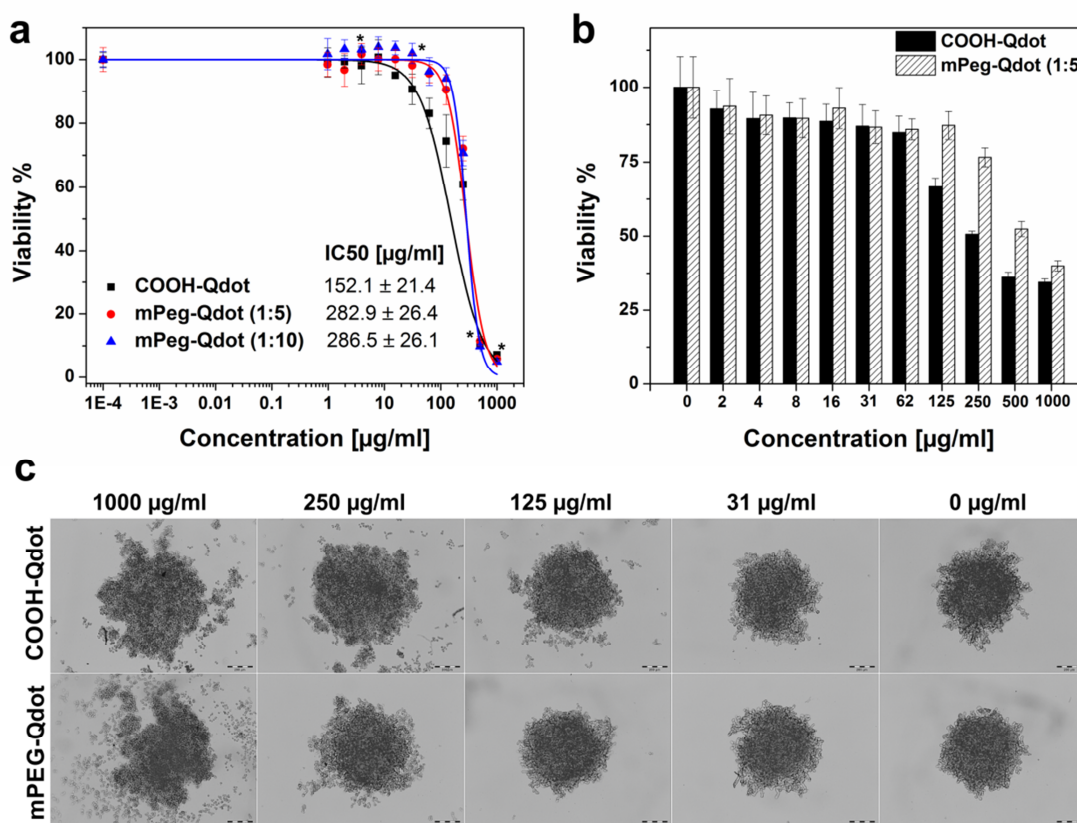


Figure 5. (a) Dose-dependent *in vitro* cytotoxicity of COOH-Qdots and mPEG-Qdots on A549 cell lines; (b) cell viability data obtained from CTB assay for 2D cell cultures; (c) bright-field microscope images of A549 tumor-like spheroids exposed to COOH- and mPEG-Qdots (1:5) with a concentration range of 0.002-1000 $\mu\text{g mL}^{-1}$ for 24 h. Data points are given as mean \pm standard error of 3 ± 1 independent experiments of which each was conducted with four replicates. Inset data in (a) show half-maximal inhibitory concentrations (IC₅₀) in $\mu\text{g mL}^{-1}$. The asterisk (*) indicates significant difference at 0.01 level. $p < \alpha = 0.01$ (ANOVA one-way). Scale bars in (c) are 200 μm .

incorporation of mPEG molecules to Qdot surface. On the one hand, mPEG-Qdots (1:10) possessing more mPEG molecules resulted an IC₅₀ value of $286.5 \pm 26.4 \mu\text{g mL}^{-1}$ which is very close to that of mPEG-Qdots (1:5).

For 3D tumor-like spheroid cultures, all Qdot samples tested demonstrated reduced toxicity levels for the applied Qdot doses in comparison to 2D cultures (**Figure 5 b**). PEGylation of Qdots mitigated dose-dependent adverse effects on 3D spheroids, agreeing with the cell viability results obtained from 2D cultures. Also, increased mPEG quantities on Qdot surface did not lead to any further improvement on Qdots toxicity (data not shown). According to the bright-field images of spheroids shown in **Figure 5 c**, Qdots induced apparent effects to the morphology of tumor spheroids in a concentration-dependent manner. Low Qdot concentrations ($<61 \mu\text{g mL}^{-1}$ for COOH-Qdot, and $<125 \mu\text{g mL}^{-1}$ for mPEG-Qdots) did not alter the overall

morphology of spheroids in comparison to control samples, while higher Qdot doses caused a rough surface formation due to protruding granular shaped cells. As the Qdot concentration was increased to $1000 \mu\text{g mL}^{-1}$, the formation of round cells became pronounced, and some cell aggregates detached from the spheroid surface.

On the basis of these observations, we can clearly state that the addition of mPEG molecules to Qdot surfaces minimized the negative effects of Qdots by improving their colloidal stability. On the other hand, in contrast to that which one might expect, increased amounts of mPEG molecules did not ameliorate the toxicity-related effects of Qdots. In the previous section, we mentioned that the increased amount of mPEGthiol in the reaction solution decelerated the deposition rate of the ZnS shell during the given reaction time, which in turn resulted in formation of a relatively thin ZnS shell. The inert nature of the ZnS shell provided a strong electronic barrier to electron–hole delocalization toward particle surface ensuring efficient passivation of surface trap sites [65, 66]. Hence, insufficient growth of ZnS shells may have an influence on overall Qdot-induced toxicity. Nevertheless, despite the restricting effect of mPEGthiol molecules on formation of a well-passivated ZnS shell, the improved colloidal stability of Qdots predominantly prevented aggravation of Qdot toxicity. On 3D spheroids, the general decrease in Qdot-induced toxicity in comparison to 2D cultures can be explained by the presence of a physical barrier arising from extracellular matrix (ECM), which is produced by the cells during the spheroidal growth [67]. This barrier can hinder NP accumulations and limit their transport toward the spheroid inner region. Such physical limitations are not as pronounced in 2D monolayer cultures as they are in 3D models [68]. Supporting our findings, conventional monolayer cell cultures were also reported to be more sensitive to NPs or drug molecules in comparison to various 3D cell culture systems in previous studies [63, 64, 69-71].

Nonspecific Cellular Binding

Nonspecific binding features of COOH–Qdots and mPEG–Qdots with A549 cells were analyzed by using flow cytometry measurements. Fluorescence intensities were obtained from cells that had been incubated with Qdots (**Figure 6**). Consequently, COOH–Qdots and mPEG–Qdots (1:5) showed stronger binding in comparison to mPEG–Qdots (1:10). The fluorescence intensities for mPEG–Qdots (1:10) reduced by 63%, indicating decreased nonspecific cellular interactions due to the presence of

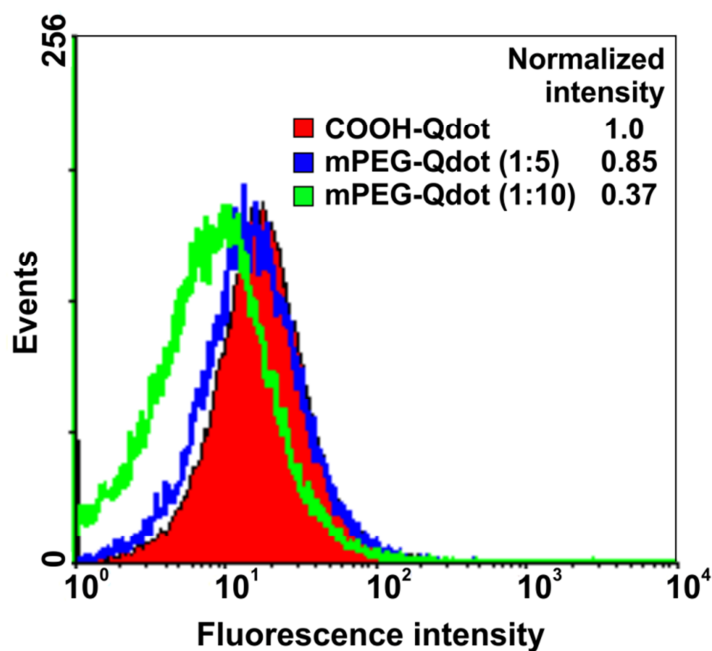


Figure 6. Logarithmic flow cytometry histograms for the A549 cells stained with $100 \mu\text{g mL}^{-1}$ COOH-Qdots and mPEG-Qdots for 30 min. Samples were excited at 488 nm, and minimum 30,000 gated events were acquired for later analyses. The binding effect was defined as the ratio between the normalized fluorescence intensity of cells incubated with COOH-Qdots and mPEG-Qdots.

increased mPEG packing density. Apparently, a higher PEGylation density resulted in a reduced cell binding within the given experimental parameters, agreeing with the previous studies [11, 72]. On the other hand, the reduced mPEG surface density for mPEG-Qdots (1:5) did not show significant nonspecific binding. It was previously reported that the grafting density has a major impact on resistance to protein adsorption for surface mPEG molecules [27, 73]. Accordingly, a tight surface coverage was found to be very efficient to prevent protein adsorption to NP surfaces, resulting in a reduced uptake [11, 12]. Considering these observations, we can assume that the surface PEG density in the case of mPEG-Qdots (1:5) was not sufficient to provide the optimal protein-repelling coating to reduce NP-cell interactions.

Labelling Tumor-like Spheroids with mPEG-Qdots

Evaluation of unmodified Qdot interactions prior to their modification with a targeting moiety for target-specific bioapplication is a prerequisite to understand their respective binding mechanisms on cellular levels. These interactions are dominated by inherent physical properties of Qdots, e.g., size, composition, surface chemistry, and charge.

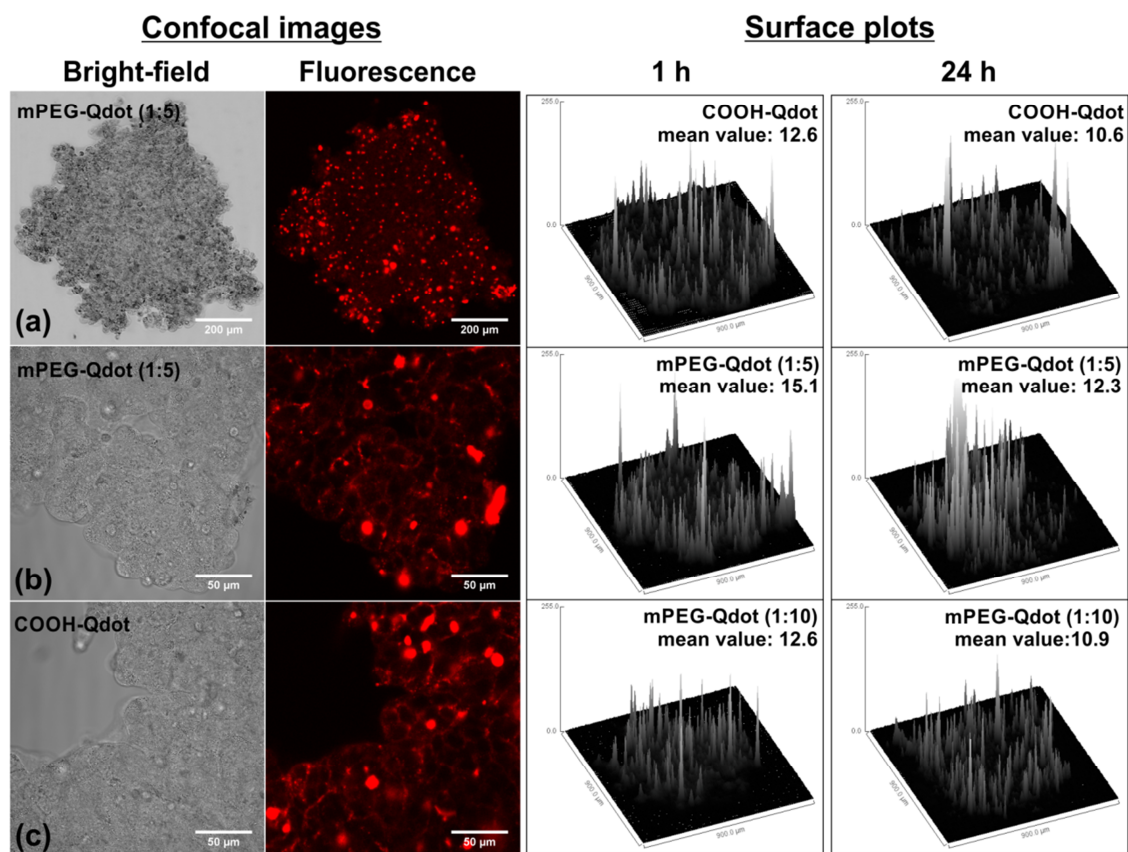


Figure 7. Cellular interactions of COOH- and mPEG-Qdots with A549 tumor-like spheroids. Left column shows confocal microscope images of tumor spheroids treated with COOH- and mPEG-Qdot (1:5) for 1 h. Fluorescence images for mPEG-Qdots (1:5) were captured with 10x (a) and 40x (b) for COOH-Qdots with 40x objectives (c) by applying 488 nm excitation laser (argon/2). Images for mPEG-Qdot (1:10) are not given since they showed very similar cellular binding. Right-column shows surface plot profiles of spheroids treated with COOH- and mPEG-Qdots for 1 and 24 h. (x, y) = (900, 900) μm . Mean fluorescence intensity values given in insets were measured after applying equal background subtraction to all images (ImageJ). Scale bar is 200 μm for (a) and 50 μm for (b) and (c).

Herein, the effect of neutral mPEG molecules on cellular binding features of Qdots was investigated by using *in vitro* 3D A549 tumor-like spheroids, as they create a physiologically relevant microenvironment for cellular assays. Confocal microscope images of tumor spheroids treated with either carboxylated or PEGylated Qdots for 1 and 24 h as well as their corresponding surface plot profiles and mean intensity values measured by image processing and analysis (ImageJ) are given in **Figure 7**. In general, there was no pronounced difference between COOH- and mPEG-modified Qdots in the sense of a cellular binding mechanism after 1 h of incubation. In the magnified images, it can be clearly seen that both COOH- and mPEG-Qdots accumulated at the cell membranes within the given incubation time. Agglomerated Qdots were also detected on the spheroid surfaces, especially for COOH-Qdots. From the surface plot and intensity analysis, slightly enhanced binding of mPEG-Qdots (1:5) to the cell

membrane compared to COOH- and mPEG-Qdots (1:10) was observed. One reason for that could be decreasing electrostatic repulsion between the Qdots and the negatively charged cell membrane promoting cellular binding [74]. In such a case, an enhanced binding should also have been observed for mPEG-Qdots (1:10), which is not the case in our observations. With regard to the colloidal stability results, we should note that COOH-Qdots lost 27% of their initial fluorescence intensity upon their transfer to serum-containing culture medium, and this value reached 33% when they were incubated for 24 h at 37 °C in cell culture conditions. mPEG-Qdots (1:5) and mPEG-Qdots (1:10), on the other hand, showed only 16% and 5% intensity loss, respectively, upon their incubation at 37 °C for 24 h in cell culture conditions. Therefore, it is more likely that the reduced fluorescence intensity for COOH-Qdots does not originate from minimized cellular binding but rather from diminished fluorescence intensity upon incubation at 37 °C in serum-containing medium. Notably, mPEG-Qdots (1:10) exhibited minimal binding to the cells in spheroid structure and displayed a more uniform binding distribution.

After 24 h of incubation, there was an apparent internalization for COOH-Qdots and mPEG-Qdots (1:5), mostly by the cells residing on the outer spheroid region, and their fluorescence intensities clearly decreased toward the spheroid inner regions, with a parallel increase in their agglomeration behavior (**Figure S1, Supporting Information**) whereas mPEG-Qdots (1:10) preserved their uniform binding with a minimal decrease in their intensity. This effect can be accounted for by the improved colloidal stability of mPEG-Qdots (1:10) in physiologically relevant culture conditions due to their increased surface mPEG density that facilitates effective steric hindrances. According to the confocal images, mPEG-Qdots (1:10) generally remained attached to the cell membranes, but there was also partial internalization by outer cells. We can assume that mPEG-Qdot (1:10), which has the highest mPEG density, might have relatively slow adsorption and uptake rates in comparison to their lesser- or non-PEGylated counterparts. Adsorption of NPs to cell membranes is reported to be the rate-limiting step, and adsorption rates, in combination with the number of NPs present on the cell membrane, determine the internalization of NPs [9, 75]. In accordance with other findings, mPEG molecules mitigate NP binding to cell surface due to their lower adsorption rates in comparison to their nonPEGylated counterparts [76]. Nevertheless,

we should note that these statements hold only for spatial scales that can be resolved by confocal microscopy.

4.3.5. Conclusion

In the current study, we introduced *in situ* attachment of thiol-terminated mPEG molecules on the Qdot surface during deposition of the ZnS outer shell. The applied synthetic approach enabled functionalization of Qdot surfaces with MPA molecules and simultaneous formation of a stable mPEG brush layer for preservation of colloidal stability. The presence of mPEG molecules in the reaction solution caused slower deposition of ZnS shell while maintaining fluorescence efficiency and monodispersity of Qdots. Surface mPEG ligands with respect to their grafting amount also enhanced colloidal stability and Qdot-induced cytotoxicity issues to a great extent. The resulting mPEG–Qdots (1:10) with a higher mPEG surface density demonstrated distinguished cellular binding features with 2D and 3D tumor-like spheroid cultures. The result of the study will contribute to the development of further strategies to enhance physiochemical properties of PEG-coupled colloidal NPs and their application in novel imaging techniques.

4.3.6. Materials and Methods

Materials: Cadmium chloride hemi(pentahydrate) ($\text{CdCl}_2 \cdot 2^{1/2}\text{H}_2\text{O}$, 98%>), sodium tellurite (Na_2TeO_3 , 99.5%), zinc chloride anhydrous (ZnCl_2 , 99.99%), 3-mercaptopropionic acid (MPA, 99%), sodium borohydride (NaBH_4 , >99.8%), trisodium citrate dehydrate ($\text{HOC}(\text{COONa})(\text{CH}_2\text{COONa})_2 \cdot 2\text{H}_2\text{O}$), polyethylene glycol methyl ether thiol (mPEGthiol, average $M_n = 800$), 4',6-diamidino-2-phenylindole dihydrochloride (DAPI), Calcein-AM (BioReagent, $\geq 96.0\%$), and bovine serum albumin (BSA, heat shock fraction, pH 7, $\geq 98\%$) were purchased from Sigma-Aldrich GmbH, Munich. CellTiter-Blue cell viability assay kit was purchased from Promega Corp., USA.

For cell culture experiments, Dulbecco's modified Eagle medium (DMEM, Sigma- Aldrich GmbH, Munich) supplemented with 10% (v/v) fetal calf serum (FCS, Biochrom GmbH, Germany) and 1% (v/v) penicillin/streptomycin (P/S, Biochrom GmbH, Germany) was used as cell culture medium. For 2D cell

cultures, 96-well flat bottom standard plates (Sarstedt AG&Co. Germany) were used. For 3D spheroid cultures, 96-well round bottom plates coated with ultralow attachment surface (Corning Inc., USA) were used. For fluorescence and confocal microscopy, μ -slide eight-well glass bottom microscopy chambers were provided from ibidi GmbH, Germany.

Synthesis of MPA-CdTe/CdS Qdots: MPA-functionalized CdTe/CdS/ZnS Qdots were synthesized as described previously [35]. First, CdTe/CdS Qdot having a core_(small)/shell_(thick) structure was synthesized as follows: 21 mL of deionized H₂O, 28.5 mg of CdCl₂ dissolved in 1 mL H₂O (125 mM), 18.5 μ L of 3-mercaptopropionic acid (11.5 M), 12.5 mg of trisodium citrate dihydrate dissolved in 1 mL H₂O (42.5 mM), 1.1 mg of sodium tellurite dissolved in 1 mL H₂O (5 mM), and 5 mg of sodium borohydride dissolved in 1 mL H₂O (125 mM) were added sequentially into a three-neck round-bottom flask. The molar ratio of Cd/Te/MPA was set to be 1/0.04/1.7. Under mixing, the solution pH was adjusted to 11.4 with 1 M NaOH. The reaction solution was then refluxed with an air condenser (Findenser, Radleys, U.K.) at 90 °C. When the emission wavelength of CdTe/CdS Qdot reached 655 ± 5 nm, the nanoparticle growth was stopped by simply cooling the reaction temperature to 4 °C. The crude CdTe/CdS solution was directly used as the seed solution for the synthesis of outer ZnS shell in the presence of MPA and mPEGthiol.

Deposition of ZnS Shell with mPEGthiol as Capping Agent: Amounts of 12 mL of the CdTe/CdS crude solution, 11 mL of deionized H₂O, 0.85 mg of ZnCl₂ dissolved in 1 mL H₂O (25 mM) and 1 mL of mPEGthiol solution (125 or 250 mM) were added together giving a final volume of 25 mL. The molar ratio of [Zn/mPEGthiol] was adjusted to either 1:5 or 1:10. The pH of the reaction solution was adjusted to 11.5 with 1 M NaOH. The solution was heated slowly to 65 °C and the ZnS shell growth proceeded for 3 h, yielding in MPA/mPEG-functionalized CdTe/CdS/ZnS core_(small)/shell_(thick)/shell_(small) Qdot ($\lambda_{\text{emission}} = 670 \pm 5$ nm, $QY_{\text{max}} \approx 64\%$). The resulting Qdot sample is referred to as “mPEG-Qdot” in the text. As a control sample, CdTe/CdS/ZnS Qdots functionalized only with MPA were synthesized by following the same procedure excluding the addition of mPEGthiol, and the sample is referred to as “COOH-Qdot” in the text. After synthesis, samples were precipitated with 2-propanol and collected via centrifugation. The colloidal precipitate was weighed after

drying under vacuum and redissolved in pure water. For storage, the Qdot solution was washed with deionized H₂O using 10 kDa MWCO PES membrane filters (Vivaspin, Sartorius Stedim Biotech GmbH, Germany) and kept at 4 °C. For cell culture studies, Qdots solutions were prepared with culture medium and sterilized with 0.2 µm pore-sized high-flow syringe filters (Sartorius Stedim Biotech GmbH, Germany) before application.

Characterization Studies: Fluorescence emissions of Qdot samples were measured with Nanodrop 3300 fluorospectrometer (Thermo Fisher Scientific Inc.USA). Zeta potential analyses were performed with 1mg mL⁻¹ samples in aqueous solutions under ambient conditions with Zetasizer Nano (Malvern Instruments Ltd. U.K.). Attenuated total reflection Fourier transform infrared (ATR-FTIR) spectroscopy analyses were conducted with a BOMEM MB122 instrument equipped with a liquid N₂-cooled MTC-A (mercury–tellurium–cadmium) detector and a Pike Technologies horizontal ATR unit equipped with a trapezoidal ZnSe ATR crystal. A background signal was recorded for uncoated ZnSe crystal surface, and then FTIR spectra were collected for Qdots films (2 mg mL⁻¹) casted on ZnSe crystal surface. Thermogravimetric (TG) analyses for powder Qdot samples (~ 5 mg) were performed using a STA 409 PC/PG apparatus (Netzsch, Germany) under 80% argon and 20% O₂ flow (flow rate: 100 mL min⁻¹) with a heating rate of 5K min⁻¹.

Stability Test: To test colloidal stability of Qdots, 1 mg mL⁻¹ of Qdots solutions (250 µL) were prepared in pure water, DMEM culture medium, and DMEM culture medium supplemented with 10% FCS. Samples prepared in each medium were incubated at 4 and 37 °C to study the effect of temperature on colloidal stability. Emission wavelengths of each sample were recorded at every 24 h for 9 days.

Microscale Thermophoresis (MST) Analysis: The equilibrium dissociation constants (K_d) of Qdot–BSA interactions were measured via MST analysis. Qdot concentration was kept constant at 100 µg mL⁻¹ and the concentration of BSA was varied from 0.013 µg mL⁻¹ to 412.5 µg mL⁻¹. After the samples were incubated at room temperature for 5 min, they were loaded to standard treated glass capillaries (NanoTemper Technologies GmbH, Munich, Germany) for MST measurements. The experiments were performed with a Monolith NT.115 MO-G008 (NanoTemper Technologies GmbH, Munich, Germany) using 40% MST power, and the samples were excited at 470 nm with 10%

excitation power. NT Analysis software (NanoTemper Technologies GmbH, Munich, Germany) was utilized for fitting the curves by using Hill model to determine the K_d values.

Cytotoxicity Studies: For the *in vitro* cytotoxicity studies, human lung adenocarcinoma A549 cell line (ACC107) purchased from DSMZ (German Collection of Microorganism and Cell Cultures) was used with a passage number of less than 20. For assessment of cytotoxicity on 2D cultures, 8000 cells in 100 μ L of culture medium (DMEM supplemented with 10% FCS and 1% P/S) were seeded to 96-well flat bottom standard plates and incubated for 2 days at 37 °C, 5% CO₂. Qdot dilution series were prepared with cell culture medium containing supplements. An amount of 100 μ L of culture medium was replaced with Qdot-containing medium, and cells were incubated for the next 24 h. A control group was treated with fresh culture medium without Qdots. For utilization of 3D spheroid cultures, 6000 cells in 100 μ L of culture medium were seeded to 96-well round-bottom spheroid plates and incubated for 2 days for spheroid formation. Afterward, 50 μ L of culture medium was replaced with 50 μ L Qdot solution freshly prepared with culture medium and incubated further for another 24 h. The metabolic activity of viable cells in terms of their reduction capacity of resazurin was measured via CTB assay kit (Promega Corp., USA). For 2D cell culture, culture medium was removed gently, and 100 μ L of CTB reagent (diluted 1:6 with supplement-free DMEM medium) was added to each well and incubated for 1–2 h (37 °C, 5% CO₂). For 3D spheroid cultures, 20 μ L of CTB stock reagent was directly added to 100 μ L Qdot-containing culture medium 5 h after Qdot introduction (giving a final dilution of 1:6) and incubated for another 19 h at 37 °C, 5% CO₂. The resulting fluorescence intensities originated from release of resorufin dye were recorded at 544_{Ex}/590_{Em} with fluorescence spectrometer (Fluoroskan Ascent, Thermo Fischer Scientific Inc. USA).

Statistical Analysis: Concentration-dependent normalized cell viability data obtained from CTB assay were fitted from 0 to 100 by using nonlinear curve fitting/growth/sigmoidal/dose–response fitting functions (OriginPro 8.6.0 b70, OriginLab Corp., USA). Half-maximal inhibitory concentrations (IC₅₀) were calculated from the fitted dose–response curves. The shown data are from at least two independent experiments, and all individual experiments were conducted with four

replicates (n=4). Levene's test to assess the homogeneity of variance of replicates and then one-way analysis of variance (ANOVA) for the comparisons of mean values of independent groups were performed at the level of 0.01 ($\alpha = 0.01$) (OriginPro 8.6.0 b70). A significant effect was reported at (*) $p < \alpha$ (0.01).

Flow Cytometry Studies: Nonspecific binding of Qdots was analyzed quantitatively by using a COULTER EPICS XL-MCL flow cytometer. A549 cells were first harvested with Accutase solution (Sigma-Aldrich). Following centrifugation at 300 g for 5 min, cell suspension was collected, and the number of viable cells was determined by trypan blue exclusion. Later, A549 cell suspensions (5×10^5) were incubated with $100 \mu\text{g mL}^{-1}$ COOH-Qdots and mPEG-Qdots prepared in culture medium (DMEM supplemented with 10% FCS and 1% P/S) for 30 min at 26 °C/ 300 rpm. Afterward cells were washed three times with PBS and resuspended in 500 μL PBS buffer (supplemented with 2% FCS). Cells were filtered through cell strainer (BD Falcon, 70 μm nylon) directly into capillary tubes for flow cytometry measurements. An excitation laser at 488 nm was used, and corresponding fluorescence intensities were collected with the fluorescence-3 (FL3) sensor using band-pass filter at 675 ± 15 nm, and the data was analyzed by WinMDI 2.9 software. Cellular fragments and debris were excluded from the analysis by gating the fluorescence on the side scatter vs forward angle light scatter signal. Geometric-mean (g-mean) fluorescence intensity of the cellular autofluorescence was subtracted from the g-mean values of the positive cells. The binding effect was defined as the ratio between the normalized fluorescence intensity of cells incubated with COOH-Qdots and mPEG-Qdots.

Microscopy Studies: Bright-field images of A549 tumor-like spheroids that were treated with Qdots at different concentrations were captured with Olympus Ix50 inverted light microscope equipped with an Olympus camera (SC30, Japan) by using cellSens Standard software (Olympus Co. Japan). For labeling experiments, A549 spheroids were treated with $100 \mu\text{g mL}^{-1}$ Qdots solutions for 1 and 24 h at 37 °C, 5% CO_2 . After incubation, spheroids were washed gently with PBS solution and placed on μ -slide glass bottom microscopy chamber slides (ibidi GmbH, Germany) for confocal imaging studies. Fluorescence images were acquired using Zeiss LSM-510 Meta confocal microscope (Zeiss, Germany) with argon/2 excitation laser at 488 nm. Image processing and analysis were conducted with ImageJ software. For intensity analysis

equal amount of background subtraction was applied to all images (rolling ball radius: 1000 pixels).

4.3.7. Acknowledgements

This work was carried out as an integral part of the BIOFABRICATION FOR NIFE Initiative (Lower Saxony Centre for Biomedical Engineering, Implant Research and Development in Hannover), which is financially supported by the Lower Saxony ministry of Science and Culture and the Volkswagen Foundation. Part of this work was also funded by the German Research Foundation (DFG) for the Cluster of Excellence REBIRTH (From Regenerative Biology to Reconstructive Therapy). R. J. acknowledges the Niedersächsische Krebsgesellschaft e.V. for financial support. We also thank Prof. Dr. -Ing. Birgit Glasmacher and Daniel Mueller (Institute of Multiphase Processes) for providing us access to the confocal microscope, Hamza Belhadj for his assistance in ATR-FTIR analysis, Paul Maschhoff (Department of Chemical Engineering, Northeastern University) for his support in editing the manuscript, and Marc Krey for his assistance in TG analysis.

4.3.8. References

- (1) Kovalenko, M. V., Manna, L., Cabot, A., Hens, Z., Talapin, D. V., Kagan, C. R., Klimov, V. I., Rogach, A. L., Reiss, P., Milliron, D. J., et al. (2015) Prospects of Nanoscience with Nanocrystals. *ACS Nano* 9, 1012–1057.
- (2) Lanza, G. M. (2015) Theranostic agents: From micro to nano in seconds. *Nat. Nanotechnol.* 10, 301–2.
- (3) Mahmoudi, M., Meng, J., Xue, X., Liang, X. J., Rahman, M., Pfeiffer, C., Hartmann, R., Gil, P. R., Pelaz, B., Parak, W. J., et al. (2014) Interaction of stable colloidal nanoparticles with cellular membranes. *Biotechnol. Adv.* 32, 679–692.
- (4) Pfeiffer, C., Rehbock, C., Huhn, D., Carrillo-Carrion, C., de Aberasturi, D. J., Merk, V., Barcikowski, S., and Parak, W. J. (2014) Interaction of colloidal nanoparticles with their local environment: the (ionic) nanoenvironment around nanoparticles is different from bulk and determines the physico-chemical properties of the nanoparticles. *J. R. Soc., Interface* 11, 10.1098/rsif.2013.0931.
- (5) Zhu, Z. J., Ghosh, P. S., Miranda, O. R., Vachet, R. W., and Rotello, V. M. (2008) Multiplexed Screening of Cellular Uptake of Gold Nanoparticles Using Laser Desorption/Ionization Mass Spectrometry. *J. Am. Chem. Soc.* 130, 14139–14143.
- (6) Verma, A., and Stellacci, F. (2010) Effect of Surface Properties on Nanoparticle-Cell Interactions. *Small* 6, 12–21.
- (7) Treuel, L., Jiang, X. E., and Nienhaus, G. U. (2013) New views on cellular uptake and trafficking of manufactured nanoparticles. *J. R. Soc., Interface* 10, 10.1098/rsif.2012.0939.

- (8) Monopoli, M. P., Walczyk, D., Campbell, A., Elia, G., Lynch, I., Bombelli, F. B., and Dawson, K. A. (2011) Physical-Chemical Aspects of Protein Corona: Relevance to in Vitro and in Vivo Biological Impacts of Nanoparticles. *J. Am. Chem. Soc.* 133, 2525–2534.
- (9) Lesniak, A., Salvati, A., Santos-Martinez, M. J., Radomski, M. W., Dawson, K. A., and Aberg, C. (2013) Nanoparticle Adhesion to the Cell Membrane and Its Effect on Nanoparticle Uptake Efficiency. *J. Am. Chem. Soc.* 135, 1438–1444.
- (10) Paszek, E., Czyz, J., Woznicka, O., Jakubiak, D., Wojnarowicz, J., Lojkowski, W., and Stepień, E. (2012) Zinc Oxide Nanoparticles Impair the Integrity of Human Umbilical Vein Endothelial Cell Monolayer In Vitro. *J. Biomed. Nanotechnol.* 8, 957–967.
- (11) Hak, S., Helgesen, E., Hektoen, H. H., Huuse, E. M., Jarzyna, P. A., Mulder, W. J. M., Haraldseth, O., and Davies, C. D. (2012) The Effect of Nanoparticle Polyethylene Glycol Surface Density on Ligand-Directed Tumor Targeting Studied in Vivo by Dual Modality Imaging. *ACS Nano* 6, 5648–5658.
- (12) Pehler, J., Brecht, A., Valiokas, R., Liedberg, B., and Gauglitz, G. (2000) A high-density poly(ethylene glycol) polymer brush for immobilization on glass-type surfaces. *Biosens. Bioelectron.* 15, 473–481.
- (13) Dai, Q., Walkey, C., and Chan, W. C. W. (2014) Polyethylene Glycol Backfilling Mitigates the Negative Impact of the Protein Corona on Nanoparticle Cell Targeting. *Angew. Chem., Int. Ed.* 53, 5093–5096.
- (14) Waku, T., Matsusaki, M., Kaneko, T., and Akashi, M. (2007) PEG brush peptide nanospheres with stealth properties and chemical functionality. *Macromolecules* 40, 6385–6392.
- (15) Torrisi, V., Graillot, A., Vitorazi, L., Crouzet, Q., Marletta, G., Loubat, C., and Berret, J. F. (2014) Preventing Corona Effects: Multiphosphonic Acid Poly(ethylene glycol) Copolymers for Stable Stealth Iron Oxide Nanoparticles. *Biomacromolecules* 15, 3171–3179.
- (16) Orts-Gil, G., Natte, K., Thiermann, R., Girod, M., Rades, S., Kalbe, H., Thunemann, A. F., Maskos, M., and Osterle, W. (2013) On the role of surface composition and curvature on biointerface formation and colloidal stability of nanoparticles in a protein-rich model system. *Colloids Surf., B* 108, 110–119.
- (17) Daou, T. J., Li, L., Reiss, P., Jossierand, V., and Texier, I. (2009) Effect of Poly(ethylene glycol) Length on the in Vivo Behavior of Coated Quantum Dots. *Langmuir* 25, 3040–3044.
- (18) Perrault, S. D., Walkey, C., Jennings, T., Fischer, H. C., and Chan, W. C. W. (2009) Mediating Tumor Targeting Efficiency of Nanoparticles Through Design. *Nano Lett.* 9, 1909–1915.
- (19) Hu, Y., Xie, J. W., Tong, Y. W., and Wang, C. H. (2007) Effect of PEG conformation and particle size on the cellular uptake efficiency of nanoparticles with the HepG2 cells. *J. Controlled Release* 118, 7–17.
- (20) Sant, S., Poulin, S., and Hildgen, P. (2008) Effect of polymer architecture on surface properties, plasma protein adsorption, and cellular interactions of pegylated nanoparticles. *J. Biomed. Mater. Res., Part A* 87A, 885–895.
- (21) Heyes, C. D., Groll, J., Moller, M., and Nienhaus, G. U. (2007) Synthesis, patterning and applications of star-shaped poly(ethyleneglycol) biofunctionalized surfaces. *Mol. BioSyst.* 3, 419–430.
- (22) Kim, D., Park, S., Lee, J. H., Jeong, Y. Y., and Jon, S. (2007) Antibiofouling polymer-coated gold nanoparticles as a contrast agent for in vivo X-ray computed tomography imaging (vol 129, pg 7661, 2007). *J. Am. Chem. Soc.* 129, 12585–12585.
- (23) Klapper, Y., Vranceanu, M., Ishitsuka, Y., Evans, D., Scheider, D., Nienhaus, G. U., and Lenewit, G. (2013) Surface energy of phospholipid bilayers and the correlation to their hydration. *J. Colloid Interface Sci.* 390, 267–274.
- (24) Wan, H., Zhang, Y., Zhang, W. B., and Zou, H. F. (2015) Robust Two-Photon Visualized Nanocarrier with Dual Targeting Ability for Controlled Chemo-Photodynamic Synergistic Treatment of Cancer. *ACS Appl. Mater. Interfaces* 7, 9608–9618.
- (25) Dong, H. F., Dai, W. H., Ju, H. X., Lu, H. T., Wang, S. Y., Xu, L. P., Zhou, S. F., Zhang, Y., and Zhang, X. J. (2015) Multifunctional Poly(L-lactide)-Polyethylene Glycol-Grafted Graphene Quantum Dots for Intracellular MicroRNA Imaging and Combined Specific-Gene-Targeting Agents Delivery for Improved Therapeutics. *ACS Appl. Mater. Interfaces* 7, 11015–11023.

- (26) Zhang, P. F., and Han, H. X. (2012) Compact PEGylated polymer-caged quantum dots with improved stability. *Colloids Surf., A* 402, 72–79.
- (27) Pelaz, B., Del Pino, P., Maffre, P., Hartmann, R., Gallego, M., Rivera-Fernandez, S., de la Fuente, J. M., Nienhaus, G. U., and Parak, W. J. (2015) Surface Functionalization of Nanoparticles with Polyethylene Glycol: Effects on Protein Adsorption and Cellular Uptake. *ACS Nano* 9, 6996.
- (28) Mukhopadhyay, A., Joshi, N., Chattopadhyay, K., and De, G. (2012) A Facile Synthesis of PEG-Coated Magnetite (Fe₃O₄) Nanoparticles and Their Prevention of the Reduction of Cytochrome C. *ACS Appl. Mater. Interfaces* 4, 142–149.
- (29) Seol, S. K., Kim, D., Jung, S., Chang, W. S., and Kim, J. T. (2013) One-Step Synthesis of PEG-Coated Gold Nanoparticles by Rapid Microwave Heating. *J. Nanomater.* 2013, 531760.
- (30) Shameli, K., Ahmad, M. B., Jazayeri, S. D., Sedaghat, S., Shabanzadeh, P., Jahangirian, H., Mahdavi, M., and Abdollahi, Y. (2012) Synthesis and characterization of polyethylene glycol mediated silver nanoparticles by the green method. *Int. J. Mol. Sci.* 13, 6639–50.
- (31) Huang, W. Y., Bai, D. W., Li, L. J., Wei, H. D., Shi, Z. P., Cheng, H., and Li, Y. Q. (2015) The synthesis of ultrasmall ZnO@PEG nanoparticles and its fluorescence properties. *J. Sol-Gel Sci. Technol.* 74, 718–725.
- (32) Shen, J. H., Zhu, Y. H., Yang, X. L., Zong, J., Zhang, J. M., and Li, C. Z. (2012) One-pot hydrothermal synthesis of graphene quantum dots surface-passivated by polyethylene glycol and their photoelectric conversion under near-infrared light. *New J. Chem.* 36, 97–101.
- (33) Zhang, Y. A., Jiang, D., He, Z., Yu, Y. W., Zhang, H. B., and Jiang, Z. H. (2014) Hydrothermal Synthesis of PEG-capped ZnS:Mn²⁺ Quantum Dots Nanocomposites. *Chem. Res. Chin. Univ.* 30, 176–180.
- (34) Rao, L., Lu, W., Zeng, T. M., Yi, Z. G., Wang, H. B., Liu, H. R., and Zeng, S. J. (2014) One-pot synthesis of PEG modified BaLuF₅:Gd/Yb/Er nanoprobe for dual-modal in vivo upconversion luminescence and X-ray bioimaging. *Dalton T* 43, 13343–13348.
- (35) Ulusoy, M., Walter, J. G., Lavrentieva, A., Kretschmer, I., Sandiford, L., Le Marois, A., Bongartz, R., Aliuos, P., Suhling, K., Stahl, F., et al. (2015) One-pot aqueous synthesis of highly strained CdTe/CdS/ZnS nanocrystals and their interactions with cells. *RSC Adv.* 5, 7485–7494.
- (36) Derfus, A. M., Chan, W. C. W., and Bhatia, S. N. (2004) Probing the cytotoxicity of semiconductor quantum dots. *Nano Lett.* 4, 11–18.
- (37) Li, Z., Dong, C. Q., Tang, L. C., Zhu, X., Chen, H. J., and Ren, J. C. (2011) Aqueous synthesis of CdTe/CdS/ZnS quantum dots and their optical and chemical properties. *Luminescence* 26, 439–448.
- (38) Li, L. L., Chen, Y., Lu, Q., Ji, J., Shen, Y. Y., Xu, M., Fei, R., Yang, G. H., Zhang, K., Zhang, J. R., and Zhu, J.-J. (2013) Electrochemiluminescence energy transfer-promoted ultrasensitive immunoassay using near-infrared-emitting CdSeTe/CdS/ZnS quantum dots and gold nanorods. *Sci. Rep.* 3, 1529.
- (39) He, Y., Lu, H. T., Sai, L. M., Su, Y. Y., Hu, M., Fan, C. H., Huang, W., and Wang, L. H. (2008) Microwave synthesis of water-dispersed CdTe/CdS/ZnS core-shell-shell quantum dots with excellent photostability and biocompatibility. *Adv. Mater.* 20, 3416.
- (40) Zhang, Y. Y., Kim, J. Y., Kim, Y., and Jang, D. J. (2012) Controlled optical properties of water-soluble CdTe/CdS/ZnS quantum dots. *J. Nanopart. Res.* 14, 10.1007/s11051-012-1117-9.
- (41) Mudunkotuwa, I. A., Al Minshid, A., and Grassian, V. H. (2014) ATR-FTIR spectroscopy as a tool to probe surface adsorption on nanoparticles at the liquid-solid interface in environmentally and biologically relevant media. *Analyst* 139, 870–881.
- (42) Lu, J. Q., Lu, S. Y., Ye, T., and Zhou, X. W. (2011) Synthesis of Multifunctional Mn-Doped CdTe/ZnS Core/Shell Quantum Dots. *Chin. J. Chem.* 29, 2308–2314.
- (43) Chen, Z. J., Zhou, Y. M., Zhang, T., Bu, X. H., and Sheng, X. L. (2014) Preparation and Characterization of Optically Active Polyacetylene@CdTe Quantum Dots Composites with Low Infrared Emissivity. *J. Inorg. Organomet. Polym. Mater.* 24, 591–599.
- (44) Li, X., Ni, X. F., Liang, Z. H., and Shen, Z. Q. (2012) Synthesis of imidazolium-functionalized ionic polyurethane and formation of CdTe quantum dot-polyurethane nanocomposites. *J. Polym. Sci., Part A: Polym. Chem.* 50, 509–516.

- (45) Sebby, K. B., and Mansfield, E. (2015) Determination of the surface density of polyethylene glycol on gold nanoparticles by use of microscale thermogravimetric analysis. *Anal. Bioanal. Chem.* 407, 2913–2922.
- (46) Rahme, K., Chen, L., Hobbs, R. G., Morris, M. A., O’Driscoll, C., and Holmes, J. D. (2013) PEGylated gold nanoparticles: polymer quantification as a function of PEG lengths and nanoparticle dimensions. *RSC Adv.* 3, 6085–6094.
- (47) Zhang, H., Zhou, Z., Yang, B., and Gao, M. Y. (2003) The influence of carboxyl groups on the photoluminescence of mercaptocarboxylic acid-stabilized CdTe nanoparticles. *J. Phys. Chem. B* 107, 8–13.
- (48) Poderys, V., Matulionyte, M., Selskis, A., and Rotomskis, R. (2011) Interaction of Water-Soluble CdTe Quantum Dots with Bovine Serum Albumin. *Nanoscale Res. Lett.* 6, 10.1007/s11671-010-9740-9.
- (49) Aldana, J., Lavelle, N., Wang, Y. J., and Peng, X. G. (2005) Size-dependent dissociation pH of thiolate ligands from cadmium chalcogenide nanocrystals. *J. Am. Chem. Soc.* 127, 2496–2504.
- (50) Del Pino, P., Pelaz, B., Zhang, Q., Maffre, P., Nienhaus, G. U., and Parak, W. J. (2014) Protein corona formation around nanoparticles: from the past to the future. *Mater. Horiz.* 1, 301–313.
- (51) Gebauer, J. S., Malissek, M., Simon, S., Knauer, S. K., Maskos, M., Stauber, R. H., Peukert, W., and Treuel, L. (2012) Impact of the Nanoparticle-Protein Corona on Colloidal Stability and Protein Structure. *Langmuir* 28, 9673–9679.
- (52) Mahmoudi, M., Abdelmonem, A. M., Behzadi, S., Clement, J. H., Dutz, S., Ejtehadi, M. R., Hartmann, R., Kantner, K., Linne, U., Maffre, P., et al. (2013) Temperature: The “Ignored” Factor at the NanoBioInterface. *ACS Nano* 7, 6555–6562.
- (53) Wienken, C. J., Baaske, P., Rothbauer, U., Braun, D., and Duhr, S. (2010) Protein-binding assays in biological liquids using microscale thermophoresis. *Nat. Commun.* 1, 100.
- (54) Huhn, D., Kantner, K., Geidel, C., Brandholt, S., De Cock, I., Soenen, S. J. H., Gil, P. R., Montenegro, J. M., Braeckmans, K., Mullen, K., et al. (2013) Polymer-Coated Nanoparticles Interacting with Proteins and Cells: Focusing on the Sign of the Net Charge. *ACS Nano* 7, 3253–3263.
- (55) Jiang, X., Weise, S., Hafner, M., Rocker, C., Zhang, F., Parak, W. J., and Nienhaus, G. U. (2010) Quantitative analysis of the protein corona on FePt nanoparticles formed by transferrin binding. *J. R. Soc., Interface* 7, S5–S13.
- (56) Bottrill, M., and Green, M. (2011) Some aspects of quantum dot toxicity. *Chem. Commun.* 47, 7039–7050.
- (57) Cho, W. S., Cho, M. J., Jeong, J., Choi, M., Cho, H. Y., Han, B. S., Kim, S. H., Kim, H. O., Lim, Y. T., Chung, B. H., et al. (2009) Acute toxicity and pharmacokinetics of 13 nm-sized PEG-coated gold nanoparticles. *Toxicol. Appl. Pharmacol.* 236, 16–24.
- (58) Sabella, S., Carney, R. P., Brunetti, V., Malvindi, M. A., Al-Juffali, N., Vecchio, G., Janes, S. M., Bakr, O. M., Cingolani, R., Stellacci, F., et al. (2014) A general mechanism for intracellular toxicity of metal-containing nanoparticles. *Nanoscale* 6, 7052–7061.
- (59) Chithrani, B. D., Ghazani, A. A., and Chan, W. C. W. (2006) Determining the size and shape dependence of gold nanoparticle uptake into mammalian cells. *Nano Lett.* 6, 662–668.
- (60) Elliott, N. T., and Yuan, F. (2011) A Review of Three-Dimensional In Vitro Tissue Models for Drug Discovery and Transport Studies. *J. Pharm. Sci.* 100, 59–74.
- (61) da Rocha, E. L., Porto, L. M., and Rambo, C. R. (2014) Nanotechnology meets 3D in vitro models: Tissue engineered tumors and cancer therapies. *Mater. Sci. Eng., C* 34, 270–279.
- (62) Stevens, M. M. (2009) Testing in the third dimension. *Nat. Nanotechnol.* 4, 342–343.
- (63) Sambale, F., Lavrentieva, A., Stahl, F., Blume, C., Stiesch, M., Kasper, C., Bahnemann, D., and Scheper, T. (2015) Three-dimensional spheroid cell culture for nanoparticle safety testing. *J. Biotechnol.* 205, 120–9.
- (64) Ulusoy, M., Lavrentieva, A., Walter, J.-G., Sambale, F., Green, M., Stahl, F., and Scheper, T. (2015) Evaluation of CdTe/CdS/ZnS core/shell/shell quantum dot toxicity on three-dimensional spheroid cultures. *Toxicol. Res.*, DOI: 10.1039/C5TX00236B.
- (65) Todescato, F., Minotto, A., Signorini, R., Jasieniak, J. J., and Bozio, R. (2013) Investigation into the Heterostructure Interface of CdSe-Based Core-Shell Quantum Dots Using Surface-Enhanced Raman Spectroscopy. *ACS Nano* 7, 6649–6657.

- (66) Tamang, S., Beaune, G., Texier, I., and Reiss, P. (2011) Aqueous phase transfer of InP/ZnS nanocrystals conserving fluorescence and high colloidal stability. *ACS Nano* 5, 9392–402.
- (67) Goodman, T. T., Ng, C. P., and Pun, S. H. (2008) 3-D Tissue Culture Systems for the Evaluation and Optimization of Nanoparticle-Based Drug Carriers. *Bioconjugate Chem.* 19, 1951–1959.
- (68) Mehta, G., Hsiao, Y. A., Ingram, M., Luker, D. G., and Takayama, S. (2012) Opportunities and Challenges for use of Tumor Spheroids as Models to Test Drug Delivery and Efficacy. *J. Controlled Release* 164, 192–204.
- (69) Kim, E., Jeon, W. B., Kim, S., and Lee, S. K. (2014) Decrease of Reactive Oxygen Species-Related Biomarkers in the Tissue-Mimic 3D Spheroid Culture of Human Lung Cells Exposed to Zinc Oxide Nanoparticles. *J. Nanosci. Nanotechnol.* 14, 3356–3365.
- (70) Mueller, D., Kramer, L., Hoffmann, E., Klein, S., and Noor, F. (2014) 3D organotypic HepaRG cultures as in vitro model for acute and repeated dose toxicity studies. *Toxicol. In Vitro* 28, 104–112.
- (71) Lee, J., Lilly, G. D., Doty, R. C., Podsiadlo, P., and Kotov, N. A. (2009) In vitro Toxicity Testing of Nanoparticles in 3D Cell Culture. *Small* 5, 1213–1221.
- (72) Chattopadhyay, P. K., Price, D. A., Harper, T. F., Betts, M. R., Yu, J., Gostick, E., Perfetto, S. P., Goepfert, P., Koup, R. A., De Rosa, S. C., et al. (2006) Quantum dot semiconductor nanocrystals for immunophenotyping by polychromatic flow cytometry. *Nat. Med.* 12, 972–977.
- (73) Michel, R., Pasche, S., Textor, M., and Castner, D. G. (2005) Influence of PEG architecture on protein adsorption and conformation. *Langmuir* 21, 12327–12332.
- (74) Treuel, L., Brandholt, S., Maffre, P., Wiegele, S., Shang, L., and Nienhaus, G. U. (2014) Impact of Protein Modification on the Protein Corona on Nanoparticles and Nanoparticle-Cell Interactions. *ACS Nano* 8, 503–513.
- (75) Cho, E. C., Xie, J. W., Wurm, P. A., and Xia, Y. N. (2009) Understanding the Role of Surface Charges in Cellular Adsorption versus Internalization by Selectively Removing Gold Nanoparticles on the Cell Surface with a I-2/KI Etchant. *Nano Lett.* 9, 1080–1084.
- (76) Cho, E. C., Au, L., Zhang, Q., and Xia, Y. N. (2010) The Effects of Size, Shape, and Surface Functional Group of Gold Nanostructures on Their Adsorption and Internalization by Cells. *Small* 6, 517–522.

4.3.9. Supplementary Information

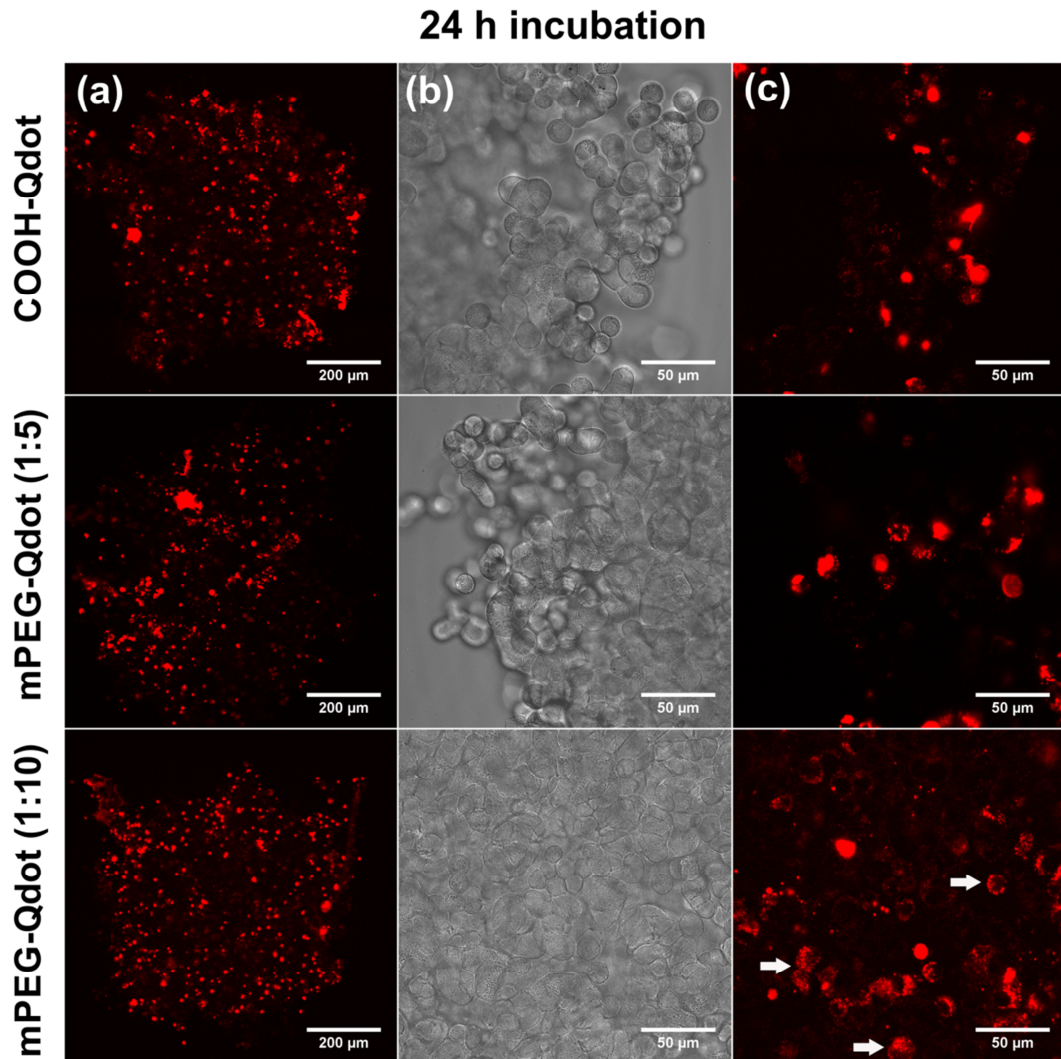


Figure S1. Confocal microscope images of A549 tumor-like spheroids treated with COOH- and mPEG-Qdots for 24 h. Column (a) shows low magnified fluorescence images of tumor spheroids, (b) shows high-magnification bright-field images of spheroid surfaces, and (c) their respective fluorescence profiles showing Qdots binding and uptake. White arrows in the bottom-right images highlight partial internalization of mPEG-Qdots (1:10) by outer cells.

5. Conclusions and Outlook

The objectives of this project were to establish an aqueous synthesis route to generate water soluble and functional Qdots, to test their applicability in targeted cell imaging, to investigate their cytotoxicity and labelling efficiency on 3D spheroid cultures, and to improve their surface-related characteristics with mPEG molecules. As a summary, generation of water-soluble CdTe/CdS/ZnS Qdots with improved fluorescence yields was achieved. Cellular uptake of Qdots by the target cells was accomplished by coupling Qdots with aptamers. Cytotoxicity studies showed that the 3D spheroids were more resistant to Qdot toxicity than the conventional 2D cell cultures. Improvement of Qdot surface structure was established through incorporating mPEG molecules to the Qdot surface. mPEG ligands not only improved the colloidal stability of Qdots, but also mitigated the Qdot toxicity to a great extent. Moreover, Qdots with inherent size and surface structure exhibited great potential to label 3D spheroids.

In general poor solubility and stability, low biocompatibility, and toxicity of Qdots comprise the major problems for their use in bioimaging studies. The developed Qdots in this study displayed improved fluorescence yields, increased stability and biocompatibility. Therefore, the outcomes provide valuable solutions to address these problems while enhancing the applicability of Qdot in 3D structures as diagnostic agents. Moreover, the results are also of particular importance for the development of improved surface structures to elevate safe application of Qdots in biomedicine.

Aqueous synthesis of Qdots and their application in targeted imaging

Herein, an aqueous approach was developed to synthesize water-soluble and functional Qdots to facilitate their application in fluorescence imaging studies. Initially, one-pot aqueous synthesis of red-emitting Qdots composed of a CdTe/CdS/ZnS core_(small)/shell_(thick)/shell_(thin) structure was demonstrated. 3-mercaptopropionic acid (MPA) was utilized as the sulphur source for the CdS and ZnS shell formation, as well as the surface passivation ligand. It introduced negatively-charged carboxyl groups to the surface of Qdot, thereby facilitated water solubility and stabilization through electrostatic interactions. Firstly, the synthesis of CdTe/CdS Qdots with a very small CdTe core and a very thick CdS shell was achieved. CdTe/CdS Qdots displayed a type-II band structure owing to strain-induced optical properties. After 6 h of synthesis at 90

°C, CdTe/CdS Qdots emitting at 730 nm were obtained, and they exhibited a maximum quantum yield (QY%) of 57%. The optical properties of CdTe/CdS Qdots were further improved with the external growth of the ZnS shell. The band offsets between CdS and ZnS allowed efficient confinement of electron–hole pairs in the CdTe/CdS core/shell structure, therefore induced an increase in quantum yield by 7%. However, due to the large lattice mismatch between CdTe core and ZnS shell (16.4%), overgrowth of a thick ZnS shell (> 0.5 monolayer) led to formation of surface defects, and as a result fluorescence yield of Qdots declined. Only after a very thin ZnS formation (≤ 0.5 monolayer), Qdots could maintain their fluorescence efficiencies. High-resolution transmission microscope images displayed the crystalline structure of the Qdots having either spherical or tetrahedral shapes with an average size of 4.3 nm. The lattices stretching straight across the entire Qdot indicated the epitaxial growth of the ZnS shell without forming significant crystalline defects. X-ray diffraction analysis revealed that as-prepared Qdots possess a zinc blende cubic crystal structure. Moreover X-ray diffraction patterns confirmed the formation of a separate ZnS shell around CdTe/CdS Qdots rather than formation of an alloyed CdZnS shell structure. The resulting CdTe/CdS and the corresponding CdTe/CdS/ZnS Qdots demonstrated very high photostability under continuous UV-irradiation after 5 h. After the irradiation, Qdot emission profiles remained almost unchanged, ruling out the possibility of photo-oxidation. Instead of that, fluorescence intensities increased by 30% for CdTe/CdS Qdots and 12% for CdTe/CdS/ZnS Qdots. This fluorescence enhancement effect was attributed to photo-annealing of surface defect sites under UV-irradiation. This effect was also found to be more pronounced for the CdTe/CdS Qdots due to the higher concentration of surface defects in comparison to CdTe/CdS/ZnS Qdots.

Later, dose-dependent *in vitro* cytotoxicity of Qdots was studied by using monolayer cultures of A549 adenocarcinoma cell line. It was observed that Qdots evinced different levels of toxicity depending on their size, composition, and exposure time. When the cells were exposed to high Qdots concentrations for 2 h, cells retained more than 70% of their viability, indicating Qdots didn't exhibit significant toxicity. However, as the exposure time was prolonged to 24 h, Qdots induced toxicity at different levels with a correlation to their size, shell composition, and ZnS shell thickness. Consequently, smaller CdTe/CdS Qdots demonstrated more toxicity than their larger counterparts. The presence of the outer ZnS shell mitigated Qdot adverse effects, and an increase in ZnS

thickness further decreased the toxicity. These results proved that the presence of a well-passivating and protective ZnS shell layer minimized the destabilization of Qdots and the release of highly toxic Cd²⁺ metal ions to the cellular environment.

As-prepared CdTe/CdS/ZnS Qdots were later coupled with DNA aptamers directed against A549 adenocarcinoma cells. The preliminary cell imaging experiments exhibited that the aptamer-Qdots bioconjugates were effectively internalized by the cells after 2 h of incubation. Unmodified Qdots as well as Qdots coupled with a random oligonucleotide were not able to accumulate into the cells as much as the positive samples. Moreover, the aptamer-Qdot bioconjugates preserved their brightness inside the cells after 24 h of uptake. In conclusion, the developed CdTe/CdS/ZnS Qdots exhibited very high optical efficiency, photostability, and a reduced cytotoxicity. Therefore, they represent an ideal candidate as a fluorescent probe for bioimaging applications.

Application of Qdots to 3D spheroid cultures

In this part, 3D spheroid cultures were used to assess toxicity issues of Qdots as well as their labelling efficiency in order to obtain physiologically relevant data about Qdot interactions with such *in vivo*-like cellular structures. For that, the dose-dependent adverse effects of CdTe/CdS/ZnS Qdots on the 3D spheroid cultures of primary human adipose-derived mesenchymal stem cells (hAD-MSCs) were studied. Initially, morphological changes in hAD-MSCs spheroid structures were investigated in dependence from the time point of treatment with different Qdots doses. For this, two different treatment models were applied. In the first model, cells were exposed to Qdots 24 h after formation of the spheroids in order to investigate the effect of Qdots to spheroids. In the second model, Qdots were administered to the cells at the beginning of spheroid formation in order to observe the effect of Qdots on the spheroid formation. According to the end-point bright-field images and time-lapse microscopy studies, Qdots caused distinct adverse effects to spheroid morphologies. In the case of cells incubated with Qdots during cell aggregation, high Qdots doses ($\geq 300 \mu\text{g ml}^{-1}$) induced drastic effects to the cells during spheroid formation. As a result, cells formed several smaller spheroids instead of one large spheroid. It can be concluded that toxic levels of Qdots significantly hindered cell–cell and cell–extracellular matrix interactions, thus prevented cells to form spheroids. Furthermore, from the granular structure of the cells, it can be assumed that cells also lost their viability. However, this

drastic effect wasn't observed in the other 3D model of which cells were exposed to Qdots after spheroid formation. At this model, only high Qdot concentrations ($>300 \mu\text{g ml}^{-1}$) caused observable alterations to the spheroid morphology. Formation of a rough surface was observed due to protruding of granular shaped cells, corresponding to a significant increase in cell death. However, the granular cells did not detach from the spheroid surface due to the presence of close cell junctions in tightly packed stem cell spheroids. Although cells preserved the intact spherical structure, they increased the diameter of the spheroid by 48%.

Further, ATP and CTB cell viability assays were conducted to study the dose-dependent effect of Qdots to the cell metabolic activity. According to the cell viability results obtained via ATP assay, significant differences were observed between 2D and 3D cell cultures. 2D cultures featured a biphasic dose-response curve, whereas 3D spheroid cultures displayed a typical monotonic dose-response profile. The presence of biphasic dose-response pattern in 2D cultures might be attributed to the existence of two distinct cell populations with different sensitivity to Qdots. As a result, 2D monolayer cell cultures were found to be more susceptible to Qdot toxicity. In 3D spheroids, cell-cell and cell-ECM interactions are generally formed in all three dimensions, and therefore they play a protective role against Qdot-induced toxicity. However, in 2D monolayer cultures, cells attach on one side to plastic substrate, therefore they only have periphery cell contacts. For that reason, they are readily exposed to medium on their exterior surface. This makes cells more vulnerable to the changes in their environments.

Lastly, CdTe/CdS/ZnS Qdots were tested for their penetration ability in 3D spheroid structures. For that, hAD-MSC spheroids were treated with Qdots, and afterwards monitored with fluorescence and confocal microscopes. The obtained fluorescence images revealed that Qdots were uptaken mostly by peripheral cells of the spheroid structure, and not captured non-specifically by extracellular matrix material. The live cell staining with Calcein-AM showed that cells retained their viability during Qdot treatment. Consequently, as-prepared Qdots with their inherent size, surface structure, and high fluorescence efficiency demonstrated a great versatility in 3D imaging. These features can be utilized in the future for targeted delivery studies especially by using solid tumor-like spheroids.

Surface modification of Qdots with mPEG ligands

In this part, surface-related features of Qdots were aimed to be improved by modifying Qdot surfaces with mPEG molecules since mPEG ligands confer advantageous properties to colloidal nanoparticles. For that, an aqueous *in situ* approach for the incorporation of thiol-terminated mPEG molecules to the surface of Qdots was developed. The surface of Qdots was modified simultaneously with carboxyl groups originated from MPA molecules and mPEG ligands during the deposition of the outer ZnS shell. Carboxyl groups enabled functionalization of Qdot surfaces, whilst mPEG molecules formed a stable brush layer to preserve colloidal stability of Qdots. Two different mPEG amounts were used during the ZnS shell deposition according to the Zn²⁺/mPEG molar ratio to be (1:5) and (1:10). The effect of mPEG density on physicochemical properties of Qdots in terms of ZnS deposition rate, Qdot surface charge, colloidal stability, cytotoxicity, and non-specific cellular interactions were investigated. Regarding the ZnS shell growth, it was found out that the higher mPEG amount decelerated the deposition of the ZnS shell significantly, and caused a slight decrease in fluorescence efficiency. However, monodispersity of the Qdots was maintained. Zeta potential analyses were conducted to measure the electrical potential of the Qdots. The obtained values demonstrated that zeta potential value became less negative upon the introduction of mPEG molecules due to the partial replacement of negatively-charged MPA ligands by non-ionic mPEG molecules. As the amount of mPEG was increased, the resulting zeta potential value was reduced further, indicating an increase in the grafting amount of mPEG to the surface of Qdot. Afterwards, colloidal stability of Qdots was tested in order to examine the effect of mPEG molecules particularly at biologically relevant conditions. For that different aqueous media including pure water, serum-free culture medium, and 10% serum-containing culture medium, and different incubation temperatures at 4 °C and 37 °C were used. In summary, carboxylated-Qdots showed a greater tendency to aggregation in all aqueous media in comparison to their PEGylated counterparts. The higher incubation temperature induced faster agglomeration of Qdots than in the case of low temperature. Incorporation of mPEG polymers enabled a significant improvement in colloidal stability of Qdots via providing a steric barrier, thus preventing interparticle interactions. Qdots possessing the highest surface mPEG amount yielded the highest colloidal stability. This can be accounted for by the formation of a more stable brush

layer through coordination of the thiol groups of mPEG with Zn^{2+} ions during ZnS shell growth. In serum-free culture medium, presence of salt cations (e.g. Na^+ and Ca^{2+}) accelerated agglomeration of Qdots. It might be due to the screening of the surface negative charges by counterions in the culture medium, resulting in reduced electrostatic repulsive forces. In serum-containing medium, Qdots exhibited a minimal aggregation tendency in comparison to the other aqueous media. It might be attributed to the adsorption of serum proteins on Qdot surfaces, thus forming a protein corona structure. Consequently, the presence of the protein layer on colloidal Qdot surfaces improved the stability of Qdots against agglomeration.

In the next step, *in vitro* cytotoxicity of PEGylated-Qdots was addressed by using both 2D monolayer cultures and 3D tumor-like spheroid cultures of A549 adenocarcinoma cells. The cell viability results showed that, PEGylated-Qdots elicited a significant reduction in Qdot-induced toxicity in comparison to carboxylated-Qdots. In 3D tumor-like spheroid cultures, all Qdot samples exhibited a reduced toxicity in comparison to 2D cultures, agreeing with the previous results obtained in the previous chapter. On the basis of these observations, it can be stated that the presence of mPEG molecules on Qdot surfaces minimized negative Qdots side effects via improving the colloidal stability of Qdots. Additionally, mPEG-modified Qdots with a higher mPEG density demonstrated a reduced cellular binding to 2D cell culture. An increase in mPEG amount on the Qdot surface caused a concomitant decrease in non-specific binding of Qdots to the cells within the given incubation conditions. In 3D tumor-like spheroids, carboxylated-Qdots and Qdots modified with a low mPEG amount showed similar binding features. After 1 h of incubation, they mostly accumulated to the cell membranes; whereas after 24 h of incubation they were internalized by the cells reside on the outer surface of the spheroid. In the mean time, carboxylated-Qdot lost their fluorescence intensity to a large extent, and agglomerations occurred on the spheroids. On the other hand, Qdots modified with a higher mPEG amount showed a distinguishable binding feature. Due to their slower adsorption rate, they remained mostly at the cell membranes even after 24 h of incubation, and there was only a partial uptake by cells on the spheroid outer region. However, they retained their fluorescence intensity, and showed a homogenous binding profile with a minimum aggregation. Overall, the results showed an enhancement in terms of surface-related properties of Qdot, and enabled application of PEGylated-Qdots in 3D spheroid imaging studies.

List of Abbreviations

ANOVA	One-way analysis of variance
AFM	Atomic force microscopy
ATP	Adenosine triphosphate
ATR-FTIR	Attenuated Total Reflection Fourier Transform Infrared
BOI	Biomolecules of interest
C-Qdot	Carbon quantum dot
CS	Core/shell
CSS	Core/shell/shell
CTB	CellTiter-Blue
CV	Coefficient of variance
Cys	L-cysteine
DAPI	4', 6-diamidino-2-phenylindole
DHLA	Dihydrolipoic acid
DMEM	Dulbecco's Modified Eagle Medium
DNA	Deoxyribonucleic acid
Dox	Doxorubicin
DSMZ	German Collection of Microorganism and Cell Cultures
ECM	Extracellular matrix
EDC	1-Ethyl-3-(3-dimethylamino-propyl)carbodiimide hydrochloride
FCS	Fetal calf serum
FFT	Fast-Fourier transformation
FWHM	Full width at half maximum
FRET	Fluorescence resonance energy transfer
GSH	Glutathione
hAD-MSCs	Human adipose-derived mesenchymal stem cells
HDA	Hexadecylamine
HRTEM	High-resolution transmission electron microscope
HS	Human serum
IC₅₀	Half-maximal inhibitory concentration
MEM-α	Minumum Essential Medium Alpha
ML	Monolayer
MMPs	Matrix metalloproteinases
MPA	3-mercaptopropionic acid
mPEG	Methoxy polyethylene glycol

MUA	Mercaptoundecanoic acid
MWCO	Molecular weight cut-off
NAC	N-acetyl-L-cysteine
NC	Nanocrystal
NIR	Near-infrared
NP	Nanoparticle
OA	Oleic acid
ODA	<i>n</i> -Octadecylamine
PBS	Phosphate buffered saline
PEG	Polyethylene glycol
PEI	Polyethylenimine
PES	Polyethersulfone
P/S	Penicillin/streptomycin
Qdots	Quantum dots
QY	Quantum yield
RES	Reticuloendothelial system
rGO	Reduced graphene oxide
ROS	Reactive oxygen species
Si-Qdot	Silica quantum dot
TGA	Thioglycolic acid
TOP	Tri- <i>n</i> -octylphosphine
TOPO	Tri- <i>n</i> -octylphosphine oxide
TEM	Transmission electron microscope
XRD	X-ray powder diffraction
0D	Zero-dimensional
1D	One-dimensional
2D	Two-dimensional
3D	Three-dimensional
ζ-Pot	Zeta-potential

List of Figures

Theoretical Background

Fig. 1 Schematic illustration of the energy levels of a semiconductor crystal structure as a function of dimension. 3D, 2D, 1D and 0D indicate three, two, one, and zero-dimension, respectively. The energy levels of the bulk semiconductor in 3D are continuous, while in the case of 0D energy levels are discrete. The exciton-Bohr diameter is represented by the sphere..... 6

Fig. 2 Schematization of the electronic band structure of a bulk semiconductor (left) and the quantum confinement effect on a quantum dot (right). E_g indicates the bandgap energy between the highest occupied molecular orbital and the lowest unoccupied molecular orbital for the bulk and the Qdot. Charge carriers are demonstrated with (+) and (–) signs, indicating hole and electron, respectively..... 7

Fig. 3 (a) Schematic representation of the quantum confinement effects: the bandgap of the Qdot increases with a decrease in its size, and discrete energy levels arise at the band-edges. Also, the energy difference between the band-edge levels increases with a decrease in size; (b) upper image shows the emission colours of Qdots from left-to right with increasing nanoparticle sizes, and the lower image shows their corresponding emission spectra covering a wide spectrum..... 8

Fig. 4 Heterostructures of Qdots: (i) inorganic core passivated with organic surface ligands; (ii) inorganic core/shell heterostructure passivated with organic surface ligands; (iii) inorganic core/shell/shell heterostructure coated with organic surface ligands; (iv) TEM images of $\text{CdS}_{1-x}\text{Se}_x$ Qdots showing their morphology as a function of Se loading: (a) 0% Se loading (CdS), (b) 5% Se loading ($\text{CdS}_{0.68}\text{Se}_{0.32}$), (c) 10% Se loading ($\text{CdS}_{0.42}\text{Se}_{0.58}$), (d) 20% Se loading ($\text{CdS}_{0.33}\text{Se}_{0.67}$), (e) 100% Se loading (CdSe). Scale bars: 50 nm (a, b, c), 100 nm (d), and 10 nm (e)..... 9

Fig. 5 Effect of surface states on the recombination process: (a) when the surface states are not passivated, the electrons at the conduction band can be trapped at the surface defect states, resulting in a weak surface state emission; (b) when the surface states are passivated well by inorganic shell layers, trap emission is eliminated and band-edge emission occurs..... 11

Fig. 6 The interrelationship between the bandgap energies, lattice constants, and lattice mismatches of CdTe, CdSe, CdS, and ZnS bulk semiconductors. The lattice parameters of bulk CdTe was utilized as a reference to calculate mismatch values..... 12

Fig. 7 Types of electronic band structures in Qdots that can be engineered by the selection of core and shell material: (a) Type-I band alignment– bandgap of the core is smaller than that of the shell, therefore electron and holes are confined in the core. A change in the shell thickness can induce slight red-shift in emission wavelengths. (b) type-II band alignment– valence and conduction band edges of the core are either lower or higher than those of the shell. Therefore, either electrons or holes are confined in the shell. An increase in the shell thickness can induce a great red-shift in emission wavelengths. (c) Inverse type-II band alignment, (d) quasi type-II band alignment– electrons are confined both in the core and shell, (e) inverse type-I alignment– both charge carriers are localized in the shell. Arrows show the lowest exciton energy separation between the occupied energy states at the core/shell interface (E_g). ... 13

Fig. 8 Schematic presentation of the nanocrystal formation mechanism. Initially, precursors react to form monomers which later nucleate to form small nuclei (A-B). As the reaction temperature rises, small nuclei grow into stable nanocrystals (C-D-E). 15

Fig. 9 Organometallic synthesis of colloidal CdSe core and CdSe/ZnS core/shell Qdots in high-temperature coordination solvent. In summary, anionic TOP-Se precursor are rapidly injected into solution containing the cationic TOPO-Cd precursor at elevated temperature under an inert atmosphere (nitrogen or argon).

Fig. 10 (a) Molecular structures of some thiol-ligands; (b) schematic illustration of the surface structure of the CdTe Qdots modified with MPA and poly(acrylic acid) (PAA). R represents carboxylic acid groups and the coil represents alkyl chain of PAA. Dotted lines show the coordination between carbonyl oxygen and cadmium on the Qdot surface. Unbounded sulphur atom on the surface indicates the decomposition of R group from the thiol-ligand.....

Fig. 11 Physicochemical properties of Qdots that determine their biological fate and inherent toxicity: shape, core and shell composition, size, and surface ligands can be manipulated during synthesis. Additional surface coating strategies, and surface modification steps with target-specific biomolecules can be assessed after their synthesis in order to increase the stability of Qdots against photo-oxidation and degradation to improve their biocompatibility, and manipulate their uptake efficiency.....

Fig. 12 Schematic overview of the different pathways by which NPs can induce oxidative stress: (a) NPs captured by lysosomes can generate ROS via direct reactivity of their surface coating, degradation of the surface coating or the whole NP in the acidic environment. Degradation of NP surface or itself can release its metal ions (Cd^{2+} , Pb^{2+} , In^{3+} , Fe^{2+}) to the intracellular environment which can in turn give rise to ROS levels by various chemical reactions. (b) NPs can also interact with mitochondria, destabilize its outer membrane, and can cause irregularities in electron transport chain of the oxidative phosphorylation. (c) NPs can directly interact with redox active proteins such as NADPH oxidase, therefore, can induce excess ROS formation in the immune cells. (d) NPs can also cause receptor activation and following to that triggering intracellular signalling cascades by binding to cell surface receptors. This can result in upregulation of ROS by expression of stress-responsive genes.....

Fig. 13 Schematic overview of NP-related characteristics that minimize NP-induced cytotoxicity, e.g. size, shape, purity, colloidal stability, surface charge and surface chemistry.....

Fig. 14 Overview of different surface coating (right side) and bioconjugation strategies for core/shell Qdots. Surface coating molecules are as follows: amphiphilic polymer coating with (i) carboxyl(ate) groups; (ii) PEG ligands; coordination of shell Zn^{2+} ions with dithiol-ligands containing (iii) PEG molecule; (iv) zwitterionic functionality; (v) carboxyl(ate) groups. R groups include carboxyl, amine, thiol, or methoxy moieties. Conjugation methods for biomolecules of interest (BOI) to the surface of Qdot are as follows: biotin-streptavidin binding; (vii) polyhistidine self-assembly; (viii) amide coupling using EDC/s-NHS activation; (ix) heterobifunctional cross-linking using succinimidyl-4-(N-maleimidomethyl)cyclohexane-1-carboxylate (SMCC); (x) aniline-catalyzed hydrazone ligation; and (xi) strain-promoted azide-alkyne cycloaddition.....

Fig. 15 Application of NIR Qdots in *in vivo* imaging and photothermal therapy: (i) Photothermal therapy efficiency of Qdots-rGO nanocomposites: (a) Schematic illustration of Qdot-rGO labelled MCF-7 cells exposed to irradiation (left) and after irradiation of Qdot-rGO causing cell death; (b) before irradiation cells were labelled with folic acid-targeted Qdot-rGO (red) and propidium (green) for live cell imaging; (c) after irradiation at 808 nm for 4 min, the area on the left side of marked line shows the fluorescence signal was diminished and the cells lost their viability. (ii) *In vivo* NIR fluorescence imaging of nude mice with water-soluble Ag_2S Qdots (emission at 910 nm): (A) control experiment, (B) with subcutaneous injection of Ag_2S Qdots, and (C) with celiac injection of Ag_2S Qdots (C, inset) shows the fluorescence signal of Qdots. (D) Corresponding emission spectra of autofluorescence of mice (blue) and Qdots labelled mice (red).....

Experimental Investigations

4.1 Aqueous synthesis of Qdots and their application in targeted imaging

- Fig. 1** Optical characteristics of NCs. Absorbance (a) and fluorescence emission spectra of CdTe/CdS CS NCs during particle growth for 6 h (b). Absorbance (c) and fluorescence emission profiles of CdTe/CdS/ZnS CSS NCs during ZnS shell growth for 6 h ($\lambda_{\text{excitation}} = 470$ nm) (d). Fluorescence efficiencies of CS and CSS NCs in terms of quantum yields (QY%) (e). Right insert shows the QY% of CSS NCs deposited on CS NCs ($\lambda_{\text{emission}} = 672$ nm). Left insert shows the QY% of CSS NCs deposited on CS NCs ($\lambda_{\text{emission}} = 652$ nm). Photostability of CS NCs and corresponding CSS NCs during continuous irradiation under UV light at 360 nm for 5 h (f).....38
- Fig. 2** Diffraction patterns of CS-I (CdTe/CdS, $\lambda_{\text{emission}} = 550$ nm), CS-II (CdTe/CdS, $\lambda_{\text{emission}} = 655$ nm) and its corresponding CSS-I (CdTe/CdS/ZnS, $\lambda_{\text{emission}} = 668$ nm) and CSS-II (CdTe/CdS/ZnS, $\lambda_{\text{emission}} = 687$ nm). The standard diffraction pattern of the reference cubic structures of CdTe (lattice constant $a = 6.4827$ Å), CdS ($a = 5.8304$ Å) and ZnS ($a = 5.4109$ Å) is also shown.....41
- Fig. 3** TEM images of CdTe/CdS NCs with low (a) and high magnifications (b), HRTEM images of CdTe/CdS NCs with a low (c) and a high magnification (d), HRTEM images of CdTe/CdS/ZnS NCs with a low (e) and a high magnification (f), a corresponding fast-Fourier transformation (FFT) profile of CdTe/CdS/ZnS NCs (g) and plotted profile of lattice plane distances along the CdTe/CdS/ZnS lattice lines (h).....42
- Fig. 4** Viability of A549 adenocarcinoma lung cancer cells treated with CS 550 (CdTe/CdS, $\lambda_{\text{emission}} = 550$ nm), CS 659 (CdTe/CdS, $\lambda_{\text{emission}} = 659$ nm) and its corresponding CSS 0.5 ML (CdTe/CdS/ZnS, 0.5 ML ZnS) and CSS 1 ML (CdTe/CdS/ZnS, 1 ML ZnS) with a concentration range 0.002–600 $\mu\text{g ml}^{-1}$. CellTiter-Blue assay was performed with the cells incubated with NCs for 2 h (a) and 24 h (b). Half maximal inhibitory concentration (IC_{50}) values were calculated by fitted dose–response curves (presented data as mean \pm standard deviation of 4 replicates).....44
- Fig. 5** Fluorescence microscope images of A549 adenocarcinoma lung cancer cells treated with S15 aptamer–NCs conjugates (a), Oligo–NCs (c), and bare NCs (d) for 2 h. Images of cells treated with S15–NCs after 24 h of internalization (b). Cell nuclei were counterstained with DAPI. Scale bar 50 μm46
- Fig. S1** HRTEM images of CdTe/CdS/ZnS NCs with high magnifications showing different tetrahedral shapes.....54
- Fig. S2** Atomic force microscopy (AFM) images of CdTe/CdS/ZnS nanocrystals deposited on poly lysine coated glass slides (a), the height profile of the cross-section marked with black straight line (b), 3-D surface plot of AFM image in (c).....54
- Fig. S3** Fluorescence lifetime decay profile of CdTe/CdS/ZnS NCs ($\lambda_{\text{emission}}=683$ nm). Sample was excited at 467 nm with a repetition rate of 1MHz. Sample was scanned for 30 seconds to constitute a single decay. This operation was repeated 5 times. An average decay was computed from all repeats for subsequent fitting (red line).....55
- Fig. S4** Fluorescence emission spectra of CdTe/CdS/ZnS NCs before and after irradiation under UV light at 360 nm for 5 h and 10 h. Fluorescence intensity was recorded every 10 s.....56
- Fig. S5** Digital image of agarose gel electrophoresis for CdTe/CdS/ZnS NCs, S15 aptamer conjugated NCs (S15/NCs) and oligonucleotide conjugated NCs (oligo/NCs) (exposure time: 0.4 s).....56

4.2 Application of Qdots to 3D spheroid cultures

Fig. 1 Bright-field microscope images of hAD-MSCs spheroids treated with different Qdot concentrations for 24 h. The Qdot solutions were introduced to the spheroids after cells were incubated for 24 h for spheroid formation ($t_{\text{QDOT}} = 24$ h). Scale bar is 200 μm67

Fig. 2 Effect of Qdot nanoparticles to the formation of hAD-MSCs spheroids. hAD-MSCs were exposed to different Qdot concentrations at the beginning of spheroid formation ($t_{\text{QDOT}} = 0$ h). Bright-field microscope images were taken after 24 h of Qdot treatment. Scale bar is 200 μm68

Fig. 3 Time-lapse bright-field microscope images of hAD-MSCs exposed to 600 $\mu\text{g ml}^{-1}$ Qdots solution at the beginning of spheroid formation ($t_{\text{QDOT}} = 0$ h). The effect of Qdots to the spheroid formation was monitored for 24 h.....69

Fig. 4 Cell viability data obtained from ATP assay. Data points are means \pm standard error of 3 ± 1 independent experiments which each were conducted in 4 replicates. * indicates significant difference at 0.01 level. $p < \alpha = 0.01$ (ANOVA one-way). Inset table shows half-maximal inhibitory concentrations (IC_{50}) in $\mu\text{g ml}^{-1}$. 2D cell culture having a biphasic dose–response curve possesses two IC_{50} values (IC_{50-1} and IC_{50-2}) whereas each 3D spheroid cultures have one IC_{50} value owing to monotonic dose–response pattern. Acceptance criteria is CV (coefficient of variance) $< 20\%$71

Fig. 5 Fluorescence imaging of hAD-MSCs spheroids treated with CdTe/CdS/ZnS Qdots for 4 h. (A) Fluorescence images captured from fluorescence microscopy from left-to-right: bright-field, Qdot (red), Calcein-AM (green) and DAPI (blue). (B) Single plane confocal images collected with 10 \times objective, from left-to-right: bright-field, DAPI (blue), Qdot (red), merge image of Qdot + DAPI and magnified spheroid. (C) Z-stacked confocal images of spheroid at individual z-planes. Z-stacks were acquired with 3 μm step size. The inserted graphic shows z-stack plot profile for normalized Qdot fluorescence mean intensity versus z-stack height (μm). (D) Single-plane confocal fluorescence images of spheroid at the bottom surface, from left-to-right: Qdot (red), Calcein-AM (green), DAPI (blue), merged image of Qdot + Calcein-AM + DAPI, and merge image of bright-field + Qdot + Calcein-AM + DAPI.....74

Fig. S1 Time-lapse microscope images of hAD-MSCs spheroids treated with 1200 $\mu\text{g/ml}$ Qdot solution. Qdots were introduced to the spheroid after cells were incubated for 24 for spheroid formation ($t_{\text{QDOT}} = 24$ h). Effect of Qdots to spheroid morphology was monitored for 24 h.....78

Fig. S2 Increase in hAD-MSCs spheroid diameters during Qdot exposure (1200 $\mu\text{g ml}^{-1}$) until 24 h. Spheroid diameters were normalized to the diameter of spheroid at the time= 0 h. Inset graph shows the linear relationship between the Qdot exposure time and the increase in spheroid diameter until 8 h (Adj. $R^2 = 0.977$).....79

Fig. S3 Cell viability data obtained from CTB assay. The fluorescence signals were normalized to untreated control samples. Data points are means \pm standard error of 3 ± 1 independent experiments which were conducted with 4 replicates. * indicates significant difference at 0.01 level. $p < \alpha = 0.01$ (ANOVA one-way).....79

4.3 Surface modification of Qdots with mPEG ligands

Fig. 1 (a) Schematic illustration of PEGylated CdTe/CdS/ZnS Qdots synthesis in aqueous medium; (b) red-shift in emission profiles of Qdots during ZnS shell growth in presence of mPEGthiols; (c) full-width at half maximum (FWHM) values for resulting Qdots as an indicator for size variations. 3-mercaptopropionic acid (MPA), which was used as sulphur source and at the same time as surface passivating ligand, coordinated at outer surface along with thiol-terminated mPEG molecules during ZnS shell growth.....86

Fig. 2 Characterization of COOH- and mPEG-Qdots; (a) Zeta-potential analysis; (b) ATR-FTIR spectra of (i) COOH-Qdot and (ii) mPEG-Qdot (1:10) films casted on a ZnSe-ATR crystal in water; (c) TG analysis of COOH-Qdots and mPEG-Qdots. The heating rate was 5 K min^{-1} under an 80% Argon and 20% O_2 flow. The vertical line indicates the temperature at which most of the adsorbed water was considered to be evaporated ($175 \text{ }^\circ\text{C}$).....88

Fig. 3 Structural stability of COOH-Qdots and mPEG-Qdots in water, DMEM cell culture medium with/without 10% fetal calf serum (FCS) at $4 \text{ }^\circ\text{C}$ and $37 \text{ }^\circ\text{C}$. Graphics show red-shift in Qdots emission wavelengths versus incubation time in given aqueous media. The aggregation induced red-shift in Qdot emission shows different profiles regarding the mPEG content.....91

Fig. 4 Determination of the dissociation constants of Qdots-BSA interactions by MST analysis. K_d values were calculated by fitting experimental data with Hill equation. Samples were excited at 470 nm with an excitation power of 10%, and thermophoresis analyses were conducted at room temperature with a 40% MST power. The error bars represent the standard deviation of at least two independent MST measurements.....93

Fig. 5 (a) Dose-dependent *in vitro* cytotoxicity of COOH-Qdots and mPEG-Qdots on A549 cell lines; (b) cell viability data obtained from CTB assay for 2D cell cultures; (c) bright-field microscope images of A549 tumor-like spheroids exposed to COOH- and mPEG-Qdots (1:5) with a concentration range of $0.002\text{--}1000 \text{ } \mu\text{g ml}^{-1}$ for 24 h. Data points are given as mean \pm standard error of 3 ± 1 independent experiments which each were conducted with 4 replicates. Inset data in (a) shows half-maximal inhibitory concentrations (IC_{50}) in $\mu\text{g/ml}$. * indicates significant difference at 0.01 level. $p < \alpha = 0.01$ (ANOVA one-way). Scale bars in (c) are $200 \text{ } \mu\text{m}$95

Fig. 6 Logarithmic flow cytometry histograms for the A549 cells stained with $100 \text{ } \mu\text{g ml}^{-1}$ COOH-Qdots and mPEG-Qdots for 30 min. Samples were excited at 488 nm, and minimum 30,000 gated-events were acquired for later analyses. The binding effect was defined as the ratio between the normalized fluorescence intensity of cells incubated with COOH-Qdots and mPEG-Qdots.....97

Fig. 7 Cellular interactions of COOH- and mPEG-Qdots with A549 tumor-like spheroids. Left-column shows confocal microscope images of tumor spheroids treated with COOH- and mPEG-Qdot (1:5) for 1 h. Fluorescence images for mPEG-Qdots (1:5) were captured with 10x (a) and 40x (b), for COOH-Qdots with 40x objectives (c) by applying 488 nm excitation laser (Argon/2). Images for mPEG-Qdot (1:10) are not given since they showed very similar cellular binding. Right-column shows surface plot profiles of spheroids treated with COOH- and mPEG-Qdots for 1 h and 24 h. (x, y) = (900, 900) μm . Mean fluorescence intensity values given in insets were measured after applying equal background subtraction to all images (ImageJ). Scale bar is $200 \text{ } \mu\text{m}$ for (a), and $50 \text{ } \mu\text{m}$ for (b, c).....98

Fig. S1 Confocal microscope images of A549 tumor-like spheroids treated with COOH- and mPEG-Qdots for 24 h. Column (a) shows low magnified fluorescence images of tumor spheroids, (b) shows high-magnification bright-field images of spheroid surfaces, and (c) their respective fluorescence profiles showing Qdots binding and uptake. White arrows in the bottom-right images highlight partial internalization of mPEG-Qdots (1:10) by outer cells.....110

List of Tables

Theoretical Background

Table 1. Recent advances in the application of bioconjugated-Qdots in imaging, sensing, and theranostics.	27
---	----

Experimental Investigations

4.1. Aqueous synthesis of Qdots and their application in targeted imaging

Table 1. Comparison of optical properties of core/shell/shell Qdots synthesized with aqueous approaches.	40
--	----

Table S1. Fluorescence lifetime characteristics of CdTe/CdS/ZnS NCs ($\lambda_{\text{emission}}=683$ nm).	55
--	----

References

1. A. P. Alivisatos, *Science*, 1996, **271**, 933-937.
2. A. P. Alivisatos, *J Phys Chem-Us*, 1996, **100**, 13226-13239.
3. R. Koole, E. Groeneveld, D. Vanmaekelbergh, A. Meijerink and C. de Mello Donegá, in *Nanoparticles: Workhorses of Nanoscience*, ed. C. de Mello Donegá, Springer-Verlag 2014, pp. 13-51.
4. C. D. Donega, *Chem Soc Rev*, 2011, **40**, 1512-1546.
5. J. A. Hollingsworth and V. I. Klimov, in *Nanocrystal quantum dots*, ed. V. I. Klimov, CRC Press, Boca Raton, 2nd edn., 2010, pp. 1-57.
6. E. Groeneveld, PhD, Utrecht University, 2012.
7. P. Zrazhevskiy and X. H. Gao, *Nano Today*, 2009, **4**, 414-428.
8. E. Cassette, M. Helle, L. Bezdetnaya, F. Marchal, B. Dubertret and T. Pons, *Adv Drug Deliv Rev*, 2013, **65**, 719-731.
9. T. P. A. Ruberu and J. Vela, *ACS Nano*, 2011, **5**, 5775-5784.
10. X. T. Lu, C. M. Hessel, Y. X. Yu, T. D. Bogart and B. A. Korgel, *Nano Lett*, 2013, **13**, 3101-3105.
11. A. R. Tao, S. Habas and P. D. Yang, *Small*, 2008, **4**, 310-325.
12. S. Lee, D. T. Lee, J. H. Ko, W. J. Kim, J. Joo, S. Jeong, J. A. McGuire, Y. H. Kim and D. C. Lee, *RSC Adv*, 2014, **4**, 9842-9850.
13. C. R. Bealing, W. J. Baumgardner, J. J. Choi, T. Hanrath and R. G. Hennig, *ACS Nano*, 2012, **6**, 2118-2127.
14. H. Zhang, D. Y. Wang, B. Yang and H. Mohwald, *J Am Chem Soc*, 2006, **128**, 10171-10180.
15. H. F. Bao, E. K. Wang and S. J. Dong, *Small*, 2006, **2**, 476-480.
16. D. S. Ling, M. J. Hackett and T. Hyeon, *Nano Today*, 2014, **9**, 457-477.
17. X. G. Peng, M. C. Schlamp, A. V. Kadavanich and A. P. Alivisatos, *J Am Chem Soc*, 1997, **119**, 7019-7029.
18. J. Lim, W. K. Bae, J. Kwak, S. Lee, C. Lee and K. Char, *Opt Mater Express*, 2012, **2**, 594-628.
19. P. Reiss, M. Protiere and L. Li, *Small*, 2009, **5**, 154-168.
20. P. Reiss, S. Carayon, J. Bleuse and A. Pron, *Synthetic Met*, 2003, **139**, 649-652.
21. L. L. Li, Y. Chen, Q. Lu, J. Ji, Y. Y. Shen, M. Xu, R. Fei, G. H. Yang, K. Zhang, J. R. Zhang and J. J. Zhu, *Sci Rep-Uk*, 2013, **3**, 1529.
22. D. V. Talapin, I. Mekis, S. Gotzinger, A. Kornowski, O. Benson and H. Weller, *J Phys Chem B*, 2004, **108**, 18826-18831.
23. T. Pons, E. Pic, N. Lequeux, E. Cassette, L. Bezdetnaya, F. Guillemin, F. Marchal and B. Dubertret, *ACS Nano*, 2010, **4**, 2531-2538.
24. S. Tamang, G. Beaune, I. Texier and P. Reiss, *ACS Nano*, 2011, **5**, 9392-9402.
25. V. V. Breus, C. D. Heyes and G. U. Nienhaus, *J Phys Chem C*, 2007, **111**, 18589-18594.
26. D. Liu and P. T. Snee, *ACS Nano*, 2011, **5**, 546-550.
27. Y. Y. Zhang, J. Y. Kim, Y. Kim and D. J. Jang, *J Nanopart Res*, 2012, **14**, 1117.
28. J. M. Tsay, M. Pflughoeft, L. A. Bentolila and S. Weiss, *J Am Chem Soc*, 2004, **126**, 1926-1927.
29. T. Pons, N. Lequeux, B. Mahler, S. Sasnouski, A. Fragola and B. Dubertret, *Chem Mater*, 2009, **21**, 1418-1424.
30. Y. He, H. T. Lu, L. M. Sai, Y. Y. Su, M. Hu, C. H. Fan, W. Huang and L. H. Wang, *Adv Mater*, 2008, **20**, 3416.
31. S. Taniguchi, M. Green, S. B. Rizvi and A. Seifalian, *J Mater Chem*, 2011, **21**, 2877-2882.
32. M. Green, P. Williamson, M. Samalova, J. J. Davis, S. Brovelli, P. Dobson and F. Cacialli, *J Mater Chem*, 2009, **19**, 8341-8346.
33. E. Petryayeva, W. R. Algar and I. L. Medintz, *Appl Spectrosc*, 2013, **67**, 215-252.

34. A. M. Smith, A. M. Mohs and S. Nie, *Nat Nanotechnol*, 2009, **4**, 56-63.
35. C. Y. Chen, C. T. Cheng, C. W. Lai, Y. H. Hu, P. T. Chou, Y. H. Chou and H. T. Chiu, *Small*, 2005, **1**, 1215-1220.
36. C. T. Cheng, C. Y. Chen, C. W. Lai, W. H. Liu, S. C. Pu, P. T. Chou, Y. H. Chou and H. T. Chiu, *J Mater Chem*, 2005, **15**, 3409-3414.
37. N. T. K. Thanh, N. Maclean and S. Mahiddine, *Chem Rev*, 2014, **114**, 7610-7630.
38. J. van Embden, A. S. R. Chesman and J. J. Jasieniak, *Chem Mater*, 2015, **27**, 2246-2285.
39. M. Ulusoy, J. G. Walter, A. Lavrentieva, I. Kretschmer, L. Sandiford, A. Le Marois, R. Bongartz, P. Aliuos, K. Suhling, F. Stahl, M. Green and T. Scheper, *RSC Adv*, 2015, **5**, 7485-7494.
40. Y. He, H. T. Lu, L. M. Sai, W. Y. Lai, Q. L. Fan, L. H. Wang and W. Huang, *J Phys Chem B*, 2006, **110**, 13352-13356.
41. R. E. Bailey, A. M. Smith and S. M. Nie, *Physica E*, 2004, **25**, 1-12.
42. G. Palui, F. Aldeek, W. T. Wang and H. Mattoussi, *Chem Soc Rev*, 2015, **44**, 193-227.
43. L. Liu, X. H. Guo, Y. Li and X. H. Zhong, *Inorg Chem*, 2010, **49**, 3768-3775.
44. K. Susumu, B. C. Mei and H. Mattoussi, *Nat Protoc*, 2009, **4**, 424-436.
45. H. Mattoussi, G. Palui and H. B. Na, *Adv Drug Deliver Rev*, 2012, **64**, 138-166.
46. M. Akin, R. Bongartz, J. G. Walter, D. O. Demirkol, F. Stahl, S. Timur and T. Scheper, *J Mater Chem*, 2012, **22**, 11529-11536.
47. C. M. Tyrakowski and P. T. Snee, *Phys Chem Chem Phys*, 2014, **16**, 837-855.
48. F. Zhang, E. Lees, F. Amin, P. Rivera Gil, F. Yang, P. Mulvaney and W. J. Parak, *Small*, 2011, **7**, 3113-3127.
49. W. R. Algar and U. J. Krull, *Chemphyschem*, 2007, **8**, 561-568.
50. W. Jiang, A. Singhal, J. N. Zheng, C. Wang and W. C. W. Chan, *Chem Mater*, 2006, **18**, 4845-4854.
51. Y. G. Zheng, S. J. Gao and J. Y. Ying, *Adv Mater*, 2007, **19**, 376.
52. V. Lesnyak, N. Gaponik and A. Eychmuller, *Chem Soc Rev*, 2013, **42**, 2905-2929.
53. J. Guo, W. Yang and C. Wang, *J Phys Chem B*, 2005, **109**, 17467-17473.
54. X. M. Xu, Y. L. Wang, W. X. Xia, L. Y. Zhou, F. Z. Gong and L. L. Wu, *Mater Chem Phys*, 2013, **139**, 210-214.
55. A. L. Rogach, T. Franzl, T. A. Klar, J. Feldmann, N. Gaponik, V. Lesnyak, A. Shavel, A. Eychmuller, Y. P. Rakovich and J. F. Donegan, *J Phys Chem C*, 2007, **111**, 14628-14637.
56. Z. Li, C. Q. Dong, L. C. Tang, X. Zhu, H. J. Chen and J. C. Ren, *Luminescence*, 2011, **26**, 439-448.
57. F. Zhang, X. W. He, W. Y. Li and Y. K. Zhang, *J Mater Chem*, 2012, **22**, 22250-22257.
58. D. W. Deng, W. H. Zhang, X. Y. Chen, F. Liu, J. Zhang, Y. Q. Gu and J. M. Hong, *Eur J Inorg Chem*, 2009, 3440-3446.
59. B. Xue, D. W. Deng, J. Cao, F. Liu, X. Li, W. Akers, S. Achilefu and Y. Q. Gu, *Dalton transactions*, 2012, **41**, 4935-4947.
60. O. M. Primera-Pedrozo, Z. Arslan, B. Rasulev and J. Leszczynski, *Nanoscale*, 2012, **4**, 1312-1320.
61. H. Zhang, Z. Zhou, B. Yang and M. Y. Gao, *J Phys Chem B*, 2003, **107**, 8-13.
62. W. W. Yu, Y. A. Wang and X. G. Peng, *Chem Mater*, 2003, **15**, 4300-4308.
63. N. Gaponik, D. V. Talapin, A. L. Rogach, K. Hoppe, E. V. Shevchenko, A. Kornowski, A. Eychmuller and H. Weller, *J Phys Chem B*, 2002, **106**, 7177-7185.
64. L. Zou, Z. Y. Gu, N. Zhang, Y. L. Zhang, Z. Fang, W. H. Zhu and X. H. Zhong, *J Mater Chem*, 2008, **18**, 2807-2815.
65. A. L. Rogach, L. Katsikas, A. Kornowski, D. S. Su, A. Eychmuller and H. Weller, *Ber Bunsen Phys Chem*, 1996, **100**, 1772-1778.
66. P. Jiang, C. N. Zhu, Z. L. Zhang, Z. Q. Tian and D. W. Pang, *Biomaterials*, 2012, **33**, 5130-5135.
67. Z. H. Sheng, H. Y. Han, X. F. Hu and C. Chi, *Dalton transactions*, 2010, **39**, 7017-7020.

68. G. X. Liang, L. L. Li, H. Y. Liu, J. R. Zhang, C. Burda and J. J. Zhu, *Chem Commun*, 2010, **46**, 2974-2976.
69. Z. T. Deng, O. Schulz, S. Lin, B. Q. Ding, X. W. Liu, X. X. Wei, R. Ros, H. Yan and Y. Liu, *J Am Chem Soc*, 2010, **132**, 5592.
70. B. B. Manshian, S. Munck, P. Agostinis, U. Himmelreich and S. J. Soenen, *Sci Rep*, 2015, **5**, 13890.
71. F. Zhao, Y. Zhao, Y. Liu, X. L. Chang, C. Y. Chen and Y. L. Zhao, *Small*, 2011, **7**, 1322-1337.
72. B. Yameen, W. I. Choi, C. Vilos, A. Swami, J. J. Shi and O. C. Farokhzad, *J Control Release*, 2014, **190**, 485-499.
73. M. Ulusoy, A. Lavrentieva, J.-G. Walter, F. Sambale, M. Green, F. Stahl and T. Scheper, *Toxicology Research*, 2015, DOI: 10.1039/c5tx00236b
74. K. M. Tsoi, Q. Dai, B. A. Alman and W. C. W. Chan, *Accounts Chem Res*, 2013, **46**, 662-671.
75. P. Rivera Gil, G. Oberdorster, A. Elder, V. Puentes and W. J. Parak, *ACS Nano*, 2010, **4**, 5527-5531.
76. B. B. Manshian, S. J. Soenen, A. Brown, N. Hondow, J. Wills, G. J. Jenkins and S. H. Doak, *Mutagenesis*, 2015, 1-10.
77. S. J. Soenen, P. Rivera-Gil, J. M. Montenegro, W. J. Parak, S. C. De Smedt and K. Braeckmans, *Nano Today*, 2011, **6**, 446-465.
78. S. J. Soenen, J. Demeester, S. C. De Smedt and K. Braeckmans, *Biomaterials*, 2012, **33**, 4882-4888.
79. B. Diaz, C. Sanchez-Espinel, M. Arruebo, J. Faro, E. de Miguel, S. Magadan, C. Yague, R. Fernandez-Pacheco, M. R. Ibarra, J. Santamaria and A. Gonzalez-Fernandez, *Small*, 2008, **4**, 2025-2034.
80. A. Panday, M. K. Sahoo, D. Osorio and S. Batra, *Cell Mol Immunol*, 2015, **12**, 5-23.
81. T. R. I. Pisanic, S. Jin and V. I. Shubayev, in *Nanotoxicity: From In Vivo and In Vitro Models to Health Risks*, ed. S. C. Sahu and D. A. Casciano, Wiley 2009, ch. 20.
82. N. Chen, Y. He, Y. Y. Su, X. M. Li, Q. Huang, H. F. Wang, X. Z. Zhang, R. Z. Tai and C. H. Fan, *Biomaterials*, 2012, **33**, 1238-1244.
83. A. Anas, H. Akita, H. Harashima, T. Itoh, M. Ishikawa and V. Biju, *J Phys Chem B*, 2008, **112**, 10005-10011.
84. I. Corazzari, A. Gilardino, S. Dalmazzo, B. Fubini and D. Lovisolo, *Toxicol in Vitro*, 2013, **27**, 752-759.
85. V. See, P. Free, Y. Cesbron, P. Nativo, U. Shaheen, D. J. Rigden, D. G. Spiller, D. G. Fernig, M. R. H. White, I. A. Prior, M. Brust, B. Lounis and R. Levy, *ACS Nano*, 2009, **3**, 2461-2468.
86. S. J. Cho, D. Maysinger, M. Jain, B. Roder, S. Hackbarth and F. M. Winnik, *Langmuir*, 2007, **23**, 1974-1980.
87. S. T. Stern, B. S. Zolnik, C. B. McLeland, J. Clogston, J. W. Zheng and S. E. McNeil, *Toxicol Sci*, 2008, **106**, 140-152.
88. R. F. Domingos, D. F. Simon, C. Hauser and K. J. Wilkinson, *Environ Sci Technol*, 2011, **45**, 7664-7669.
89. C. E. Bradburne, J. B. Delehanty, K. B. Gemmill, B. C. Mei, H. Mattoussi, K. Susumu, J. B. Blanco-Canosa, P. E. Dawson and I. L. Medintz, *Bioconjugate Chem*, 2013, **24**, 1570-1583.
90. S. J. Soenen, W. J. Parak, J. Rejman and B. Manshian, *Chem Rev*, 2015, **115**, 2109-2135.
91. S. K. Mahto, C. Park, T. H. Yoon and S. W. Rhee, *Toxicol in Vitro*, 2010, **24**, 1070-1077.
92. Y. Y. Su, Y. He, H. T. Lu, L. M. Sai, Q. N. Li, W. X. Li, L. H. Wang, P. P. Shen, Q. Huang and C. H. Fan, *Biomaterials*, 2009, **30**, 19-25.
93. L. Ju, G. L. Zhang, C. Zhang, L. Sun, Y. Jiang, C. L. Yan, P. J. Duerksen-Hughes, X. Zhang, X. Q. Zhu, F. F. Chen and J. Yang, *Mutat Res-Gen Tox En*, 2013, **753**, 54-64.
94. A. Romoser, D. Ritter, R. Majitha, K. E. Meissner, M. McShane and C. M. Sayes, *Plos One*, 2011, **6**, e22079.
95. Y. P. Ho and K. W. Leong, *Nanoscale*, 2010, **2**, 60-68.
96. P. Zrazhevskiy, M. Sena and X. H. Gao, *Chem Soc Rev*, 2010, **39**, 4326-4354.
97. X. W. He and N. Ma, *Colloid Surface B*, 2014, **124**, 118-131.

98. J. Y. Shi, F. Tian, J. Lyu and M. Yang, *J Mater Chem B*, 2015, **3**, 6989-7005.
99. L. J. Wang, Y. Yang and C. Y. Zhang, *Analytical chemistry*, 2015, **87**, 4696-4703.
100. U. Resch-Genger, M. Grabolle, S. Cavaliere-Jaricot, R. Nitschke and T. Nann, *Nat Methods*, 2008, **5**, 763-775.
101. X. H. Gao, L. L. Yang, J. A. Petros, F. F. Marshal, J. W. Simons and S. M. Nie, *Curr Opin Biotech*, 2005, **16**, 63-72.
102. R. Bilan, F. Fleury, I. Nabiey and A. Sukhanova, *Bioconjugate Chem*, 2015, **26**, 609-624.
103. A. S. Karakoti, R. Shukla, R. Shanker and S. Singh, *Adv Colloid Interfac*, 2015, **215**, 28-45.
104. W. J. Parak, T. Pellegrino and C. Plank, *Nanotechnology*, 2005, **16**, R9-R25.
105. G. T. Hermanson, *Bioconjugate techniques*.
106. V. Biju, T. Itoh and M. Ishikawa, *Chem Soc Rev*, 2010, **39**, 3031-3056.
107. N. Singh, S. Charan, K. Sanjiv, S. H. Huang, Y. C. Hsiao, C. W. Kuo, F. C. Chien, T. C. Lee and P. L. Chen, *Bioconjugate Chem*, 2012, **23**, 421-430.
108. P. Yang and G. J. Zhou, *Mater Res Bull*, 2011, **46**, 2367-2372.
109. Y. C. Lo, M. A. Edidin and J. D. Powell, *J Immunol*, 2013, **191**, 5107-5114.
110. Y. Chen, M. Molnar, L. Li, P. Friberg, L. M. Gan, H. Brismar and Y. Fu, *Plos One*, 2013, **8**.
111. X. W. He, L. Gao and N. Ma, *Sci Rep-Uk*, 2013, **3**, 2825.
112. C. Li, Y. Ji, C. Wang, S. J. Liang, F. Pan, C. L. Zhang, F. Chen, H. L. Fu, K. Wang and D. X. Cui, *Nanoscale Res Lett*, 2014, **9**, 244.
113. J. Wang, X. X. Huang, R. Zhu, Y. J. Long and H. Z. Zheng, *Anal Methods-Uk*, 2015, **7**, 3801-3805.
114. E. Cai, P. H. Ge, S. H. Lee, O. Jeyifous, Y. Wang, Y. X. Liu, K. M. Wilson, S. J. Lim, M. A. Baird, J. E. Stone, K. Y. Lee, M. W. Davidson, H. J. Chung, K. Schulten, A. M. Smith, W. N. Green and P. R. Selvin, *Angew Chem Int Edit*, 2014, **53**, 12484-12488.
115. S. Su, J. W. Fan, B. Xue, L. H. Yuwen, X. F. Liu, D. Pan, C. H. Fan and L. H. Wang, *ACS Appl Mater Inter*, 2014, **6**, 1152-1157.
116. X. Y. Huang, J. J. Wang, H. Liu, T. Lan and J. C. Ren, *Talanta*, 2013, **106**, 79-84.
117. J. M. Li, Y. Y. Wang, M. X. Zhao, C. P. Tan, Y. Q. Li, X. Y. Le, L. N. Ji and Z. W. Mao, *Biomaterials*, 2012, **33**, 2780-2790.
118. E. Y. Chung, C. J. Ochs, Y. Wang, L. Lei, Q. Qin, A. M. Smith, A. Y. Strongin, R. Kamm, Y. X. Qi, S. Y. Lu and Y. X. Wang, *Nano Lett*, 2015, **15**, 5025-5032.
119. B. R. Liu, J. G. Winiarz, J. S. Moon, S. Y. Lo, Y. W. Huang, R. S. Aronstam and H. J. Lee, *Colloid Surface B*, 2013, **111**, 162-170.
120. C. H. Ke, J. A. Chen, Y. J. Guo, Z. W. Chen and J. Y. Cai, *Bba-Biomembranes*, 2015, **1848**, 859-868.
121. H. F. Dong, W. H. Dai, H. X. Ju, H. T. Lu, S. Y. Wang, L. P. Xu, S. F. Zhou, Y. Zhang and X. J. Zhang, *ACS Appl Mater Inter*, 2015, **7**, 11015-11023.
122. J. Pichaandi and F. C. J. M. van Veggel, *Coordin Chem Rev*, 2014, **263**, 138-150.
123. L. Chen and H. Y. Han, *Microchim Acta*, 2014, **181**, 1485-1495.
124. R. Hu, K. T. Yong, I. Roy, H. Ding, W. C. Law, H. Cai, X. Zhang, L. A. Vathy, E. J. Bergey and P. N. Prasad, *Nanotechnology*, 2010, **21**, 145105.
125. M. Chu, X. Pan, D. Zhang, Q. Wu, J. Peng and W. Hai, *Biomaterials*, 2012, **33**, 7071-7083.
126. R. Hu, W. C. Law, G. Lin, L. Ye, J. Liu, J. Liu, J. L. Reynolds and K. T. Yong, *Theranostics*, 2012, **2**, 723-733.
127. S. H. Hu, Y. W. Chen, W. T. Hung, I. W. Chen and S. Y. Chen, *Adv Mater*, 2012, **24**, 1748-1754.
128. J. H. Gao, K. Chen, R. G. Xie, J. Xie, Y. J. Yan, Z. Cheng, X. G. Peng and X. Y. Chen, *Bioconjugate Chem*, 2010, **21**, 604-609.
129. J. Yang, Y. P. Hu, J. W. Tan, L. Jia, Y. H. Zhua and J. S. Yu, *J Mater Chem B*, 2015, **3**, 6928-6938.
130. F. D. Duman, I. Hocaoglu, D. G. Ozturk, D. Gozuacik, A. Kiraz and H. Y. Acar, *Nanoscale*, 2015, **7**, 11352-11362.
131. M. Montalti, A. Cantelli and G. Battistelli, *Chem Soc Rev*, 2015, **44**, 4853-4921.

132. X. Y. Cheng, S. B. Lowe, P. J. Reece and J. J. Gooding, *Chem Soc Rev*, 2014, **43**, 2680-2700.
133. T. L. Zhou, R. T. Anderson, H. S. Li, J. Bell, Y. A. Yang, B. P. Gorman, S. Pylypenko, M. T. Lusk and A. Sellinger, *Nano Lett*, 2015, **15**, 3657-3663.
134. K. Dohnalova, T. Gregorkiewicz and K. Kusova, *J Phys-Condens Mat*, 2014, **26**, 173201
135. S. Ohta, K. Yamura, S. Inasawa and Y. Yamaguchi, *Chem Commun*, 2015, **51**, 6422-6425.
136. S. Ohta, P. Shen, S. Inasawa and Y. Yamaguchi, *J Mater Chem*, 2012, **22**, 10631-10638.
137. F. Erogbogbo, K. T. Yong, I. Roy, R. Hu, W. C. Law, W. W. Zhao, H. Ding, F. Wu, R. Kumar, M. T. Swihart and P. N. Prasad, *ACS Nano*, 2011, **5**, 413-423.
138. R. Friedman, *J Natl Cancer I*, 2011, **103**, 1428-U1412.
139. H. T. Li, Z. H. Kang, Y. Liu and S. T. Lee, *J Mater Chem*, 2012, **22**, 24230-24253.
140. X. Y. Xu, R. Ray, Y. L. Gu, H. J. Ploehn, L. Gearheart, K. Raker and W. A. Scrivens, *J Am Chem Soc*, 2004, **126**, 12736-12737.
141. S. Y. Lim, W. Shen and Z. Q. Gao, *Chem Soc Rev*, 2015, **44**, 362-381.
142. X. Wang, L. Cao, S. T. Yang, F. S. Lu, M. J. Mezziani, L. L. Tian, K. W. Sun, M. A. Bloodgood and Y. P. Sun, *Angew Chem Int Edit*, 2010, **49**, 5310-5314.
143. Y. P. Sun, B. Zhou, Y. Lin, W. Wang, K. A. S. Fernando, P. Pathak, M. J. Mezziani, B. A. Harruff, X. Wang, H. F. Wang, P. J. G. Luo, H. Yang, M. E. Kose, B. L. Chen, L. M. Veca and S. Y. Xie, *J Am Chem Soc*, 2006, **128**, 7756-7757.
144. P. C. Hsu and H. T. Chang, *Chem Commun*, 2012, **48**, 3984-3986.
145. L. M. Hu, Y. Sun, S. L. Li, X. L. Wang, K. L. Hu, L. R. Wang, X. J. Liang and Y. Wu, *Carbon*, 2014, **67**, 508-513.
146. L. Zhou, Y. H. Lin, Z. Z. Huang, J. S. Ren and X. G. Qu, *Chem Commun*, 2012, **48**, 1147-1149.
147. S. T. Yang, L. Cao, P. G. J. Luo, F. S. Lu, X. Wang, H. F. Wang, M. J. Mezziani, Y. F. Liu, G. Qi and Y. P. Sun, *J Am Chem Soc*, 2009, **131**, 11308.
148. Q. Li, T. Y. Ohulchanskyy, R. L. Liu, K. Koynov, D. Q. Wu, A. Best, R. Kumar, A. Bonoiu and P. N. Prasad, *J Phys Chem C*, 2010, **114**, 12062-12068.
149. P. C. Hsu, P. C. Chen, C. M. Ou, H. Y. Chang and H. T. Chang, *J Mater Chem B*, 2013, **1**, 1774-1781.
150. H. Q. Tao, K. Yang, Z. Ma, J. M. Wan, Y. J. Zhang, Z. H. Kang and Z. Liu, *Small*, 2012, **8**, 281-290.
151. P. Juzenas, A. Kleinauskas, P. G. Luo and Y. P. Sun, *Appl Phys Lett*, 2013, **103**.
152. A. Mewada, S. Pandey, M. Thakur, D. Jadhav and M. Sharon, *J Mater Chem B*, 2014, **2**, 698-705.
153. K. A. S. Fernando, S. Sahu, Y. M. Liu, W. K. Lewis, E. A. Guliyants, A. Jafariyan, P. Wang, C. E. Bunker and Y. P. Sun, *ACS Appl Mater Inter*, 2015, **7**, 8363-8376.
154. R. J. Li, W. P. Hu, Y. Q. Liu and D. B. Zhu, *Accounts Chem Res*, 2010, **43**, 529-540.
155. M. Sytnyk, E. D. Glowacki, S. Yakunin, G. Voss, W. Schofberger, D. Kriegner, J. Stangl, R. Trotta, C. Gollner, S. Tollabimazraehno, G. Romanazzi, Z. Bozkurt, M. Havlicek, N. S. Sariciftci and W. Heiss, *J Am Chem Soc*, 2014, **136**, 16522-16532.
156. Y. L. Lei, Q. Liao, H. B. Fu and J. N. Yao, *J Phys Chem C*, 2009, **113**, 10038-10043.
157. L. T. Kang, Z. C. Wang, Z. W. Cao, Y. Ma, H. B. Fu and J. N. Yao, *J Am Chem Soc*, 2007, **129**, 7305-7312.
158. M. V. Kovalenko, L. Manna, A. Cabot, Z. Hens, D. V. Talapin, C. R. Kagan, V. I. Klimov, A. L. Rogach, P. Reiss, D. J. Milliron, P. Guyot-Sionnest, G. Konstantatos, W. J. Parak, T. Hyeon, B. A. Korgel, C. B. Murray and W. Heiss, *ACS Nano*, 2015, **9**, 1012-1057.
159. C. Philippot, F. Dubois, M. Maurin, B. Boury, A. Prat and A. Ibanez, *J Mater Chem*, 2012, **22**, 11370-11378.

List of Publications

1. **Ulusoy M.**, Jonczyk R., Walter J. G., Springer S., Lavrentieva A., Stahl F., Green M. and Scheper T., Aqueous synthesis of PEGylated quantum dots with increased colloidal stability and reduced cytotoxicity, *Bioconjugate Chemistry*, 2015, DOI: 10.1021/acs.bioconjchem.5b0049.
2. **Ulusoy M.**, Lavrentieva A., Walter J. G., Sambale F., Green M., Stahl F. and Scheper T., Evaluation of CdTe/CdS/ZnS core/shell/shell quantum dot toxicity on three dimensional spheroid cultures, *Toxicology Research*, 2015, 5, 126-135.
3. **Ulusoy M.**, Walter J. G., Lavrentieva A., Kretschmer I., Sandiford L., Marois A. Le, Bongartz R., Aliuos P., Suhling K., Stahl F., Green M. and Scheper T., One-pot aqueous synthesis of highly strained CdTe/CdS/ZnS nanocrystals and their interactions with cells, *RSC Advances*, 2015, 5, 7485.

Oral presentations

1. Aqueous synthesis of red-emitting CdTe/CdS/ZnS quantum dots and their interactions with cells, **Ulusoy M.**, Walter J. G., Bongartz R., Stahl F., Green M. and Scheper T., International Colloid and Interface Science Symposium, 6-9 July 2014, London/UK

Poster presentations

1. Dendrimer modified quantum dots conjugates for cancer cell imaging, **Akin M.**, Bongartz R., Walter J. G., Demirkol D. O., Stahl F., Timur S. and Scheper T., EC COST Thematic Workshop for nano-scaled arrangements of proteins, aptamers, and other nucleic acid structures and their potential applications, Helmholtz Centre for Environmental Research, UFZ, 8-9 October 2013, Leipzig/Germany
2. Quantum Dot Nanoparticles for cell detection, **Akin M.**, Bongartz R., Stahl F., 'Science Bridging' Exhibition of the German-Turkish Year of Research, Education and Innovation, 23 January 2014, Berlin/Germany (exhibition)
3. Synthesis of CdTe/CdS/ZnS quantum dots and their cytotoxicity in 3D spheroid cultures, **Ulusoy M.**, Lavrentieva A., Walter J. G., Stahl F., Green M. and Scheper T., Conference of Scientific Cooperation between Lower Saxony and Israel, March 10-11th 2015, Hanover/Germany

Curriculum Vitae

Mehriban Ulusoy

formerly Mehriban Akin

Nationalities: EU Republic of Bulgaria, Republic of Turkey

Languages: German, English, Turkish

Education

- 2012 – 2016** PhD graduate
Leibniz University of Hanover, Institute of Technical Chemistry, Germany
Thesis title: Aqueous synthesis and characterization of CdTe/CdS/ZnS quantum dots; their cytotoxicity and cellular interactions
Supervisor: Prof. Dr. Thomas Scheper
- 2009 – 2012** M.Sc. in Biochemistry (Mark: 90.9/100)
Ege University, Department of Biochemistry, Izmir, Turkey
Thesis title: Preparation of quantum dot bioconjugates for targeted imaging
Supervisor: Prof. Dr. Suna Timur
- 2004 – 2009** B.Sc. in Biochemistry (Mark: 3.08/4.0)
Ege University, Department of Biochemistry, Izmir, Turkey
Thesis title: Development of electrochemical biosensors for alcohol detection
Supervisor: Prof. Dr. Suna Timur

Employment

- 2013 – 2015** Research fellow at the Institute of Technical Chemistry, Hanover
- Supervised bachelor thesis: Aqueous synthesis and characterization of CdTe/CdS/ZnS core/shell/shell quantum dots
 - Tutored quantum dot synthesis experiments for high school students
 - Assisted undergraduate and master students in practical courses
 - Reviewed and marked laboratory reports

Professional activities

- 2013 – Present** Student member, Royal Society of Chemistry
- 2013 – 2015** Student member, DECHEMA
- 2014 – Present** Ad hoc reviewer *Physical Chemistry Chemical Physics*
- 2014 – Present** Ad hoc reviewer *RSC Advances*

Awards

2012 – 2013	PhD scholarship (DAAD, Germany)
2012	German language scholarship (Goethe Institute, Gottingen)
2010 – 2012	Master scholarship (TUBITAK, Turkey)
2007 – 2008	Undergraduate scholarship (City of Izmir Scholar Foundation)
2007 – 2008	Volunteer bursary (Turkey Volunteers Foundation-TOG)

Self-development courses

- Scientific image processing and analysis, Dr. Jan Brocher, 2014, Hanover
- Project management for young scientist, Dr. Simon Golin, 2014, Hanover
- Job hunting and interview skills, Rob Thompson, 2014, Hanover
- Negotiation Skills, Rob Thompson, 2014, Hanover

Social activities

- Helping immigrant students for their educational and social development (IKEM, Hanover)
- Organization of thematic social projects, e.g. global warming, environmental pollution and human rights; come-together events with elderly people; national “We are reading!” activity (Turkey Volunteers Foundation-TOG)
- Attending multicultural events (International Office, Hanover)
- Organization of social activities in the research institute, e.g. summer festival, Christmas party, Secret Santa, Pub night (Hanover)